Copyright

by

Christopher James Brennan

2018

The Dissertation Committee for Christopher James Brennan Certifies that this is the approved version of the following dissertation:

Piezoelectricity and Flexoelectricity in 2D Transition Metal Dichalcogenides

Committee:

Edward T. Yu, Supervisor

Nanshu Lu, Co-Supervisor

Sanjay K. Banerjee

Deji Akinwande

Rui Huang

Piezoelectricity and Flexoelectricity in 2D Transition Metal Dichalcogenides

by

Christopher James Brennan

Dissertation

Presented to the Faculty of the Graduate School of

The University of Texas at Austin

in Partial Fulfillment

of the Requirements

for the Degree of

Doctor of Philosophy

The University of Texas at Austin

May 2018

Dedication

To my family.

Acknowledgements

I first want to thank both of my advisors for their exceptional leadership and kindness during my time in graduate school. I'm honored to be among the first few Ph. D. students which Professor Nanshu Lu has graduated as she is bound to have a very long and successful career. I'm also honored to have been a member of Professor Edward T. Yu's research group which has already graduated many students due to Ed's amazing research mentorship. I have had the unique opportunity of being a member of two groundbreaking research groups where I was able to learn how to think of research problems from multiple perspectives. It's often said that one's research advisor shapes their graduate experience, and I count myself as doubly lucky to have had Ed and Nanshu as my advisors.

I'm also thankful for all my fellow lab members in both of my groups. As a new graduate student, they were kind enough to teach me proper lab techniques and how to operate the fabrication and characterization tools needed to perform my research. Through the years they have also provided me with priceless discussions that have helped with my research. It has been an honor to get to know so many future leaders of our industry.

I also appreciate Professor Sanjay K. Banerjee, Professor Deji Akinwande, and Professor Rui Huang for being members of my committee. They offered insightful discussions during my qualification exam and gave suggestions to strength my research. I have also been lucky enough to have been a coauthor with all of them.

I'd also like to acknowledge my funding sources: NSF CMMI Award under Grant No. 1351875, NSF DMR Award under Grant No. 1311866, The Dr. Brooks Carlton Fowler Endowed Presidential Graduate Fellowship in Electrical and Computer Engineering, and

The Temple Foundation Graduate Microelectronic and Computer Development Fellowship in Engineering.

The friends I have made during my tenure at UT are friends I hope to have for the rest of my life. They have made the stressful situation of graduate school a truly enjoyable one. Special thanks go to my roommates Andrew and Xin for living through graduate school with me and teaching me to cook.

Lastly, and most importantly, thank you to my entire family for supporting me through graduate school. My entire family has taught me by example the importance of a strong work ethic, how to treat others with respect, and the importance of family. Thank you to my father for fostering my love of engineering, my mother for loving and supporting me even though I moved to Texas, and my brother for being a positive role model by obtaining and doctoral degree himself. Words can’t describe how grateful I am for the love my family has given me. I would not have been able to accomplish this degree without them.

Piezoelectricity and Flexoelectricity in 2D Transition Metal Dichalcogenides

Christopher James Brennan, Ph. D.

The University of Texas at Austin, 2018

Supervisor: Edward T. Yu

Co-Supervisor: Nanshu Lu

Two-dimensional materials are only on to a few atoms thick, making them the thinnest possible material known to man. Their combination of electrical, optical, and mechanical properties allows for unique electrical devices with a wide range of future applications, from being a post-silicon material option, creating high-speed communication systems, allowing the advancement of flexible electronics, and even creating transparent electronics. Among their amazing characteristics is the coupling of electrical and mechanical properties. Although not unique to 2D materials, electromechanical coupling could be used in 2D materials to create a class of sensors, actuators, and energy harvesters at a scale not previously possible. Specifically, 2D materials could be utilized in flexible, wearable electronics as an energy harvester to convert the motion of the body into electrical energy. In this dissertation, the electromechanical coupling properties known as piezoelectricity and flexoelectricity are studied in 2D materials both to advance the development of 2D materials in general, and to improve the understanding of the relatively novel effect of flexoelectricity.

This work focuses on a class of 2D materials known as transition metal dichalcogenides (TMDs), which are semiconducting and intrinsically piezoelectric. To

begin, the adhesion between the TMDs and soft substrates is studied. Soft substrates could be used in flexible and wearable electronic systems, so adhesion of TMDs to soft substrates is important. It was found that the adhesions between the TMD molybdenum disulfide and polydimethylsiloxane is roughly 18 mJ m^{-2}. Next, the out-of-plane electromechanical coupling of molybdenum disulfide and other TMDs was studied. Piezoelectric theory predicts that there should be zero out-of-plane response, but a signal is measured in all TMDs, suggesting the presence of flexoelectricity. The measured effective out-of-plane piezoelectric response is on the order of 1 pm V^{-1} and the estimated flexoelectric response is on the order of 0.05 nC m^{-1}. Additionally, it was found that the magnitude of the out-of-plane electromechanical response of different TMDs roughly follows a trend predicted by a simple model of flexoelectricity. The work presented in this dissertation provides the first experimental evidence of a flexoelectric effect present in 2D TMDs.

Table of Contents

List of Tables xii

List of Figures xiv

Chapter 1: Introduction 1

1.1. Motivation of Research 2

1.2. 2D Materials 4

1.2.1. Graphene – The Conductor 4

1.2.2. Hexagonal Boron Nitride – The Insulator 6

1.2.3. Transition Metal Dichalcogenides – The Semiconductors ..6

1.3. Electromechanical Coupling 8

1.3.1. Piezoelectricity 8

1.3.2. Flexoelectricity 9

1.3.3. Electromechanical Coupling in 2D Materials 11

1.4. Introduction to Atomic Force Microscopy 13

1.4.1. General Overview 13

1.4.2. Tapping Mode 14

1.4.3. Contact Mode 16

1.5. Overview of Dissertation 17

Chapter 2: Measuring Adhesion of 2D Materials on Soft Substrates 19

2.1. Introduction 20

2.2. Experimental Methods 22

2.2.1. PDMS Preparation 22

2.2.2. MoS_2 Exfoliation 23

2.2.3. Buckle Formation 25

2.3. Results and Discussion 28

2.3.1. Determination of MoS_2 Flake Thickness 28

2.3.2. Calculation of Adhesion 32

2.3.3. Uncertainty Estimation 35

2.4. Conclusions and Significance 36

Chapter 3: Piezoresponse Force Microscopy....38
3.1. Introduction....39
3.2 Operating Principle....40
3.3. Sample Requirements....44
3.4. AFM Probe Particulars....45
3.5. Ideal Calculation of $d33$....48
3.6. PFM Deficiencies and Limitations....50
3.6.1. Material Clamping....50
3.6.2. Understanding the Forces Involved....51
3.6.3. The Effective Nature of the Measured $d33$....54
3.7. Background Vector Subtraction....55
3.7.1. The Inherent Background Signal....55
3.7.2. Unwanted Frequency Dependence....56
3.7.3. Removing the Background Signal....58
3.8. Uncertainty Estimation....61
3.9. Maximizing PFM Contrast....63
3.10. Conclusions and Significance....66
Chapter 4: Out-of-Plane Electromechanical Response of Monolayer MoS_2....68
4.1. Introduction....69
4.2. Experimental Methods....71
4.2.1. MoS_2 CVD Growth Overview....71
4.2.2. Transfer of CVD-Grown MoS_2....72
4.2.3. MoS_2 on Gold Thickness Determination....77
4.2.4. MoS_2 on Al_2O_3 Thickness Determination....80
4.3. PFM Results....86
4.3.1. MoS_2 on Gold....86
4.3.2. MoS_2 on Al_2O_3....88
4.4. Discussion....93
4.4.1. Results Summary and Comparison....93
4.4.2. Flexoelectricity as the Signal Origin....94

4.4.3. Contamination Issues 98
4.5. Conclusions and Significance 100

Chapter 5: Comparison of Electromechanical Responses Between TMDs 101
5.1. Introduction 102
5.2. Experimental Methods 102
5.2.1. $MoSe_2$ Sample Fabrication and Characterization 102
5.2.2. WS_2 Sample Fabrication and Characterization 104
5.2.3. WSe_2 Sample Fabrication and Characterization 106
5.3. Results 107
5.3.1. $MoSe_2$ PFM 107
5.3.2. WS_2 PFM 108
5.3.3. WSe_2 PFM 109
5.4. Discussion 110
5.5. Conclusions and Significance 113

Chapter 6: Conclusions and Outlook 114
6.1. Summary and Conclusion of Research 115
6.2. Future work and Outlook 117

References 119

List of Tables

Table 1.1 Summary of the basic equations used to describe piezoelectricity and flexoelectricity. Each effect has a direct and converse behavior, while piezoelectricity also has commonly interchangeable coefficients *d* and *e*. 9

Table 2.1 Summary of the fit values from the buckle-delaminations and wrinkles and the resulting adhesions measurement for each MoS_2 flake........35

Table 4.1 The calculated d_{33}^{eff} values for MoS_2 on gold and on Al_2O_3. The three columns represent different comparisons between the three PFM vectors created from the data. The first subtracts the background signal measured on the substrate and the second subtracts the background signal measured on the voltage-off condition. The third compares the two background conditions 93

Table 4.2 XPS measurements of the materials found on the surface of three different samples. First is pristine gold-coated silicon, second is gold-coated silicon which was stamped with PDMS, third is the sample used in the PFM measurement which is gold-coated silicon with MoS_2 transferred onto the surface with a PDMS stamp. 99

Table 5.1 A summary of the TMD materials investigated with PFM in this work. Also included from literature are the lattice constant, a_0, dielectric susceptibility, χ, the 2D Young's modulus, Y_{2D}, previous DFT estimates of in-plane piezoelectricity, d_{11}, and the estimated flexoelectric coefficient, μ_{est}. Here d_{33}^{eff} is calculated using gold measurement as the background vector. The effective flexoelectric coefficient μ_{eff}^{*} is also estimated for each TMD from the PFM measurements.................111

List of Figures

Figure 1.1 A single layer of graphene is shown with its hexagonal lattice structure. Reproduced from literature. 5

Figure 1.2 The structure of TMDs is overviewed in (a) where a single monolayer consists of three atoms and monolayers stack on top of each other via van der Waals forces. The geometry of the 2H-phase is shown in (b) and the 1T-phase is shown in (c). The top images show a top-view and the bottom images show a side-view of the TMD structure. These figures are reproduced from literature. 7

Figure 1.3 An example of a generic AFM probe. The entire structure is referred to as the probe with pyramidal structure called the tip and the long supporting rectangular prism being called the cantilever. The radius of curvature refers to how wide the apex of the tip is when fit to a sphere. 14

Figure 1.4 An illustration of tapping mode AFM. An AFM probe oscillates above a sample surface whose amplitude is defined as the tapping amplitude. The distance above the surface is called the amplitude setpoint and can be defined by the user. 15

Figure 1.5 An illustration of contact mode AFM. An AFM probe is brought into contact with a sample surface and caused to deform a certain amount defined as the deflection setpoint..16

Figure 2.1 Optical images of exfoliated MoS_2 on a PDMS substrate imaged using reflection mode (a) and transmission mode (b). The array of dark dots is from laser damage incurred during Raman spectroscopy measurements. 25

Figure 2.2 Schematic of the spontaneous buckling process. (a) First, the pressure of exfoliation process locally expands the PDMS surface. (b) Next, the release of the pressure lets the PDMS surface relax, transferring compressive strain to the MoS_2 that causes buckling. 26

Figure 2.3 Schematic of the pre-stretch process. (a) MoS_2 is transferred on top of a stretched PDMS substrate and then the strain is released (b) to form buckle-delaminations and wrinkles...27

Figure 2.4 Schematic defining the parameters of (**a**) buckle-delaminations and (**b**) wrinkles. An optical image of MoS_2 on PDMS with buckle-delaminations and wrinkles is shown in (**c**). This sample was created using the spontaneous buckling method. 28

Figure 2.5 AFM images (a, b) of two different MoS_2 flakes on PDMS. Cross-sectional height profiles of the wrinkles along the blue lines in the AFM images are given to the right of each (c, d). The green dashed line in each height profile is the MATLAB fit to the AFM experimental data. 31

Figure 2.6 AFM images (a, b) of two different MoS_2 flakes on PDMS. Cross-sectional height profiles of the buckle-delaminations along the blue lines in the AFM images are given to the right of each (c, d). The green dashed line in each height profile is the MATLAB fit to the height profile. 33

Figure 3.1 A block diagram of the PFM measurement system. An alternating voltage is applied across a sample material which will deform if it is electro-mechanically active. The deflection will then be measured by the laser in the position sensitive photodiode and amplified by the lock-in amplifier. The amplitude and phase are the two output channels of the measurement. 41

Figure 3.2 The calibration process to determine the deflection sensitivity. A typical loading curve shown in (a) illustrates each stage of the process and is labeled with a corresponding graphical representation of each mechanism. As the Z-piezo tube extends the AFM probe towards the surface but does not yet contact the surface, the laser deflection does not change (b). Once the AFM tip is close enough to the sample to interact via van der Waals forces, it 'jumps' to the sample (c). Finally, the Z-piezo tube continues to expand, loading the AFM probe and sample surface causing the cantilever to bend and deflect the laser upward (d). The dashed black line in (a) is a linear fit to the (d) region and represents the deflection sensitivity. 44

Figure 3.3 The electric field distribution arising as a result of the applied voltage between the AFM tip and the bottom electrode and the resultant direction of the mechanical response of the sample. The black arrows represent the electric field distribution and the dashed red arrows represent the material response. 49

Figure 3.4 Material clamping in the PFM experiment. When only the AFM tip is used as the electrode, only a small area around the tip is affected and responds to the localized electric field (a). The rest of the material which doesn't experience the same electric field clamps the reacting material's ability to respond fully. Depositing an electrode on top of the sample will result in a more uniform and broad distribution of the electric field, reducing the clamping effect (b). Reproduced from Jungk et. al......51

Figure 3.5 AFM probe in-contact with a PFM sample. The blue areas represent electromechanically active materials on a gold substrate. The opaque grey rectangular box represents the area on the sample which is directly below the AFM cantilever. If there were electrostatic contributions to the force between the cantilever and the sample, the signal measured at the AFM tip point would be an average over the entire opaque box area. If the individual sample areas are distinguishable, then electrostatic forces from the cantilever are negligible. 53

Figure 3.6 The frequency response of the PFM amplitude while sweeping the drive frequency from 15 kHz – 65 kHz. There is a very complex response below 50 kHz, so this range of drive frequencies should be avoided. Instead 60 kHz is used as the drive frequency in this work because it is in a range that is relatively frequency independent. 58

Figure 3.7 A depiction of the vector background subtraction method. First, a PFM image is obtained on a sample capturing the amplitude and phase channel on both the sample and substrate. Next, vectors are created from the amplitude and phase data and are subsequently subtracted from each other. The result, shown in blue here, is a background-subtracted vector that can be used for d_{33}^{eff} calculations. The uncertainty of each measured vector is depicted as a circle at the end of each vector, of which the vector could point to anywhere within. 61

Figure 3.8 The length of the cantilever will affect the bending angle for a given vertical deflection. A shorter cantilever (a) will have a larger bending angle than a larger cantilever (b). This results in better sample displacement resolution for shorter cantilevers. 65

Figure 4.1 The schematic steps in the transfer process are shown with associated pictures of the sample at each step. The process is as follows: (a) MoS_2 is grown on SiO_2 via CVD; (b) a PDMS stamp is pressed on the MoS_2; (c) the sample is submerged in water; (d) the sample is removed from water, dried, and the PDMS is peeled off with some MoS_2; (e) the MoS_2 on PDMS is placed on the receiving substrate (gold shown here) and heated on a hot plate to 50 - 70 °C; (f) and finally the PDMS stamp is slowly peeled away, leaving the MoS_2 on the receiving gold substrate. 73

Figure 4.2 Microscope images of the MoS_2 on the growth substrate (a), PDMS stamp (c), and gold (e), with corresponding photoluminescence measurements shown to the right (b, d, f). The three monolayer PL signals on the different substrates are shown together in (g), where there is a peak shift after the MoS_2 is removed from the growth substrate.76

Figure 4.3 Raman spectra of monolayer MoS_2 on SiO_2, PDMS and gold substrates. The locations of these measurements are the same as in Figure 4.2. The shift in the highlighted E' peak indicates the presence of strain when the MoS_2 is on the SiO_2 substrate. 77

Figure 4.4 Characterization of CVD-grown MoS_2 transferred on gold. Optical microscope image in (a) shows MoS_2 is visible on gold. The colored circles represent the monolayer and multilayer measurement location for Raman (b) and PL (c). Tapping-mode AFM of roughly the same area as (a) is shown in (d). The white box indicates the location of the height profile shown in (e). 80

Figure 4.5 Optical microscope image of CVD-grown MoS_2 transferred onto a thin layer of Al_2O_3 on Si where the monolayer MoS_2 is not visible is shown in (a). A tapping-mode AFM image of the red boxed area is shown in (b) where the location of the MoS_2 becomes apparent. Raman spectroscopy measurements are shown in (c), where the non-optically-visible monolayer area does not give a detectable signal but the barely-visible thick MoS_2 does give a detectable signal. The areas of measurement are depicted and color-coded in the inset, where the 'thick' measurement is on the same location as labeled in (a) and (b). The inset scale bar is 10 μm and the large peak around 520 cm^{-1} is from the underlying Si substrate. 82
Figure 4.6 Tapping mode AFM measurement of monolayer and bilayer MoS_2 on Al_2O_3 is shown in (a). The area shown here corresponds to the area near the label of bilayer in Figure 4.5 (b). Height profiles along the white boxes are given in (b). Step 1 shows the height from monolayer to Al_2O_3 substrate to monolayer again. Step 2 shows a step from monolayer to bilayer MoS_2. The monolayer thickness is inflated when measured from the substrate. 83

Figure 4.7 CVD-grown MoS_2 on its SiO_2 growth substrate. (a) shows a tapping-mode AFM image, where the two boxes indicate the locations of the step heights plotted in (c). An optical microscope image is shown in (b), where the white box indicates the location of the color-coded Raman map in (d). In increasing intensity, black shows no MoS_2, blue shows monolayer MoS_2, green shows bilayer, and yellow and red show multilayer MoS_2. The white circles indicated in (b) show the location of Raman spectral measurements in (e). 85

Figure 4.8 An optical image of the MoS_2 on gold is shown in (a) where the red box indicates the area imaged by PFM in Figure 4.9. A schematic of the MoS_2 on gold sample is shown in (b). The AFM is purposely drawn broad because on the scale of monolayer MoS_2 and with tip wear, the AFM tip will be broad in comparison to the MoS_2 thickness...........86

Figure 4.9 The PFM measurements of the MoS_2 on gold sample. The drive voltage is applied in (a) – (c) and the drive voltage is not applied in (d) – (f). The topography images (a) and (d) show the background gold substrate, monolayer MoS_2, and multi-layer MoS_2 regions. The applied drive voltage does not affect the topographic measurement (color bar is 0 nm to 5 nm for both). The PFM amplitude images (b) and (e) show that the MoS_2 region has contrast against the gold substrate only when the drive voltage is applied (b). The same is true for the PFM phase images (c) and (f). Both amplitude images and phase images share the same color scale...87

Figure 4.10 A tapping-mode AFM image of the MoS_2 on Al_2O_3 is shown in (a) where the red box indicates the area imaged by PFM in Figure 4.11. A schematic of the MoS_2 on Al_2O_3 sample is shown in (b). The MoS_2 is transferred onto Al_2O_3 to limit current flow through MoS_2 to the bottom electrode. The AFM is purposely drawn broad because on the scale of monolayer MoS_2 and with tip wear, the AFM tip will be broad in comparison to the MoS_2. 89

Figure 4.11 The PFM measurements of the MoS_2 on Al_2O_3 sample. The drive voltage is applied in (a) – (c) and the drive voltage is not applied in (d) – (f). The topography images (a) and (d) show the background Al_2O_3 substrate, monolayer MoS_2, and bilayer MoS_2 regions. The applied drive voltage does not affect the topographic measurement (color bar is 0 nm to 3.7 nm for both). The PFM amplitude images (b) and (e) show that the MoS_2 region has contrast against the Al_2O_3 substrate only when the drive voltage is applied (b). The same is true for the PFM phase images (c) and (f). Both amplitude images and phase images share the same color scale. 90

Figure 4.12 The response of the PFM amplitude with a DC Bias sweep applied in addition to the AC drive voltage. There is no dependence on DC bias seen in this measurement, meaning that there are no electrostatic force contributions present in the PFM measurement...............................92

Figure 5.1 The $MoSe_2$ sample fabricated on gold is shown. An optical microscope image is shown in (a), and a tapping mode AFM image is shown in (b) where the color bar indicates heights of 0 nm to 30 nm. This tapping mode image was edited using the Gwyddion open source SPM data analysis software. The Raman spectrum of the monolayer region is shown in (c)..104

Figure 5.2 The WS_2 sample fabricated on gold. An optical microscope image is given in (a). The black and red dot indicate the location of the monolayer and multilayer measurements for the Raman (b) and photoluminescence (c) measurements. 105

Figure 5.3 The WSe_2 sample fabricated on gold. An optical microscope image is given in (a) and a tapping mode AFM is given in (b). The color bar represents height of 0 nm to 26.6 nm. A Raman measurement is shown in (c) of the monolayer and multilayer region of the WSe_2 sample on the black and red dot in (a). 106

Figure 5.4 PFM images of $MoSe_2$ with the drive voltage applied (a, c, e) and not applied (b, d, f). The height image is given in (a, b), the PFM amplitude image is given in (c, d) and the PFM phase is given in (e, f). The scale bars correspond to both images to their left. The imaging conditions were: V_d = 5 V, f_d = 60 kHz, scan speed = 5 µm/sec. 108

Figure 5.5 PFM images of WS_2 with the drive voltage applied (a, c, e) and not applied (b, d, f). The height image is given in (a, b), the PFM amplitude image is given in (c, d) and the PFM phase is given in (e, f). The scale bars correspond to both images to their left. The imaging conditions were: V_d = 7 V, f_d = 60 kHz, scan speed = 5 µm/sec. 109

Figure 5.6 PFM images of WSe_2 with the drive voltage applied (a, c, e) and not applied (b, d, f). The height image is given in (a, b), the PFM amplitude image is given in (c, d) and the PFM phase is given in (e, f). The scale bars correspond to both images to their left. The imaging conditions were V_d = 7 V, f_d = 60 kHz, scan speed = 5 μm/sec........................110

Figure 5.7 A plot comparing the estimated value of the flexoelectric coefficient, μ_{est}, using Kogan's method to the calculated value of the flexoelectric coefficient, μ_{eff}^{*} , from PFM measurements. WSe_2 is shown as a blue diamond to emphasis that it does not follow the trend of the other TMDs. 113

Chapter 1:

Introduction[i]

The research presented here originated from studying the link between mechanical deformation and electrical polarization called electromechanical coupling. This first chapter introduces the relevant principles and materials used in the research. First, the motivation for this research is presented with a brief description of two-dimensional materials and why they are useful for this study. Next, electromechanical coupling is introduced along with the platform used for the measurements performed. Finally, an overview of the following chapters is discussed.

[i] Akinwande, D.; Brennan, C. J.; Bunch, J. S.; Egberts, P.; Felts, J. R.; Gao, H.; Huang, R.; Kim, J.; Li, T.; Li, Y.; et al. A Review on Mechanics and Mechanical Properties of 2D materials—Graphene and beyond. Extrem. Mech. Lett. 2017, 13, 42–77.
Author Contributions of included section titled 'Piezo- and flexoelectricity': C.J.B. researched and wrote section, N.L. edited and reviewed included section, R.H. edited section, K.M.L. edited section.

1.1. Motivation of Research

The success of modern electronics and the possibilities for its future rest on a foundation of incremental gains in basic scientific knowledge. Each new discovery about how the world works leads to new capabilities that help propel the scientific community forward. Even minor advances can have far-reaching implications that may not be anticipated at the time. It is partially this spirit of scientific discovery, along with more concrete goals, that has motivated this study on piezoelectricity and flexoelectricity in two-dimensional transition metal dichalcogenides.

Flexible and wearable electronics have increasingly gained popularity over the past decade[1–4]. They offer a unique combination of the computing power of modern electronics and state-of-the-art sensing capabilities in a platform which can conform to and move with the human body. One type of wearable system called epidermal electronics[1], or electronic tattoos, can perform electrocardiograms (ECGs)[5], electromyograms (EMGs)[6], and electroencephalograms (EEGs)[7] by having very conformal electrodes in direct contact with the skin. These systems are designed with serpentine structures which greatly reduce stresses generated in the device materials during deformation[8]. Additionally, these devices are exceptionally thin, allowing for extreme flexibility and thus conformability to the micron-scaled features of the human epidermis[6].

One challenge of these systems is delivering power to the device for measurement and data acquisition. The platform is very thin and does not allow for the use of traditional batteries, which tend to be bulky and inflexible. The current solution is to attach connectors to the devices to supply power from an external source. This limits the applicability of the device as a mobile, wearable system by being physically tethered to an external power source. The first motivator of this research is to work towards a solution to this problem by developing the technology and physical understanding needed to incorporate energy

harvesters in epidermal electronic systems. Energy harvesters in this case would take advantage of the stresses and strains created by normal use and convert that mechanical energy into electrical energy. Simply moving the body while wearing the device would power the device's functions.

The physical phenomenon which makes this possible is called electromechanical coupling, specifically piezoelectricity[9] and flexoelectricity[10–12], which link portions of a material's mechanical properties with portions of its electrical properties. Before energy harvesting can be implemented in epidermal electronics, a stronger foundational knowledge of electromechanical coupling in materials compatible with this type of system is required. One such material class which meets the system requirements is two-dimensional (2D) materials due to their extreme flexibility, mechanical robustness[13–15], and intrinsic electromechanical coupling[16].

2D materials have experienced an explosion in popularity since 2004[17] due to their impressive electronic[18,19], optical[20–23], and mechanical properties[13–15]. This leads to the second major motivator of this research: advancing the understanding of 2D materials for future use in electronic systems. Beyond their use in flexible systems, 2D materials have promise as a post-silicon material for devices at nanometer scale[24]. They also hold potential as various types of sensors, including chemical[25], strain[26], and optical[27] modalities. 2D materials may be the future of electronic devices, so gaining understanding of their physical properties will benefit future device design. Specifically in this research, the piezoelectric and flexoelectric properties of a few 2D materials are studied to gain insight into the materials' base, physical properties. The information gained will be able to be applied to energy harvester, strain sensor, and actuator design.

The third major motivator of this research is gaining a deeper understanding of the electromechanical phenomena known as flexoelectricity. As previously mentioned,

piezoelectricity and flexoelectricity are principally being studied here for their applicability towards energy harvesters. Piezoelectricity is a well-developed field which links uniform strain fields with uniform polarization fields[9,28]. Flexoelectricity, on the other hand, is a relatively new and underdeveloped field and relates strain gradients to polarization[10–12]. Since the field of flexoelectricity is in its scientific infancy, any gain in understanding will help advance the field. This work will use 2D materials as a platform to study and analyze the flexoelectric effect.

Thus, the research presented here is motivated by three factors: 1) gaining basic understanding of the physical phenomena known as flexoelectricity, 2) adding to the knowledge base of the properties of 2D materials, and 3) the potential application of 2D materials and electromechanical coupling for energy harvesting in epidermal electronics. This work does not design or create energy harvesters, but instead builds upon and extends the science and physics needed for the design of such a device.

1.2. 2D MATERIALS

2D materials are in general single atomic layers whose surfaces interact with other surfaces via van der Waals forces. There are no dangling bonds on their surfaces which makes them ideal for electronic applications[29]. They were first discovered by exfoliating, or cleaving, single atomic layers from a bulk crystal material[17]. The bulk material is simply many layers of 2D materials stacked on top of each other via van der Waals forces. There are a few different classes of 2D materials; the most prominent ones will be discussed in the following.

1.2.1. Graphene – The Conductor

The most well-known 2D material, graphene is a single atomic layer of carbon atoms arranged in a hexagonal lattice. The carbon atoms are sp^2 hybridized with in-plane

σ-bonds and out-of-plane π-orbitals[30,31]. The in-plane σ-bonds make graphene one of the strongest known materials with a Young's modulus of 1TPa[13]. Multiple layers stacked on top of each other will eventually result in the bulk material known as graphite. An example of a single layer of graphene[30] is shown in Figure 1.1.

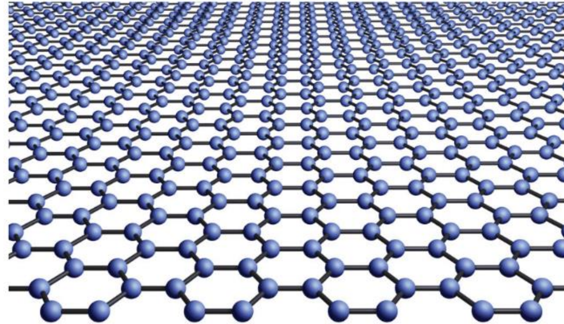

Figure 1.1 A single layer of graphene is shown with its hexagonal lattice structure. Reproduced from literature[30].

Graphene's remarkable nature becomes most apparent when there is only a single layer present, known as a monolayer. At the monolayer limit, its electronic properties are dominated by the valence and conduction bands meeting at a single point, creating a semimetal. The dispersion relation becomes linear and the charge carriers act as massless Dirac fermions[30]. Graphene possesses many other remarkable properties, but in the context of this research, graphene is not ideal because of its conducting ability. Electrical conductors are not electromechanically active because free carriers can screen out the electric field that may cause mechanical deformation. Graphene can be induced to have a bandgap[32] and even to be piezoelectric[33], but these methods require careful and precise fabrication which is not necessary in other 2D materials. Therefore, graphene was not chosen as a material to study in this research.

1.2.2. Hexagonal Boron Nitride – The Insulator

The next major type of 2D material is hexagonal boron nitride (h-BN). This material is similar to graphene in that it is a single atomic layer of atoms in a hexagonal array, but different in that there are two different atoms within the unit cell. This leads to a breaking of symmetry which both creates a bandgap, making the material an insulator[34], and induces intrinsic in-plane piezoelectricity[16]. Monolayer h-BN is thus an insulating counterpart to conductive graphene. It can also be used as encapsulation for graphene. It protects graphene's electronic structure from the surrounding environment and improve mobility values because of its atomically smooth surface which also has no dangling bonds[35].

Even with h-BN's insulating capabilities and intrinsic piezoelectricity, it is not ideal for the current research on 2D material electromechanical coupling. As will be described in Chapter 3, a technique called piezoresponse force microscopy (PFM) is employed to measure out-of-plane electromechanical coupling. Monolayer h-BN has no 'thickness' since it is only a single atomic layer of nitrogen and boron atoms, making the out-of-plane movement of atoms unlikely. Therefore, a 2D material which has some 'thickness' and possesses a bandgap would be an ideal candidate for this research.

1.2.3. Transition Metal Dichalcogenides – The Semiconductors

Transition metal dichalcogenides (TMDs) are the next major class of 2D materials and consist of three atoms in their unit cell[36]. A monolayer of a TMD is also not a single atomic plane of atoms, but instead three atoms thick. Shown in Figure 1.2 (a), the middle atom is the transition metal atom and the top and bottom atoms are the chalcogen atoms[19]. The most common configurations use the transition metals molybdenum (Mo) or tungsten (W) with the chalcogen atoms sulfur (S), selenium (Se), or tellurium (Te). Among the corresponding combinations, MoS_2, $MoSe_2$, $MoTe_2$, WS_2, and WSe_2 typically exist in the

2H-phase, are semiconducting, and are air-stable, while WTe_2 is more energetically favorable in the 1T-phase, which is metallic. The different phase geometries[36] are shown in Figure 1.2 (b) and (c). Semiconducting TMDs complete the suite of 2D electronic materials needed to create a functional transistor. Graphene can be used as the source, drain, and gate electrode, h-BN can be used as the gate dielectric, and a TMD can be used as the semiconducting channel.

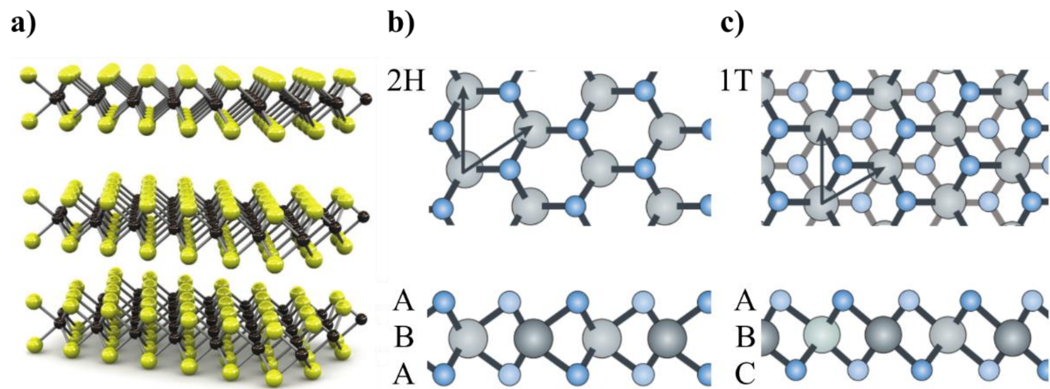

Figure 1.2 The structure of TMDs is overviewed in (a) where a single monolayer consists of three atoms and monolayers stack on top of each other via van der Waals forces[19]. The geometry of the 2H-phase is shown in (b) and the 1T-phase is shown in (c)[36]. The top images show a top-view and the bottom images show a side-view of the TMD structure. These figures are reproduced from literature[19,36].

Like h-BN, TMDs in the 2H-phase have a bandgap and are intrinsically piezoelectric. Unlike h-BN, TMDs have a 3-atom thick monolayer which allows for atomic displacement out-of-plane which could be measurable. These properties make TMDs a perfect candidate for studying electromechanical coupling of 2D materials. To summarize, they are extremely thin and thus extremely flexible for use in wearable electronics, they are semiconducting and electromechanically active, and they have a non-zero thickness, which makes studying out-of-plane electromechanical coupling effects possible.

1.3. ELECTROMECHANICAL COUPLING

1.3.1. Piezoelectricity

The most well-known type of electromechanical coupling is piezoelectricity. It relates strains and stresses to polarizations and electric fields. There is both a direct piezoelectric effect in which an applied stress creates a polarization within the crystal, and a converse piezoelectric effect in which an applied electric field creates a strain in the crystal. The relationships between these mechanical and electrical properties are summarized in Table 1.1. Among the equations used in the table, P, E, ε, σ, μ, and x represent the polarization, electric field, strain, stress, flexoelectric coefficient and spatial direction, respectively. The subscripts i, j, k, l all represent the different cartesian directions as *1*, *2*, and *3*, or x, y, and z.

Piezoelectricity is usually described by one of two coefficients, d or e. The coefficient d is used throughout this research because it offers a more intuitive explanation of the physical effect. It has two equivalent units, Coulombs per Newton or meters per volt. In direct piezoelectricity, d can be thought of as representing the amount of charge accumulated per applied force ($C\ N^{-1}$). In converse piezoelectricity, d can be thought of as representing the amount of displacement field created per applied voltage ($m\ V^{-1}$).

The origin of the piezoelectric effect is a fundamental asymmetry in a crystal's lattice structure. Because of this, not all crystal structures possess piezoelectric properties. Only crystals which fall under the class of non-centrosymmetric crystals exhibit piezoelectricity, while crystals structures of higher symmetry do not. Centrosymmetry exists if a crystal can be transferred from every point (x, y, z) to (-x, -y, -z) and retain the same geometric structure. Piezoelectric materials must be non-centrosymmetric so that a strain within the crystal will separate the centers-of-mass of the positively and negatively

charged ions. This limitation on the crystal's structure limits the materials which can be used to create the piezoelectric effect.

Electromechanical Effect	Strain / Stress	Direct Effect	Converse Effect
Piezoelectricity	Strain	$P_i = e_{ijk}\varepsilon_{jk}$	$\varepsilon_{jk} = d_{ijk}E_i$
	Stress	$P_i = d_{ijk}\sigma_{jk}$	$\sigma_{jk} = e_{ijk}E_i$
Flexoelectricity	Strain	$P_i = \mu_{ijkl}\frac{\partial \varepsilon_{jk}}{\partial x_l}$	-
	Stress	-	$\sigma_{ij} = \mu^*_{ijkl}\frac{\partial E_k}{\partial x_l}$

Table 1.1 Summary of the basic equations used to describe piezoelectricity and flexoelectricity. Each effect has a direct and converse behavior, while piezoelectricity also has commonly interchangeable coefficients *d* and *e*.

1.3.2. Flexoelectricity

Flexoelectricity is similar to piezoelectricity, except spatial gradients are involved, making the analysis and understanding slightly more challenging. Flexoelectricity also has direct and converse effects: in the direct effect an applied strain gradient will create a polarization, and in the converse effect an applied electric field gradient will create a stress. There have also been reports where an applied uniform electric field has induced a curvature in the material[37]. The equations used to describe the flexoelectric effects are also shown in Table 1.1 alongside the piezoelectric equations for comparison.

Unlike piezoelectricity, flexoelectricity is present in every crystal structure and does not rely on inherent asymmetry in the crystal structure. Due to the spatial gradient terms in the constitutive equations, different amounts of strain at different physical locations within the crystal create the asymmetry needed to separate the centers-of-mass of

positive and negative charge to give rise to a polarization. This means that a wider variety of materials are available for use as electromechanical devices. Additionally, since many of the best performing piezoelectric materials contain lead, flexoelectricity opens the door for the use of more biocompatible materials or enhancing the piezoelectric effect within devices used for sensors, actuators, and energy harvesters.

Flexoelectricity is also a relatively new discovery which remains not well understood. Over the past few decades, awareness of flexoelectricity has slowly increased within the scientific community, but many current researchers are still unaware of its existence. One reason for this is because flexoelectricity is a weaker effect than piezoelectricity in most situations. Only when the length scales of interest approach the nanoscale does the flexoelectric effect become appreciable. Since the magnitude of the induced polarization depends on both the magnitude of the flexoelectric coefficient, which is relatively small, and the strain gradient, it is the strain gradient terms which must become large to cause the polarization. Such large strain gradients are only feasible at small length scales where larger materials would experience catastrophically large amounts of strain.

For example, if a strain gradient of 0.1 % nm^{-1} is needed to create a significant flexoelectric polarization, a material which is only 10 μm thick would experience 500 % compressive strain on one surface and 500 % tensile strain on the other surface. This would surely cause mechanical failure in a huge majority of materials useful for electronics. Alternatively, in a material which is 10 nm thick, the same strain gradient would only create strains of 0.5 % on the sample surfaces. This level of strain is considerably more realistic for materials to experience and withstand. The same reasoning can then be applied to 2D materials to claim that sufficiently large strain gradients can be produced to create noticeable flexoelectric polarization.

1.3.3. Electromechanical Coupling in 2D Materials

Recently, piezoelectricity and flexoelectricity have begun to be studied in 2D materials, adding to the long list of intriguing characteristics of this family of materials[38,39]. Studies of piezoelectricity within 2D materials have already yielded strong experimental work, but the study of 2D material flexoelectricity is still in its infancy. The polarization and strain relation in materials is summarized in the equation

$$P_i = e_{ijk}\varepsilon_{jk} + \mu_{ijkl}\frac{\partial \varepsilon_{jk}}{\partial x_l}, \quad (1.1)$$

where the first term represents the piezoelectric contribution and the second term represents the flexoelectric contribution[10]. A few papers have theoretically[16,40–43] and experimentally[44–48] explored piezoelectricity in a wide range of 2D materials. Flexoelectricity, on the other hand, is relatively understudied in 2D materials even though its sub-nanometer thickness affords a potentially great platform for its study. The main reason for the lack of study of flexoelectricity seems to be due to the lack of awareness mentioned in the previous section, deceptively small flexoelectric coefficients, and measurement difficulties. At larger length scales, the strain gradient in Equation (1.1) will be small, silencing the flexoelectricity term, but this is not necessarily the case in nanoscale systems.

On the theoretical side, there has been a handful of studies exploring the polarization arising from the curvature of 2D materials. Most studies to date focus on carbon systems[31,49–51] and hexagonal boron nitride (h-BN)[52–54], but a few touch upon TMDs[54]. Carbon systems, such as curved graphene[38] and graphitic nanocones[50], are theorized to have out-of-plane polarization that arises from the curvature of sp^2 bonds and the redistribution of the electron gas in the normal direction. In contrast to carbon systems, h-BN tends to have curvature induced in-plane polarization. Bilayer h-BN was found to have enhanced electromechanical coupling compared to monolayer[53], but monolayer h-BN

has still been calculated to have non-zero in-plane polarization when in a corrugated shape[52]. Flexoelectricity can also be used to induce piezoelectric-like properties in non-piezoelectric 2D materials if non-symmetric holes are created in the material[33].

On the experimental side, studying flexoelectricity can be very difficult, even for bulk material. Isolating the flexoelectric effect completely from the piezoelectric effect is challenging. Plus, experiments for measuring flexoelectric coefficients often gives results that can be orders-of-magnitude different from calculations[10]. Currently, the most promising experimental evidence for flexoelectricity in 2D materials is obtained using a method called PFM. In this method, a conductive atomic force microscopy (AFM) tip is brought into contact with a sample to apply an alternating electric field[55]. The electric field causes a piezoelectric sample to expand/contract due to the converse piezoelectric effect, and this movement is measured by vertical displacement of the AFM tip. This technique is typically used to study piezoelectric and ferroelectric materials, but it can potentially be used to study flexoelectricity if the electric field originating from the AFM tip is spatially varying, taking advantage of converse flexoelectricity. Alternatively, non-symmetric feature can be inserted into 2D materials to cause a non-uniform electric field distribution within the material to cause a non-piezoelectric material to exhibit piezoelectric-like behavior. This has been done with graphene nitride nanosheets containing triangular holes where a PFM was used to detect electromechanical coupling thought to originate from the flexoelectric effect[55]. Additionally, PFM was used to measure piezoelectricity in Janus monolayer TMDs[48], which do have intrinsic out-of-plane piezoelectricity, and to detect changes that MoS_2 has on the properties of underlying ferroelectric materials[56,57].

The theoretical and experimental study of flexoelectricity in 2D materials has just begun and has much potential for future discoveries. Very little experimental work has

been published on this topic and represents an area where any contribution can have a huge impact on the entire field.

1.4. INTRODUCTION TO ATOMIC FORCE MICROSCOPY

1.4.1. General Overview

Different modes of atomic force microscopy (AFM) are used throughout this research. In general, AFM is a method to measure the topography of a sample surface to a very high level of resolution. A small pointed tip, anywhere from the order of a nanometer to a hundred nanometers, interacts with the surface to cause the bending of a cantilever. The cantilever deflection is then measured by reflecting a laser off the back of the cantilever and into a position sensitive photodiode. The amount of deflection of the laser is used to move the AFM probe tip up or down to cause cantilever to be at a constant level of deflection. The AFM probe is then scanned along the surface of the sample, performing the process of deflection correction at each point on the surface. This creates a topographic map of the surface by recording how much the tip needed to be moved up or down at each point. In this work, 'AFM tip' will refer to the pyramidal structure which contacts the sample, 'AFM cantilever' will refer to the cantilever which suspends the AFM tip, and 'AFM probe' will refer to the entire product. Schematic illustration of a generic AFM probe is shown in Figure 1.3.

There are many different modes of AFM, including mechanical[13,58], electrical[59], magnetic[60], and electrochemical modes[61], all of which revolve around the principle of a very fine probe tip interacting with a surface. The two most common methods of measuring surface topography are tapping mode and contact mode, which will be discussed in the following sections. Both techniques are used in this work to obtain high resolution height images of sample surfaces containing 2D materials. Additionally, PFM, which is a type of

contact mode measurement, is used extensively in this work to detect electromechanical coupling in 2D materials and will be discussed in depth in Chapter 3.

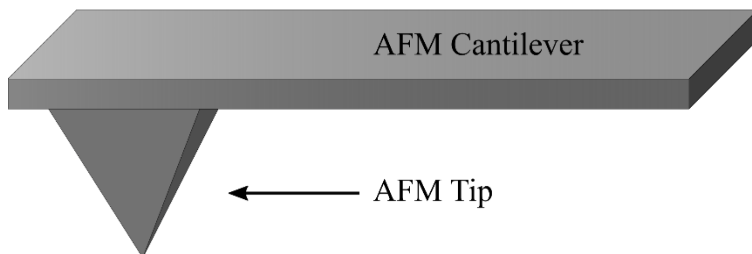

Figure 1.3 An example of a generic AFM probe. The entire structure is referred to as the probe with pyramidal structure called the tip and the long supporting rectangular prism being called the cantilever. The radius of curvature refers to how wide the apex of the tip is when fit to a sphere.

1.4.2. Tapping Mode

Tapping mode AFM is the most common way to capture topographic images of sample surfaces. It is often used to measure the height of materials and has become the standard way to characterize 2D materials. The height of sample features which are resolvable by this technique range from sub-nanometer to about 10 μm. The limiting factor for the larger end of this range is due to the limit of the actuator, which physically moves the AFM probe up and down. The actuator is constructed from a piezoelectric element which will expand and contract with an applied voltage from the AFM controller circuitry to precisely control the AFM probe height. The lateral resolution is controlled by the radius of curvature of the AFM tip.

In the tapping mode configuration, the AFM probe is oscillated up and down above the sample surface as shown in Figure 1.4. The amplitude of the oscillations is called the tapping amplitude and the distance above the sample is defined as the amplitude setpoint. In a tapping mode measurement, an amplitude setpoint is selected by the user and corresponds to a certain tapping amplitude. As the AFM probe is scanned along the sample

surface, if the sample height increases the tapping amplitude will decrease, and if the sample height decreases the tapping amplitude will increase. The AFM controller will then raise or lower the AFM probe tip so that the tapping amplitude will remain constant. That is to say that the system automatically moves the tip up and down to keep the tip at a constant distance above the sample surface, the amplitude setpoint.

This method imparts low stress onto the sample as the only times that the AFM tip touches the sample surface are at the minima of its tapping motion. To minimize the force exerted on the sample from the tip, the amplitude setpoint can be set to a large value so that the tapping amplitude barely interacts with the surface. The amplitude setpoint can be lowered if a more precise measurement of the sample surface is needed[62]. Because tapping mode can have little interaction with the sample surface while still obtaining a high quality topographic image, it is the preferred method to obtain high resolution topographic images of sample surfaces.

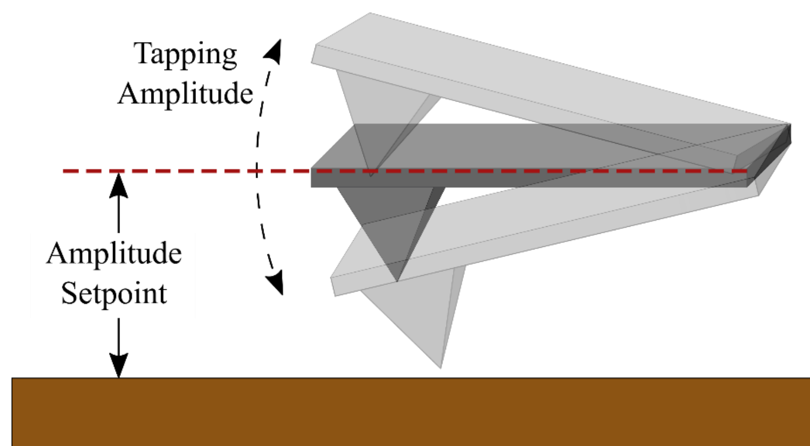

Figure 1.4 An illustration of tapping mode AFM. An AFM probe oscillates above a sample surface whose amplitude is defined as the tapping amplitude. The distance above the surface is called the amplitude setpoint and can be defined by the user.

1.4.3. Contact Mode

Contact mode AFM operates on a similar principle as tapping mode. In this case the AFM probe does not oscillate above the sample surface, but it is constantly in direct contact with the sample surface. First the AFM tip is brought barely into contact with the sample surface, which will cause the cantilever to bend. Then the system will extend the probe further so that the AFM cantilever deforms a specific amount defined by the user, called the deflection setpoint. This value is defined in Figure 1.5. A smaller deflection setpoint will impart less force on the sample and tip, while a larger deflection setpoint will obtain a more accurate image of the sample surface while imparting greater forces. The AFM till will then rub across the surface of the sample during a scan. The AFM controller moves the AFM probe up and down with the sample topography to keep a constant deflection setpoint.

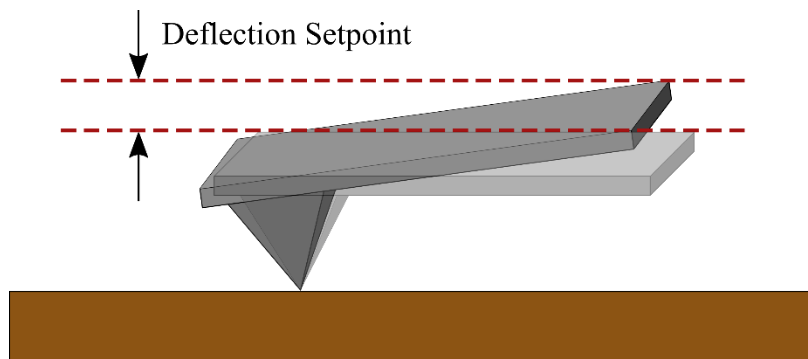

Figure 1.5 An illustration of contact mode AFM. An AFM probe is brought into contact with a sample surface and caused to deform a certain amount defined as the deflection setpoint.

The constant contact of the AFM tip on the sample surface has a few consequences. First, both the AFM tip and the sample surface can be damaged. Imaging the sample in this way requires a more robust sample which does not deform easily. Also, the AFM tip must be harder to prevent wear and tear. Contact mode AFM tips will also typically be

larger than tapping mode AFM tips so they can last a longer time without wearing down. A downside of this is that the lateral resolution will often be worse in contact mode AFM because of the greater size of the AFM tip.

Being in constant contact with the sample surface allows for other types of measurements to take place beyond topography. If the AFM probe is conductive, electrical measurements can be performed on the sample. PFM takes advantage of this possibility by using a conductive AFM probe to apply an electric field through the sample while simultaneously using the contact mode AFM electronics to measure the resultant sample deflection. This method will be discussed in more detail in Chapter 3.

1.5. Overview of Dissertation

The goal of the next few chapters is to present the research which has been accomplished towards the goals of gaining a better understanding of 2D materials and electromechanical coupling. Chapter 2 looks at developing a method to measure the adhesion between 2D materials and soft substrates. Efforts to do this in literature are lacking due to the difficulty of translating traditional methods developed on hard substrates to soft substrates. The knowledge gained in this chapter helps accomplish the present research goals by providing a measure of how well a 2D material can adhere to a soft substrate and offers insights into 2D material transfer characteristics for fabrication of devices.

Chapter 3 explores the measurement technique called piezoresponse force microscopy. This technique is pivotal to understanding the meaning of the measurements taken on 2D materials. A brief overview is first given on the PFM process followed by a detailed explanation of how the measurement is performed and analyzed. The process is

inspired by previous literature, but much has been adapted to specifically analyze the 2D material samples created for this work.

Chapter 4 uses the PFM technique to measure out-of-plane electromechanical coupling of monolayer MoS_2. This is the first measurement of its kind and offers an estimate of the magnitude of the electromechanical response. Out-of-plane piezoelectricity in MoS_2 should not be allowed due to symmetry arguments, which is one reason that this response is argued to be a flexoelectric effect. This would also be the first experimental evidence of out-of-plane flexoelectricity in monolayer MoS_2.

Chapter 5 explores the out-of-plane electromechanical responses of a suite of TMD materials using the processes developed in the previous chapters. It is found that $MoSe_2$, WS_2, and WSe_2 also exhibit out of plane electromechanical coupling like MoS_2. The magnitude of their responses can then be compared to each other to track trends with other parameter differences between the materials. One trend that becomes visible and may be predicted by the flexoelectric effect, is that the magnitude of the responses tends to follow the ratio of the dielectric susceptibility to the lattice constant of the material. This is further evidence that the observed effect could be flexoelectric in origin and could give insights into the fundamental understanding of flexoelectricity.

Finally, Chapter 6 concludes the research presented in the previous chapters. Conclusions from this work are given along with interesting future experiments which may result in interesting findings. Overall, the goal of this research is to increase the knowledge of 2D materials and electromechanical coupling, and especially the combination of the two. Although the motivating application has been energy harvesters for wearable electronics, the results of this research have become broader and generally applicable to a wider variety of fields.

Chapter 2:

Measuring Adhesion of 2D Materials on Soft Substrates[ii]

A vast array of applications has arisen for 2D materials, including their use in stretchable and flexible electronics. Additionally, 2D materials typically need to be transferred from one substrate to another using a soft stamp to create a device. Both areas, fabrication and deformable device functionality, rely on the knowledge and controllability of adhesions between 2D materials and soft substrates. In this chapter, a method to measure the adhesion between 2D materials and soft substrates is developed using MoS_2 and PDMS.

[ii] Brennan, C. J.; Nguyen, J.; Yu, E. T.; Lu, N. Interface Adhesion between 2D Materials and Elastomers Measured by Buckle Delaminations. *Adv. Mater. Interfaces* **2015**, *2* (16), 1500176.
Author Contributions: C.J.B. performed AFM measurements, data analysis, sample fabrication, and wrote paper; J.N. performed sample fabrication; E.T.Y. supervised and coordinated project; N.L. supervised, coordinated and developed project idea.

2.1. INTRODUCTION

Interest in 2D materials has grown quickly due to their low profile[18], high deformability[63], visual transparency[64], and superior electronic performance[65]. Potential applications of 2D materials include transparent electronics[19], chemical sensors[25], and flexible electronics[27]. With the emergence of stretchable electronics[66,67] and bio-integrated electronics[2,3], many more opportunities for 2D materials await to be explored.

In general, fabrication of 2D electronic systems involves transferring the 2D material from one substrate to another in a process called transfer printing[68,69]. This process relies heavily on the interactions between the 2D material and the various surfaces that it contacts. Adhesion values must allow for the transfer from one substrate to another. By gaining a better understanding of the adhesion energy between 2D materials and the various substrates involved, the transfer process can be improved to allow for the picking up and printing of 2D materials onto arbitrary flexible and stretchable substrates.

Adhesion of 2D materials is also a controlling parameter for device mechanics. As a component in an integrated device, a 2D material will have to make secure contact with supporting substrates, metallic interconnects, other 2D materials, encapsulation layers, and other elements of a complete system. The mechanical interaction between 2D materials and their neighbors is an important parameter that governs the mechanical integrity of the device during thermal and mechanical loadings. Mechanical loading is often prominent during the operation of flexible 2D devices. For example, strain engineering of 2D materials on polymer substrates can be achieved by deforming the substrate[70], but any slippage between 2D materials and the substrate would weaken the strain transfer to the 2D materials and hence limit the tunability on electronic properties. Moreover, slippage between 2D materials and their polymer substrates when the substrate is deformed may

lead to buckle delaminations or wrinkles when the substrate is unloaded[71], resulting in device degradation.

Because of the significance of adhesion, many experimental studies have been carried out to measure the adhesion energy between graphene and stiff substrates, as summarized in a recent review paper[72]. For example, adhesion energy between exfoliated monolayer graphene and SiO_2 has been measured to be 450 mJ m^{-2} by a pressurized blister method[73], while adhesion of chemical vapor deposited (CVD) monolayer graphene to Si measured by the double cantilever peeling method is found to be 357 mJ m^{-2}. Adhesion between CVD graphene and seed copper has been measured to be 720 mJ m^{-2} using cantilever method[74] whereas after transferring CVD graphene to a foreign copper surface, the interface adhesion was found to be only 510 mJ m^{-2} using a blister test[75].

Adhesion between graphene and stretchable substrates is much less investigated due to the difficulty of handling soft substrates. In one study, the lower bound of the adhesion energy between exfoliated graphene and polydimethylsiloxane (PDMS) elastomer has been estimated to be 7 mJ m^{-2} by probing the conformability of exfoliated graphene on a pre-corrugated PDMS surface[76]. In another study, the adhesion energy between exfoliated graphene and a polyethylene terephthalate (PET) substrate has been estimated to be 0.54 mJ m^{-2} from buckling analysis, but the buckle profile measured by the AFM is of low resolution in this work and the authors called for more accurate experiments[77].

Buckling and wrinkling are instability phenomena often observed when stiff membranes are bonded to compliant substrates[78], and have been harnessed to create stretchable electronics out of intrinsically brittle, inorganic semiconductor nanoribbons[79–81] and graphene[82,83]. In addition, wrinkle-based metrology has been applied to probe the mechanical properties of thin films[84,85] and buckle-delamination-based metrology has been

used to measure film-to-substrate adhesion[86–88]. In this work, both wrinkle-based and buckle-delamination-based metrologies on 2D materials bonded to soft elastomeric substrates are used. Concomitant wrinkles and buckle delaminations can be created in the same MoS_2 flake exfoliated onto a PDMS substrate. Fitting the buckle delamination profile allows for the calculation of the adhesion between the MoS_2 and the PDMS, but requires very accurate knowledge of the width and height of the buckle delamination as well as the thickness of the MoS_2 flake. Instead of using an AFM step height measurement or Raman spectroscopy, fitting the wrinkle profile can yield more accurate flake thicknesses. Applying these two methodologies on the same MoS_2 flake provides a very simple but reliable process to calculate the adhesion between few layer MoS_2 and PDMS.

In this chapter, first the preparation of the samples is discussed, including the PDMS fabrication, MoS_2 exfoliation, and buckle formation. Next the results of the fabrication are shown, where wrinkles and buckle-delaminations are easily distinguishable in optical microscopy and AFM measurements. The fitting process is then discussed as well as the thickness and adhesion calculation procedures. Finally, uncertainty of the measurement is considered and followed by discussion about the importance of this work and applications.

2.2. EXPERIMENTAL METHODS

2.2.1. PDMS Preparation

PDMS is used as the soft, polymer substrate in this study of adhesions. PDMS samples were created in lab using the Sylgard® 184 Silicone Elastomer kit in a 10:1 mixing ratio of polymer to curing agent. The two components are mixed in a plastic cup with a glass rod by stirring the mixture in a counter-clockwise pattern for five minutes. It is

important to only stir in a single direction, so the polymer chains are aligned in a single direction.

After the components have been mixed, the liquid is poured into a Petri dish which determine the shape of the cured PDMS. At this stage, the mixture will have bubbles trapped inside and curing the sample at this point would create a low-quality, unusable PDMS sample. To remove the bubbles, the sample is placed inside a desiccator connected to a pump. A weak vacuum is created inside the chamber which draws out the bubbles within the PDMS mixture due to the pressure difference. The bubbles are removed after about 45 – 60 minutes inside the desiccator. Finally, the mixture is placed inside a 70 °C oven for 4 hours to cure into a solid piece of PDMS.

The cured PDMS has a typical RMS surface roughness of 1.0 – 2.3 nm across the tapping-mode AFM measurements performed in this study. The top, free surface of the cured PDMS is always used because the bottom surface will take the shape and roughness of the curing container. No pretreatment of the PDMS surface was done prior to the MoS_2 transfer besides cleaning the surface with Scotch tape. The intrinsic adhesion between PDMS and MoS_2 is of interest and any other surface treatment may affect the surface chemistry of the PDMS, changing its adhesive properties.

2.2.2. MoS_2 Exfoliation

Exfoliated MoS_2 flakes are used to study the adhesion of MoS_2 to soft substrates. The exfoliation method was the first fabrication process developed in the field[17], and is still the simplest and least cost prohibitive way to create monolayer and few-layer flakes of MoS_2. The downside is the poor yield of monolayers and uncertain repeatability. Nevertheless, this method remains one of the most popular among research groups studying

the mechanical and electrical properties of MoS_2 and often gives better quality samples than using grown MoS_2.

A synthetic bulk MoS_2 crystal obtained from 2D Semiconductors Inc. is used as the source material. The crystal is placed on a piece of blue polyethylene cleanroom tape and then peeled off. A small portion of the crystal will remain adhered to the tape. Next, the tape is folded over so that MoS_2 is sandwiched. Unfolding the tape splits the MoS_2 into two regions, thinning the crystal and creating a larger coverage of MoS_2 on the tape. This process is typically done 3-6 more times to further thin the MoS_2 and to increase coverage on the tape. The increased coverage on the tape is desired to yield a larger amount of transferred MoS_2 area onto a receiving substrate.

Typically, stiff SiO_2 is used as the receiving substrate, but for this study the MoS_2 is transferred onto the polymer PDMS. PDMS is used because of its stretchability and softness which could be a future platform for stretchable electronics, but more importantly for this study, allows for the easy formation of buckle-delaminations and wrinkles. PDMS offers different challenges than SiO_2 for obtaining a good transfer. First, PDMS is viscoelastic[89] which causes the speed at which the MoS_2/tape is peeled off the PDMS to affect the amount of transferred MoS_2. Removing the tape slowly transfers virtually no MoS_2 to the PDMS, but quickly removing the tape transfers a large amount of MoS_2. The amount of MoS_2 transferred to the PDMS is greater in both surface coverage and thickness than what is usually transferred to SiO_2. A higher amount of surface coverage means that there are more potential areas of useable MoS_2, but unfortunately, most of the transferred MoS_2 is thick and can be considered bulk. The thin (< 10 monolayers) areas of MoS_2 also tend to be along the edges of thicker flakes. Isolated, thin MoS_2 flakes are not as common as the thicker flakes. The MoS_2 does have a visible contrast difference against the PDMS even down to monolayer thickness in reflective mode microscopy. Since PDMS is

transparent, a transmission mode microscope can be used to image the MoS_2 and could be used to calculate the percent of light transmitted per layer in MoS_2[20,90]. Examples of exfoliated flakes of MoS_2 on PDMS imaged using reflection mode and transmission mode microscopes are shown in Figure 2.1 (a) and 2.1 (b), respectively.

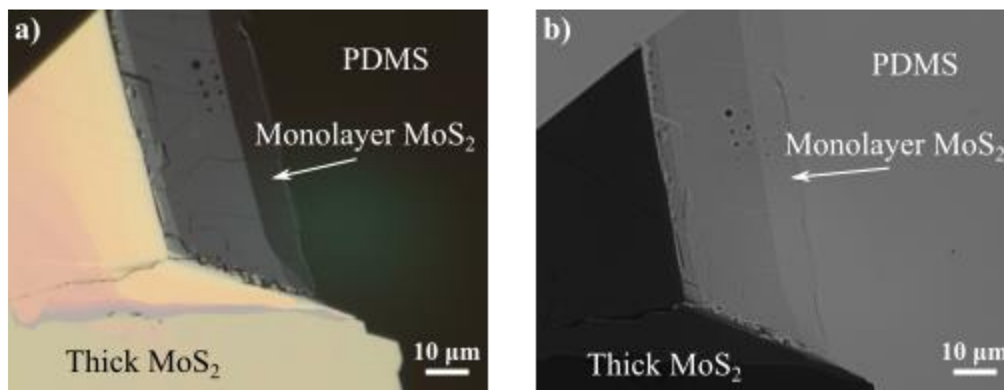

Figure 2.1 Optical images of exfoliated MoS_2 on a PDMS substrate imaged using reflection mode (a) and transmission mode (b). The array of dark dots is from laser damage incurred during Raman spectroscopy measurements.

2.2.3. Buckle Formation

Buckling of a thin film on a soft substrate can refer to the formation of buckle-delaminations or wrinkles. Buckle-delaminations have been used in this work to study the adhesion of MoS_2 and PDMS and wrinkles are used as an independent method to measure of MoS_2 thickness. The main fabrication method used to create the buckles is a process called spontaneous buckling. It was discovered that buckle-delaminations and wrinkles can be formed in MoS_2 simply by exfoliating onto PDMS. The buckles originate from the huge elastic mismatch between MoS_2 and PDMS: the Young's modulus of MoS_2 is 0.27 TPa[15] while that of PDMS is 1.8 MPa[91].

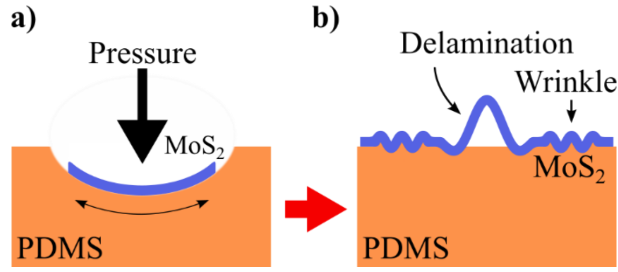

Figure 2.2 Schematic of the spontaneous buckling process. (a) First, the pressure of exfoliation process locally expands the PDMS surface. (b) Next, the release of the pressure lets the PDMS surface relax, transferring compressive strain to the MoS_2 that causes buckling.

The mechanism believed to form the buckles is schematically illustrated in Figure 2.2. During the transfer of the exfoliated MoS_2 flakes to the PDMS from the tape, a small amount of pressure is created by pressing down on the tape to make good contact. Since the PDMS is so soft, it deforms slightly causing a local expansion of its surface. At this point, the MoS_2 adheres to the expanded PDMS surface. Once the pressure is released, the PDMS surface rebounds to its original, flat configuration and the MoS_2 follows. Effectively, the MoS_2 experiences a compressive strain caused simply by the exfoliation process.

The compressive strain causes the stiff thin-film MoS_2 to buckle on top of the soft, elastomeric PDMS. First, wrinkling will occur where the MoS_2 is still in contact with the PDMS surface. With increasing compression, the wrinkles will turn into buckle-delaminations, separating the MoS_2 from the PDMS surface over a short region. Due to the huge elastic mismatch between the two materials, the critical strain for buckling is very low and can be calculated[92] to be 0.02 % using the equation

$$\varepsilon_c = \frac{1}{4}\left(\frac{3\bar{Y}_s}{\bar{Y}_f}\right)^{\frac{2}{3}}. \tag{2.1}$$

The plane-strain modulus of MoS_2 and PDMS are $\bar{Y}_f$= 0.288 TPa and $\bar{Y}_s$ = 2.40 MPa, respectively. The plane-strain modulus is defined as $\bar{Y} = Y/(1-\nu^2)$, where Y and ν are the Young's modulus and Poisson's ratio of the film, respectively.

Using this method assumes that some slippage occurs during the initial contact of the MoS_2/tape to the PDMS. In order for the MoS_2 to experience the compressive force of the surface rebounding, the MoS_2 must adhere to the PDMS while it is locally expanded from the pressure of the transfer. Although this process was repeatable over a few samples, the yield was low and proper buckle-delaminations tended not to form in monolayer flakes[90].

A second method was also used to create buckles in the MoS_2 flakes. This method, called pre-stretching, is widely used and is the standard in literature[81,82,90,92] to create buckles in thin, rigid films on soft substrates. The pre-stretching method creates buckles by adhering a thin rigid film to a tensely strained substrate and then releasing the tensile strain. The thin film undergoes compressive strain as a result of the substrate relaxation. Depending on the elastic mismatch, amount of pre-stretch, and the strength of adhesion, the film layer will either wrinkle or buckle-delaminate. A schematic of this process is depicted in Figure 2.3. Although this process also created buckles, it was not found to be more successful than the spontaneous method.

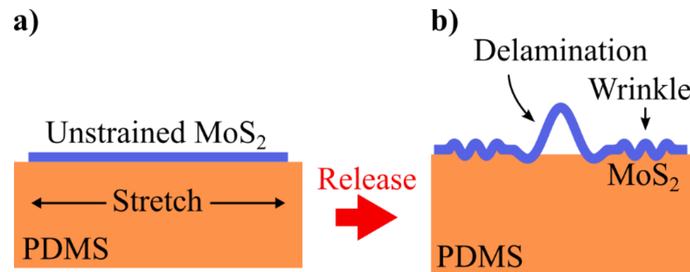

Figure 2.3 Schematic of the pre-stretch process. (a) MoS_2 is transferred on top of a stretched PDMS substrate and then the strain is released (b) to form buckle-delaminations and wrinkles.

With the relatively same success rate, spontaneous buckling was focused on since it requires less sample preparation. Figure 2.4 (c) shows an example of an MoS_2 flake on PDMS with both buckle-delaminations and wrinkles that were formed using the spontaneous buckling procedure. Also shown are the definitions of the buckle-delamination height, δ, width, λ, and film thickness, h, in Figure 2.4 (a). Figure 2.4 (b) defines the wrinkle amplitude, A, and wrinkle period, λ_w.

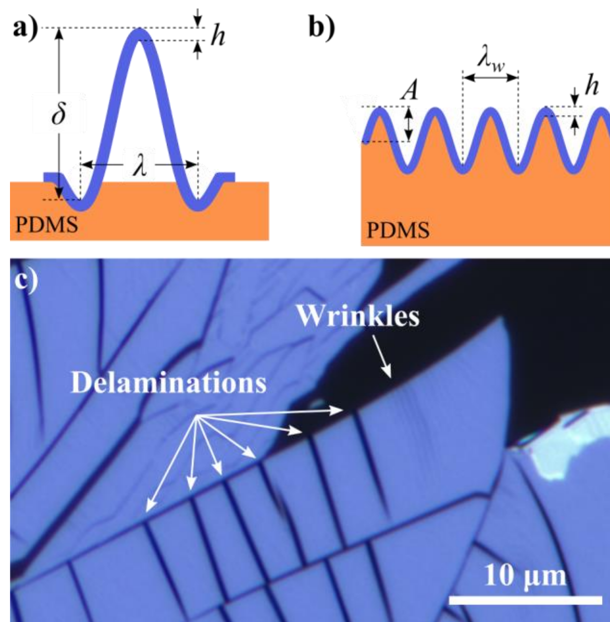

Figure 2.4 Schematic defining the parameters of (**a**) buckle-delaminations and (**b**) wrinkles. An optical image of MoS_2 on PDMS with buckle-delaminations and wrinkles is shown in (**c**). This sample was created using the spontaneous buckling method.

2.3. Results and Discussion

2.3.1. Determination of MoS_2 Flake Thickness

The strength of adhesion between 2D materials and soft, stretchable substrates is important if flexible and wearable electronics are to be made from this material. A first step towards understanding the adhesion between 2D materials and soft substrates is to

develop a method to measure it reliably. Such a method has been developed here by measuring the height profile of buckle-delaminations and wrinkles of exfoliated MoS_2 on PDMS. The first important step of the process is to obtain an accurate measurement of the thickness of MoS_2 because MoS_2 thickness strongly influences the final adhesion calculation.

Obtaining accurate measurements of MoS_2 thickness, h, proves to be a more difficult task than simply taking a step height measurement using the AFM. The large elastic mismatch between the MoS_2 and the PDMS substrate results in an artificial increase in the AFM step height measurement compared to the actual thickness of the MoS_2 flake. Such effects have also been seen previously with MoS_2 on soft Gel-Films®[90], for which the MoS_2 thickness was estimated using a combination of Raman spectroscopy, PL spectroscopy, and transmittance measurements. Other concerns have been raised regarding the reliability of AFM step height measurements of graphene on stiffer materials than PDMS, such as SiO_2[62], suggesting that there may be some uncertainty in AFM measurements at the scale of few-layer 2D material thickness. Despite these issues, AFM scanning profiles of wrinkles and buckle-delaminations within one MoS_2 flake are still reliable as long as there is no abrupt change in material stiffness.

To remedy this problem, wrinkle-based metrology is used to determine the actual MoS_2 thickness. To be able to use this method for adhesion measurements, the extra requirement of having coexisting wrinkles and buckle-delaminations on the same MoS_2 flake must be met. Fortunately, it is theoretically possible[93] and has been observed in multiple flakes. The thickness and the amount of pre-strain present in the system at the time of transfer can then be calculated simultaneously by fitting the sinusoidal wrinkle profile. Wrinkles can be distinguished from buckle-delaminations by their periodic sinusoidal shape as opposed to a singular sinusoidal peak. The amplitude, A, and

wavelength, λ_w, of the wrinkled system subjected to a compressive strain ε_{pre} beyond the critical strain of wrinkling are captured by the postbuckling solutions[92]

$$A = \frac{A_0}{\sqrt{1+\varepsilon_{pre}}(1+\xi)^{1/3}}, \quad (2.2)$$

$$\lambda_w = \frac{\lambda_0}{(1+\varepsilon_{pre})(1+\xi)^{1/3}}, \quad (2.3)$$

respectively. Figure 2.4 (b) schematically shows the definitions of the parameters and $\xi = 5\varepsilon_{pre}(1 + \varepsilon_{pre})/32$. A_0 and λ_0 are the amplitude and period at the onset of wrinkling at a critical strain point and are given, respectively, as

$$A_0 = h\sqrt{\frac{\varepsilon_{pre}}{\varepsilon_c} - 1}, \quad (2.4)$$

$$\lambda_0 = 2\pi h\left(\frac{\bar{Y}_f}{3\bar{Y}_s}\right)^{1/3}. \quad (2.5)$$

The critical strain of wrinkling, ε_c, is given by Equation (2.1). Using this set of equations, h and ε_{pre} can be used as fitting parameters to extract the film thickness when the wrinkle amplitude and period are known.

Figure 2.5 shows a tapping-mode AFM image of two wrinkled flakes of MoS_2 on PMDS with height profiles provided for cuts along the blue lines. Figure 2.5 (a) is the same wrinkled area shown optically in Figure 2.4 (c). The amplitude and wavelength values are determined using a fitting algorithm implemented in MATLAB by fitting the equation

$$w(x) = A\cos\left(2\pi\frac{x - x_{off}}{\lambda_w}\right) + y_{off} \quad (2.6)$$

to the data obtained from the AFM measurement data. Here, $w(x)$ represents the height of the wrinkle at a given point x, and x_{off} and y_{off} are the x and y coordinate offsets, respectively. From the data, the thickness of the MoS_2 flakes shown in Figure 2.5 (a) and Figure 2.5 (b) are calculated to be 3.83 ± 0.3 nm and 3.04 ± 0.3 nm, respectively.

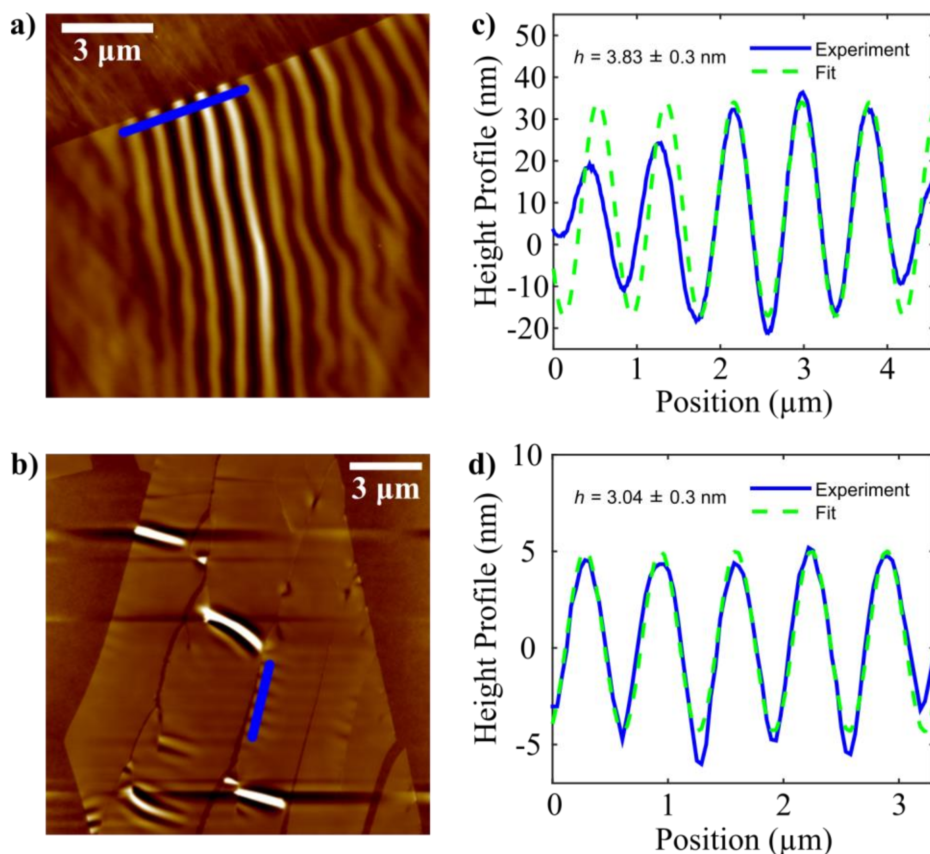

Figure 2.5 AFM images (a, b) of two different MoS_2 flakes on PDMS. Cross-sectional height profiles of the wrinkles along the blue lines in the AFM images are given to the right of each (c, d). The green dashed line in each height profile is the MATLAB fit to the AFM experimental data.

These two values suggest that the two samples differ by a thickness of 0.79 nm, or about one monolayer of MoS_2[19,94–98]. The MoS_2 flake shown in Figure 2.5 (a) is then 5-6 layers thick with a layer thickness of 0.77 nm or 0.64 nm respectively, while the MoS_2 in Figure 2.5 (b) is 4-5 layers thick with a monolayer thickness of 0.76 nm or 0.61 nm respectively. All these monolayer thicknesses are within the ranges of values given by different literature reports. Studies of the interlayer spacing of bulk MoS_2 flakes using methods other than AFM have reported values[95–97] of 0.60 – 0.65 nm with more recent studies[96,97] converging on 0.65 nm. When AFM step height measurements of monolayer

MoS_2 are reported[19,94,98], thicknesses range from 0.6 – 0.9 nm, tending to be on the larger side of this range. These discrepancies suggest that measured heights of monolayer MoS_2 flakes tend to be slightly larger than the interlayer distance and support that AFM step height measurements may not be sufficient for highly accurate measurements of few-layer MoS_2 thickness.

2.3.2. Calculation of Adhesion

With accurate knowledge of the MoS_2 flake thickness, the adhesion can now be calculated from the profile of a buckle-delamination. Linear elastic fracture mechanics offers a simple formula to calculate the adhesion energy, also known as the interface toughness, from the buckling profile as[88]

$$\Gamma = 2\pi^4 \frac{B\delta^2}{\lambda^4}, \tag{2.7}$$

where Γ is the adhesion energy, B is the bending stiffness of the film, δ is the buckle-delamination height, and λ is the buckle-delamination width. Conveniently, this equation does not depend on the compressive strain that induced the buckles. Next, $B = \bar{Y} \cdot h^3/12$ where h is the film thickness and $\bar{Y}$ is the plane strain modulus is substituted into the equation. The interface toughness can then be expressed in terms of the film thickness, buckle height, and buckle width as

$$\Gamma = \frac{\pi^4}{6} \frac{h^3\delta^2}{\lambda^4} \frac{Y}{1-\nu^2}. \tag{2.8}$$

Since the mechanical properties of MoS_2 have been previously measured[14,15] and simulated[99], its Young's modulus[15] $Y = 0.27$ TPa and Poisson's ratio[99] $\nu = 0.25$ are taken from the literature.

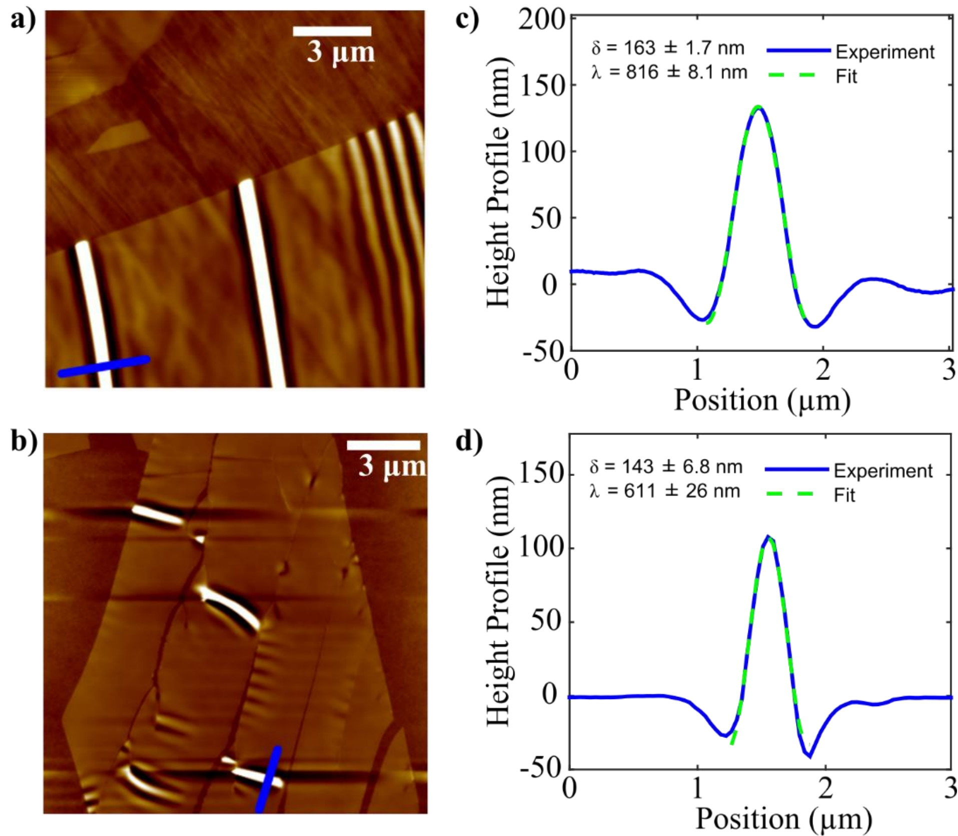

Figure 2.6 AFM images (a, b) of two different MoS_2 flakes on PDMS. Cross-sectional height profiles of the buckle-delaminations along the blue lines in the AFM images are given to the right of each (c, d). The green dashed line in each height profile is the MATLAB fit to the height profile.

Figure 2.6 shows AFM topographic images and cross-sectional line profiles of the same two flakes of MoS_2 as in Figure 2.5. MoS_2 buckle-delaminations and wrinkles are the same thickness because no layer steps between the features are seen in either the AFM or optical images. Buckle-delaminations in MoS_2 flakes are distinguished from other features by their sinusoidally shaped peaks flanked on either side by smaller depressions, as illustrated in Figure 2.4 (a). They can also be seen in Figures 2.6 (a) and Figure 2.6 (b) as bright streaks running across the MoS_2 flakes. Height profiles along the blue lines in

the AFM images are shown in Figure 2.6 (c) and Figure 2.6 (d). The profiles are then fit to the buckle-delamination profile[88]

$$d(x) = \frac{\delta}{2}\left(1 + \cos\frac{2\pi(x - x_{off})}{\lambda}\right) + y_{off}, \quad (2.9)$$

using a MATLAB least-squares fitting function to obtain δ and λ. Here, *d(x)* is the buckle-delamination height at a given point x along the buckle-delamination cross-section, x_{off} and y_{off} are coordinate offsets, and the line thickness in the figures is for clarity and not to indicate averaging. The fits are shown by the dashed lines in Figure 2.6 (c) and Figure 2.6 (d) and have almost perfect overlap with the experimental data.

With all three geometric parameters in Equation (2.8) obtained through careful profile fittings, the adhesion of the few-layer MoS_2 flakes shown in Figure 2.6 to their PDMS substrates is calculated to be 16 ± 5 mJ m^{-2} and 19 ± 8 mJ m^{-2}. Table 2.1 summarizes these values as well as those from two other measured buckle-delaminations not shown. Despite different flake thicknesses and buckling profiles, the four adhesion values are consistent. Averaging over four different buckle-delaminations, the adhesion between few-layer MoS_2 and PDMS is 18 ± 2 mJ m^{-2}. This value is the first adhesion measurement of few-layer MoS_2 to a soft substrate and is higher than the lower bound found for a graphene-PDMS interface[76] (7 mJ m^{-2}). More work is needed to determine the dependence of adhesion on the number of MoS_2 layers present, including monolayer MoS_2, which was not experimentally observed to show regular buckle-delaminations formation.

Delamination	h (nm)	δ (nm)	λ (nm)	Adhesion (mJ m^{-2})
1	3.83 ± 0.3	163 ± 1.7	816 ± 8.1	16 ± 5
2	3.04 ± 0.3	143 ± 6.8	611 ± 26	19 ± 8
3	3.83 ± 0.3	188 ± 2.2	825 ± 8.1	20 ± 7
4	3.83 ± 0.3	213 ± 3.1	909 ± 9.2	17 ± 6
Average	-	-	-	18 ± 2

Table 2.1 Summary of the fit values from the buckle-delaminations and wrinkles and the resulting adhesions measurement for each MoS_2 flake.

To prove that this method is generic and can be applied to other similar systems, a reported buckle delamination of MoS_2 on Gel-Film®[90] with given height (380 ± 10 nm) and width (1100 ± 10 nm) of the buckle-delamination is analyzed. The uncertainty is added ad hoc here to account for any possible uncertainty in their measurements. Their estimate of 3-4 layers of MoS_2 is similar to the number of layers seen in this work. Using a monolayer thickness of 6.7 Å and a relatively large uncertainty, the total thickness of their flake can be estimated to be ~ 2.3 ± 0.6 nm. The adhesion calculated from the given values can then be estimated to be 6 ± 4.8 mJ m^{-2}, which is somewhat smaller than the results presented here for MoS_2 and PDMS.

2.3.3. Uncertainty Estimation

The uncertainty in measured values of the parameters h, δ, and λ must be taken into consideration when determining adhesion values. For the delamination height and width, the uncertainty is taken to be the 95% confidence interval of the MATLAB fitting process. For the thickness measurements, roughly half of the monolayer thickness, or 0.3 nm, is used for the measurement uncertainty. The values used for each variable and their associated uncertainties are shown in Table 2.1. The uncertainties for the three variables

are then propagated through Equation (2.8) to obtain the total error in the adhesion using the equation[100]

$$\sigma_{\Gamma} = \Gamma\sqrt{\left(\frac{3\sigma_h}{h}\right)^2 + \left(\frac{2\sigma_\delta}{\delta}\right)^2 + \left(\frac{4\sigma_\lambda}{\lambda}\right)^2 + \left(\frac{\sigma_E}{E}\right)^2}, \quad (2.10)$$

where σ_{Γ}, σ_h, σ_δ, σ_λ, and σ_E are uncertainties of the adhesion, MoS_2 thickness, delamination height, delamination width, and Young's modulus respectively. Equation (2.10) also incorporates the uncertainty of the Young's modulus of MoS_2 that currently exists in the literature, which is estimated to be ± 0.06 TPa. Including the uncertainty of the Young's modulus, the total uncertainty increases by roughly 1 mJ m-2.

Additional uncertainty in the buckle-delamination height and width due to perturbation of the sample during the AFM measurement is possible and should be analyzed. In this scenario, the measurement process itself could affect the shape of the buckle-delamination by imparting stress to the sample from the AFM tip during the tapping mode measurement. To test for this, the amount of force applied to the sample by the tip is changed via the amplitude setpoint value and is then extrapolated to a zero-force point. From this process, the estimated errors in the measurement of the buckle-delamination height and width from the tip-sample interaction is roughly ± 1 % for each. This uncertainty is negligible compared to the other sources of uncertainty and is neglected in the analysis.

2.4. CONCLUSIONS AND SIGNIFICANCE

A buckle-based metrology technique has been developed to measure the interface adhesion between 2D materials and elastomeric substrates. Taking advantage of the spontaneous and concomitant wrinkles and buckle-delaminations that are formed when exfoliating MoS_2 on PDMS, the width and height of the delaminations can be easily extracted from the AFM scanning profile. The MoS_2 thickness, however, must be

determined through wrinkle analysis due to the deficiency of AFM step height measurements across materials with large elastic mismatch. The adhesion between few-layer MoS_2 and PDMS is measured to be 18 ± 2 mJ m^{-2}. This value is about an order of magnitude less than reported adhesion measurements between graphene and rigid substrates while being about an order of magnitude above reported estimates of adhesion between graphene and polymer substrates such as PDMS[76] and PET[77]. The implications of this measurement point towards possible device failure induced by slippage of 2D materials against polymer substrates when deforming 2D flexible electronics[71]. Although this work focuses on MoS_2 to PDMS adhesion, the methodology is applicable to systems involving any 2D material on any soft substrate.

Chapter 3:

Piezoresponse Force Microscopy[iii]

A major part of this work has been developing the methodology and understanding behind the measurement technique called piezoresponse force microscopy (PFM). PFM is able to detect out-of-plane electromechanical coupling of samples, but its implementation and data analysis proves to be non-trivial. This chapter is dedicated to the general understanding of how the PFM measurement technique works and how to best understand the resultant signals from a given input. The understanding gained in the chapter will be crucial to the analysis performed in the following chapters.

[iii] Brennan, C. J.; Ghosh, R.; Koul, K.; Banerjee, S. K.; Lu, N.; Yu, E. T. Out-of-Plane Electromechanical Response of Monolayer Molybdenum Disulfide Measured by Piezoresponse Force Microscopy. Nano Lett. 2017, 17 (9), 5464–5471.
Author Contributions: C.J.B. performed the sample fabrication, AFM, PFM, Raman, photoluminescence, and data analysis. R.G. and S.B. provided CVD grown MoS_2 and assisted in the transfer process. K.K. assisted in AFM measurements. N.L. and E.T.Y. assisted in project design and supervised research. C.J.B., N.L., and E.T.Y. wrote the paper.

3.1. INTRODUCTION

Piezoresponse force microscopy (PFM) is a specialized version of atomic force microscopy (AFM) used to probe the electromechanical properties of materials[101,102]. It uses a conductive AFM probe to apply a voltage across a sample, and the same probe to measure the mechanical response. First developed by Günthner and Dransfeld[103], PFM was first, and predominately still, used for characterization of ferroelectric materials. The technique enables imaging of the different ferroelectric domains within a single sample by detecting electromechanical coupling that is either in-phase or out-of-phase with an applied electric field. A ferroelectric's domain direction can also be controlled where patterns can then be written into a sample using a PFM if a strong enough electric field is applied[102]. PFM is important for material characterization of ferroelectric materials with applications in data storage, non-linear optics, and material growth characterization[104].

There are other applications outside of ferroelectric material characterization, and this research will focus on using PFM to characterize the possible electromechanical response of 2D materials. There have been a few studies using a PFM to investigate electromechanical properties of 2D materials, namely on graphene-nitride nanosheets with non-symmetric holes,[55] graphene forming bonds to the underlying SiO2 substrate[105], and Janus monolayers of different TMDs[48]. In this work, PFM will be used to obtain estimates of out-of-plane electromechanical response in 2D materials

The main goal of this chapter is to describe how PFM operates and how it can be used to obtain quantitative measurements. First, the general operating principles of a PFM will be explored in further detail, followed by a discussion of the sample and AFM probe requirements for a proper PFM measurement. Next, the idealized math involved in calculating the out-of-plane electromechanical coefficient d_{33} is presented, followed by a discussion of limitations and deficiencies in PFM and why the measurement should be

referred to as an effective piezoelectric coefficient, d_{33}^{eff}. A background vector substraction process is then introduced which removes any unwanted contributions to the measurement. Calculation of the experimental uncertainty is also described followed by a general discussion of how to obtain better quality PFM images. The chapter is then ended with some concluding remarks to motivate the following chapter.

3.2 OPERATING PRINCIPLE

Said simply, PFM measures how much a sample moves when an electric field is applied through it. PFM takes advantage of the extremely high vertical resolution of an AFM and the converse piezoelectric effect to measure the small deflections caused by an applied electric field. The deflections involved can be as small as 0.1 pm and are detectable via use of a lock-in amplifier. If the amount of deflection caused by the applied voltage and consequent electric field is known, the out-of-plane converse piezoelectric coefficient of the material-under-test can be qualitatively estimated. Figure 3.1 diagrams the general setup in the PFM measurement and will be discussed in further detail.

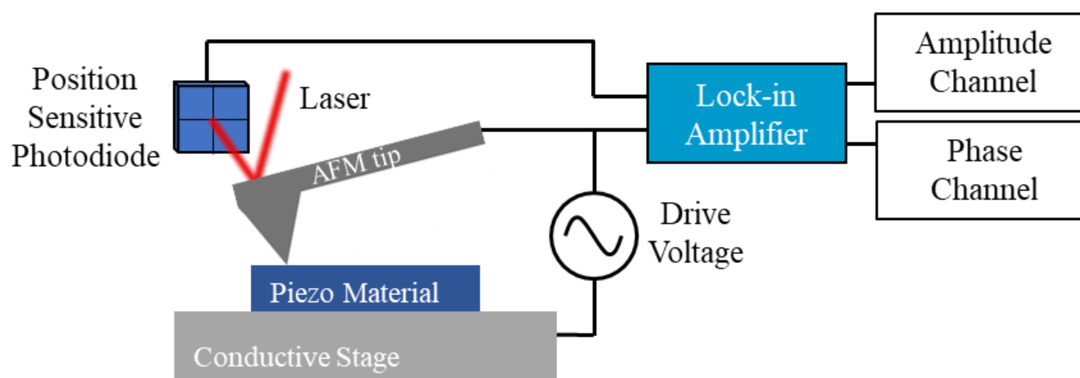

Figure 3.1 A block diagram of the PFM measurement system. An alternating voltage is applied across a sample material which will deform if it is electro-mechanically active. The deflection will then be measured by the laser in the position sensitive photodiode and amplified by the lock-in amplifier. The amplitude and phase are the two output channels of the measurement.

The PFM measurement is performed by first applying a drive voltage, V_d, between a conductive probe tip and conductive bottom electrode at a specified drive frequency, f_d. The voltage will then create an electric field through the sample material. The distribution of the electric field will depend on the thickness and material properties of the sample as well as the geometry and material of the AFM tip. The field distribution can affect the interpretation of the measured signals, but a majority of the field direction will be out-of-plane. If the sample material is electromechanically active, the alternating electric field will cause the sample to expand and contract. The expansion and contraction of the material is detected by the AFM probe because the tip is in contact with the sample, so the out-of-plane movement of the sample will cause the cantilever to bend. The bending of the AFM cantilever will then change the angle of the laser reflection off the back surface of the cantilever. The position sensitive photodiode is the sensing component which physically measures the laser deflection and produces the data for further analysis.

The signal from the position sensitive photodiode, which, to reiterate, corresponds to how much the sample is being deflected by the applied drive voltage, is then fed into a

lock-in amplifier. The drive frequency is also fed into the lock-in amplifier as the reference signal. The role of the lock-in amplifier is to isolate the frequency response measured by the position sensitive photodiode, $H_p(\omega)$, to the frequency equal to that of the reference signal which is set to the drive frequency, $H_p(\omega = f_r = f_d)$. The goal of this process is to isolate the movement of the material which is only a response of the applied electric field. The converse piezoelectric effect is theoretically not frequency dependent for the frequencies used, so the sample material should be able to respond to the drive voltage at the same frequency. All other movement measured by the position sensitive photodiode will be noise and not relevant to the measurement.

There are two outputs from the lock-in amplifier: the amplitude channel and the phase channel. The amplitude channel gives the strength of the sample's response to the applied electric field at the frequency component equal to the frequency of the drive voltage, $|H_p(\omega = f_r)|$. The phase channel gives the phase difference between the drive voltage and the sample's response in the units of degrees. The units of the amplitude channel are given in mV which represents the amount the laser was deflected in the position sensitive photodiode.

To convert the amplitude channels units from mV to a physical distance, a calibration step is needed. Figure 3.2 illustrates the calibration process using a loading curve. At a single point above the sample, the Z-piezo tube, which controls the height of the AFM probe relative to the sample, begins to extend and brings the tip closer to the sample. This stage of the process is show as the flat portion of the curve in Figure 3.2 (a) and, is depicted in Figure 3.2 (b) where the cantilever is not bent and the laser is not deflected away from the center-point of the position sensitive photodiode. Next, the Z-piezo tube is extended to the point where the AFM tip begins to interact with the sample surface via van der Waals interactions. At this point, depicted in Figure 3.2 (c), the AFM

tip ‘jumps’ to the sample surface, bending the cantilever down and deflecting the laser below the center-point of the position sensitive photodiode. This point is labeled in the curve in Figure 3.2 (a) and is where there is a slight dip below the neutral state. Finally, the Z-piezo tube is further extended, loading the sample surface with force from the AFM tip, causing the AFM cantilever to bend upward. As the tip is bent upward, the laser is deflected above the center-point in the position sensitive photodiode as shown in Figure 3.2 (d). In a proper measurement with a stiff sample and AFM probe, the portion of the curve in Figure 3.2 (a) labeled (d) should be linear and the slope represents the calibration constant. Said plainly, the calibration constant is the amount of laser displacement in the position sensitive photodiode, measured in mV, corresponding to a known displacement of the Z-piezo tube. The displacement of the Z-piezo tube is known and precisely calibrated in-factory and tuned in-lab to a reference sample with known dimensions. This process thus allows the magnitude of the laser deflection in the position sensitive photodiode to be correlated with a physical displacement of the sample. It should be noted that this calibration process physically moves the AFM probe into the sample, while in the PFM measurement, it is the sample that loads the AFM probe. These two processes are equivalent, so it is a valid method to determine the amount of physical displacement corresponding to laser displacement in a position sensitive photodiode in mV. The calculated calibration constant is called the deflection sensitivity, s_d, and is typically given in the units of nm V^{-1}.

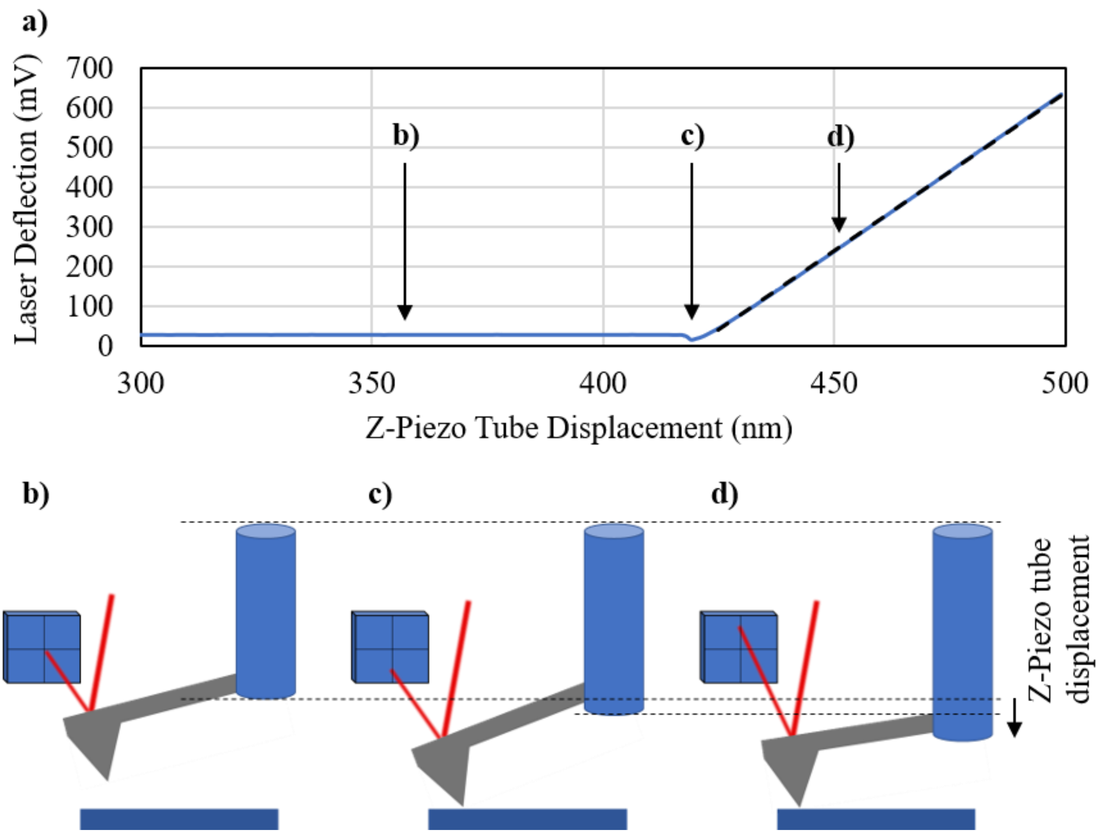

Figure 3.2 The calibration process to determine the deflection sensitivity. A typical loading curve shown in (a) illustrates each stage of the process and is labeled with a corresponding graphical representation of each mechanism. As the Z-piezo tube extends the AFM probe towards the surface but does not yet contact the surface, the laser deflection does not change (b). Once the AFM tip is close enough to the sample to interact via van der Waals forces, it 'jumps' to the sample (c). Finally, the Z-piezo tube continues to expand, loading the AFM probe and sample surface causing the cantilever to bend and deflect the laser upward (d). The dashed black line in (a) is a linear fit to the (d) region and represents the deflection sensitivity.

3.3. Sample Requirements

In order to obtain quality results in the PFM measurement, it must be first ensured that the sample being measured is properly prepared. Firstly, the material of interest must be placed on a conductive substrate. The purpose of this is to ensure that the drive voltage entered into the software and thus applied between the conductive stage and conductive

AFM tip is actually being applied only across the material of interest. This setup will create the electric field within the sample which will then cause a mechanical response if that sample is electromechanically active. When attaching / depositing the material of interest on the conductive substrate, it is also important that the substrate is cleaned. A typical cleaning process is a sonicated acetone bath, IPA bath, and DI water bath followed by an O_2 plasma clean to remove any organics on the conductor's surface. The cleaning becomes increasingly important as thinner materials are being used, such as 2D materials. If there is an appreciable residue layer, that thickness may be of the same order as a monolayer of a 2D material and cause significant contributions to the measured signal.

It is good practice to then secure the sample on a conductive and magnetic AFM disk with silver paste, being sure that a conductive path is created from the conductive substrate to the AFM disk. The AFM disk serves as a robust handle to manipulate the sample without risking damage from tweezers and provides secure and stable mounting of the sample onto the stage. The mounting is done using a magnetic sample holder which anchors the AFM disk and thus the sample.

More generally, the material of interest for a PFM measurement should be either insulating or semiconducting. Conductive materials are not electromechanically active due to the fundamental fact that they contain free carriers which screen out any potential electric field that would enter the sample. Insulators and semiconductors on the other hand will not be able to screen out the electric field, allowing for the field to interact with the sample's constituent atoms.

3.4. AFM PROBE PARTICULARS

After preparing the sample, the selection of the AFM probe is the most important aspect of the PFM setup. There are many tip and cantilever specifications that must be

weighed against each other to determine which type of AFM probe is appropriate for PFM. Such properties include tip radius-of-curvature, cantilever spring constant, resonant frequency, width, length, and the materials used to fabricate and coat the probes. The following should help in the selection of an appropriate AFM probe, as well as justify why the probes used in the measurements were selected.

The first step for AFM probe selection is to understand the requirements of the measurement. PFM is a conductive, contact mode AFM measurement which applies an alternating voltage between the AFM tip and the conductive stage. Thus, the most obvious requirement is that the probe is conductive and relatively wear-resistant. Either the base material of the probe, or a coating over the probe, must be conductive to fulfill this requirement. Additionally, since PFM is a contact mode measurement, the tip should be reasonably hard to resist the wear and tear. Materials that fit these criteria include cobalt-chromium, platinum-iridium, doped-diamond, and platinum-silicide tips. The level of conductivity should also be considered, where the metal-coated tips will be the most conductive.

The next parameter of interest is the radius-of-curvature of the tip. Ideally, the AFM tip would come to an infinitely sharp point at the tip apex, but in reality, the tip more closely resembles a sphere with a certain radius. Different probes types have different tip radii which are mostly material dependent. Of the conductive probes mentioned the metal coated CoCr and PtIr probes have a radius of 25 – 35 nm, the PtSi tips are ~ 15 nm, and the doped-diamond are ~ 100 nm. The importance of radius-of-curvature lies in the fact that this controls the maximum resolution attainable in a given measurement. Tips with a small radius-of-curvature will be able to distinguish smaller features and give more localized measurement compared to large radius-of-curvature tips. Another aspect that is affected is the electric field distribution around the probe tip. Sharper tips will have

stronger electric field concentration and potentially larger electric field gradients which could affect electromechanical measurements. A trade-off arises here because sharper tips tend to not be as wear-resistant.

Another aspect of AFM probes to consider is the resonant frequency of the cantilever, especially the contact resonance. In the PFM measurement, an alternating voltage is applied to the sample through the tip and with an electromechanically active material, the sample will oscillate between expansion and contraction and cause movement of the cantilever. If the oscillations happen at the resonant frequency of the cantilever, the measurable signal will be affected and could be enhanced. More specifically, since the AFM tip will be in contact with the sample, it is the contact resonance frequency which will affect the measurement. The value of the contact resonant frequency will be higher than the resonant frequency quoted on AFM probe specification sheets since those refer to free-space contact resonant frequencies. A frequency sweep of the piezoresponse amplitude channel should be done to determine this frequency. It is possible to uses the resonant phenomena to enhance the PFM signals, but this adds complexity and is avoided in this research.

Two AFM probe specifications related to the resonant frequency are cantilever length and width. These two parameters will affect the resonant frequency of the cantilever, but also play other roles in the measurement. The width of the cantilever can affect how much laser light is reflected into the position sensitive photodiode, and the length will affect the angle at which the laser is reflected for a given displacement of the sample. This issue will be discussed in detail in Chapter 3.9, but the main conclusions is that shorter cantilevers will cause a larger deflection of the laser light for a given sample deflection.

Another AFM probe characteristic related to the cantilever length is the cantilever spring constant. The spring constant, k, is a measure of the stiffness of the cantilever where a small value means the cantilever is softer and easier to deform and a large constant means the cantilever is stiffer. The length and width of the cantilever will also affect this value, where narrower, longer cantilevers tend to be softer and wider, shorter cantilevers tend to be stiffer. When measuring small PFM signals of 2D materials, it may be believed that a soft cantilever would be more sensitive and give a better signal, but the opposite is true. Soft cantilevers tend to give inferior PFM images because their response to deformation is more nonlinear and somewhat uncontrollable[101]. A good rule of thumb is to select cantilevers with k values greater than 1 N m^{-1}.

Taking this information into account, a selection of an AFM probe can be made. The probes used for all PFM measurements done in this work are cobalt-chromium coated, etched silicon probes from Bruker (MESP-RC, or the newer version MESP-RC-V2). These probes have a nominal tip radius of curvature of 35 nm, a free-space resonant frequency of 150 kHz, spring constant of 5 N m^{-1}, and a cantilever length and width of 125 μm and 35 μm, respectively. These specifications tend to yield relatively good quality PFM images.

3.5. Ideal Calculation of d_{33}

From the PFM measurement outputs, a quantitative description of the material's electromechanical response can be made. The quantity being measured is the amount of expansion and contraction caused in the sample material due to the applied voltage. This is a converse piezoelectric effect whose behavior is described by the piezoelectric tensor d_{ij}. This tensor is defined in Table 1.1 and has equivalent units of C N^{-1} and m V^{-1} to describe the direct and converse effects, respectively. The PFM measurement directly

measures the units needed for this coefficient: picometers of displacement per applied drive voltage.

The PFM measurement gives a single number – a scalar – whereas d_{ij} is a tensor with various components defined as

$$d_{ij} = \begin{bmatrix} d_{11} & d_{12} & d_{13} & d_{14} & d_{15} & d_{16} \\ d_{21} & d_{22} & d_{23} & d_{24} & d_{25} & d_{26} \\ d_{31} & d_{32} & d_{33} & d_{34} & d_{35} & d_{36} \end{bmatrix}. \tag{3.1}$$

The *i* subscript describes the direction of polarization, or electric field, and the *j* subscripts describe the relevant component of the strain, or stress, tensor. To properly ascribe the measured value from the PFM measurement to a specific component, the geometry of the problem must be understood. Figure 3.3 shows the general behavior of the electric field distribution and the resultant expansion and contraction direction. For a thin sample material, a majority of the applied electric field will be in the out-of-plane direction, $i = 3$, and a majority of the material's mechanical response will be in the out-of-plane direction, $j = 3$. As a result, the d_{ij} component measured in a PFM experiment in the ideal case is d_{33}.

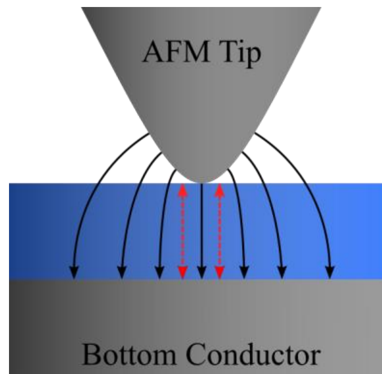

Figure 3.3 The electric field distribution arising as a result of the applied voltage between the AFM tip and the bottom electrode and the resultant direction of the mechanical response of the sample. The black arrows represent the electric field distribution and the dashed red arrows represent the material response.

With the knowledge of what is being measured by the PFM and the appropriate field direction involved, an equation can now be constructed to describe the magnitude of the ideal piezoelectric response of the sample,

$$d_{33} = \frac{V_{PFM} \cdot s_d}{V_d \cdot GAIN}. \tag{3.2}$$

The PFM amplitude, V_{PFM}, is the amplitude channel output of the lock-in amplifier given in mV, s_d is the deflection sensitivity which is calculated as described in section 3.2, V_d is the drive voltage amplitude, and *GAIN* is to compensate for a built-in hardware amplification factor of the amplitude channel which is done to allow detection of the small signals involved (*GAIN* = 16x here).

3.6. PFM Deficiencies and Limitations

3.6.1. Material Clamping

Although PFM is a powerful technique, it has several limitations. This section is dedicated to further discussion of these factors and provides an argument why the measured piezoelectric coefficient should be referred to as an effective value rather than an absolute one.

The first issue that creates concern about the interpretation of the measurement is material clamping[106,107]. As is shown in Figure 3.3, the electric field is rather localized around the AFM tip, so the portion of the sample which will experience the electromechanical coupling is limited. As a result, the electromechanical response of the sample area directly under the AFM tip will be suppressed by the non-reacting portion of the sample adjacent to it. In other words, the sample area responding to the electric field is clamped by the adjacent area. Figure 3.4 (a), reproduced from Jungk, et. al.[106], shows this process where the sample is only locally affected by the electric field. A potential way to eliminate material clamping is to apply a second electrode on top of the sample so the

electric field is distributed in the material more uniformly and over a larger area. An example of this is given in Figure 3.4 (b) also from Jungk, et. al.[106]. This route involves extra processing steps and photolithography when involving the small areas of 2D materials, so it is avoided in this work. The end result of material clamping occurring in a sample is a probable reduction in the measured value of d_{33} from the actual material property value.

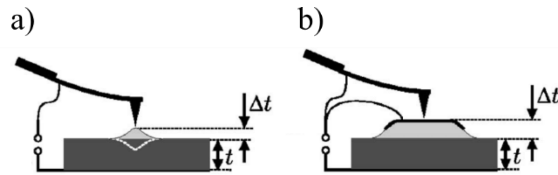

Figure 3.4 Material clamping in the PFM experiment. When only the AFM tip is used as the electrode, only a small area around the tip is affected and responds to the localized electric field (a). The rest of the material which doesn't experience the same electric field clamps the reacting material's ability to respond fully. Depositing an electrode on top of the sample will result in a more uniform and broad distribution of the electric field, reducing the clamping effect (b). Reproduced from Jungk et. al.[106].

3.6.2. Understanding the Forces Involved

In a PFM measurement, there are other factors that can affect how the AFM probe interacts with the sample surface. The multiple contributions to the force that can act on the AFM tip can be summarized by

$$F_{tot} = F_0 + F_{ES} + F_{EM} \tag{3.3}$$

where F_{tot} is the total force, F_0 the elastic force, F_{ES} is the electrostatic force, and F_{EM} is the electromechanical force. The different force components can be further written out as

$$F_0 = kd_0, \tag{3.4}$$

$$F_{ES} = F_{ES}^{Tip} + F_{ES}^{Cant}, \tag{3.5}$$

$$F_{EM} = F_{EM}^{Piezo} + F_{EM}^{Flexo}, \quad (3.6)$$

where k is the spring constant of the AFM cantilever and d_0 is the deflection setpoint, i.e. the amount of deflection the cantilever experiences while in constant contact with the sample. The electrostatic force is split into contributions from the tip, F_{ES}^{Tip}, and the cantilever, F_{ES}^{Cant}, and the electromechanical force is split into components from piezoelectricity, F_{EM}^{Piezo}, and flexoelectricity, F_{EM}^{Flexo}.

The elastic contribution comes from the PFM measurement being a contact-mode AFM technique. The AFM tip is brought into contact with the sample surface and a constant feedback loop attempts to keep the tip and cantilever at a constant level of deflection, d_0. The constant deflection will create a constant elastic force given by Equation (3.4). Because the PFM measurement uses a lock-in amplifier which only amplifies signals at the same frequency as the reference signal, the constant elastic force will have no effect on the PFM signal and can be neglected.

The next possible contribution to the total force comes from electrostatic forces between the AFM probe and the substrate. These forces can come from the AFM tip or the AFM cantilever, as described by Equation (3.5). Contributions from the cantilever would act as parallel-plate capacitor-like interactions from the rectangular beam cantilever to the substrate. The dimensions of the cantilever used here are 125 μm x 35 μm, so any electrostatic interactions from the cantilever would be averaged over this entire area. A method to rule out this type of contribution to the PFM measurement is if the measured feature has finer resolution than the size of the cantilever. Figure 3.5 illustrates this point with an AFM probe over a sample with interspersed areas of electromechanically active material on conductive gold. If the electrostatic contributions from the cantilever are significant, the PFM measurement would be averaged over the entirety of the cantilever

size. Being able to distinguish each individual sample area would rule out electrostatic contributions from the cantilever.

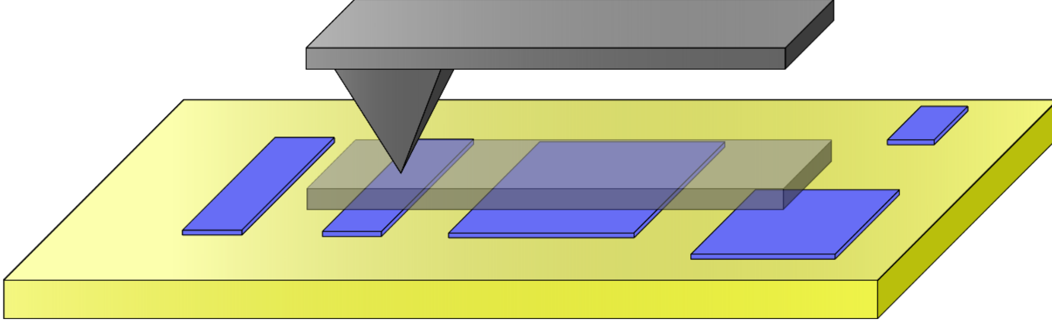

Figure 3.5 AFM probe in-contact with a PFM sample. The blue areas represent electromechanically active materials on a gold substrate. The opaque grey rectangular box represents the area on the sample which is directly below the AFM cantilever. If there were electrostatic contributions to the force between the cantilever and the sample, the signal measured at the AFM tip point would be an average over the entire opaque box area. If the individual sample areas are distinguishable, then electrostatic forces from the cantilever are negligible.

Similarly, electrostatic forces from the AFM tip can contribute to the total force. This force can be written as[108]

$$F_{ES}^{Tip} = -\frac{1}{2}\frac{dC_{Tip}}{dz}\left(V_{DC} + V_{AC}\sin(\omega t) + \frac{\Delta\varphi}{q}\right)^2, \tag{3.7}$$

where V_{DC}, V_{AC}, ω, t, $\Delta\varphi$, and q are the applied DC voltage, applied AC voltage amplitude, frequency, time, work function difference between the tip and area under the tip, and charge of an electron, respectively. Because the PFM experiment uses a lock-in amplifier to measure tip deflection, it is sufficient to consider only the first harmonic of Equation (3.7), yielding

$$F_{ES,1\omega}^{Tip} \propto \left(V_{DC} + \frac{\Delta\varphi}{q}\right)V_{AC}. \tag{3.8}$$

This relation provides multiple insights for detecting electrostatic contributions to the PR signal. To determine if electrostatic forces are significant, a DC bias sweep can be performed while measuring the amplitude channel signal. A linear absolute-value dependence on V_{DC} with a minimum at $V_{DC}=\Delta\varphi/q$ is expected if electrostatic forces are playing a role. If the DC bias sweep measurement and the amplitude channel response is independent of V_{DC}, then the electrostatic interaction between the tip and the sample are negligible and can be ignored. Otherwise, V_{DC} can be set equal to $\Delta\varphi/q$ to minimize the electrostatic contribution during the PFM measurement.

With the elimination of the first two terms in Equation (3.3), the PFM signal must be coming from electromechanical effects. The main two sources of potential signal are summarized in Equation (3.6) and are either piezoelectric or flexoelectric. Typical PFM studies neglect flexoelectric responses to the signal and claim that the entirety of the forces acting on the AFM tip and cantilever are due to piezoelectric forces. In a piezoelectrically active material, flexoelectric effects are most-likely small compared to the piezoelectric effects, but should not be neglected in weakly-piezoelectric or non-piezoelectric materials. Specific contributions from flexoelectricity and piezoelectricity are material and system dependent and will be discussed in further detail in Chapter 4. Nevertheless, this fact brings about the idea that the measured signal may not be purely piezoelectric in origin, leading to the next section.

3.6.3. The Effective Nature of the Measured d_{33}

The measured result from the PFM measurement, d_{33}, could include contributions from, or may be affected by, phenomena which are not piezoelectric in nature. A few of these contributions have been discussed in this section, and as a result, the measured value from the PFM experiment should be referred to as an effective piezoelectric coefficient,

d_{33}^{eff}. Due to difficulty in isolating the proper source of the measured signal, it would not be appropriate to definitively claim that only the d_{33} coefficient is being measured. Other components of the piezoelectric tensor, depending on the specific material, may also be contributing in a non-negligible fashion to the final measured result. Material clamping can also affect the measured signal noticeably by decreasing the magnitude of the material's electromechanical response.

More importantly to the research being done in this work, it is difficult to distinguish piezoelectric and flexoelectric responses at the nanoscale. In the following chapter, the sample material will be the 2D material molybdenum disulfide (MoS_2) which has a thickness of only 6.5 Å. On the length scale of the order of individual atoms, the classic interpretation of a voltage being applied across two metal contacts creating a uniform electric field may break down. Also, electric field gradients are present laterally since the electric field will get weaker with increased distance from the AFM tip. Electric field gradients are the fundamental cause of converse flexoelectricity, which can exist in every crystal structure, unlike piezoelectricity. The unavoidable inhomogeneity of the electric field emanating from the AFM tip and the nanoscale nature of the sample make it improper to report the quantitative value measured by a PFM measurement to be d_{33}. Instead, referring to it as d_{33}^{eff} allows for it to be a catch-all of various possible electromechanical responses even though the d_{ij} tensor purely describes piezoelectricity.

3.7. BACKGROUND VECTOR SUBTRACTION

3.7.1. The Inherent Background Signal

PFM measurements have an unavoidable contribution from an inherent background signal[101,106,109,110]. The signal seems to be system-specific and results from a combinations the AFM feedback electronics, mechanical resonances of the AFM probe, and extreme

sensitivity of the measurement that may be detecting thermal noise[101]. The baseline magnitude of the background signal is on the order of 2 mV as measured in the position sensitive photodiode, but dependence on drive frequency has been observed.

This level of background signal becomes troublesome as it is roughly the same order-of-magnitude of the expected responses of 2D materials and weaker piezoelectric materials (1 – 10 pm V^{-1}). To obtain a reliable quantitative estimate of the material response, removing the background contributions become imperative. A background vector substation technique has been adopted from literature[109] and specialized to accommodate the measurement of 2D materials with weak responses.

3.7.2. Unwanted Frequency Dependence

Theoretically, the electromechanical response of a material should not be frequency dependent in the kHz regime[109] and thus the PFM measurement should not depend on the drive frequency as long as it is away from the contact-resonant frequency. In experiments, this is not the case. A dependence on the frequency can be seen in both the amplitude and phase channels. A similar frequency dependence can even be seen when the drive voltage is not applied to the sample, indicating that at certain frequencies the PFM signal response can be dominated by some type of system-inherent mechanical behavior of the AFM cantilever.

This type of behavior occurs during both stationary, point measurements and measurements while scanning the surface. The frequency dependence observed during the PFM scanning gives rise to another possible errant cause of the PFM signal. The feedback electronics in the system which keep the AFM cantilever at a certain deflection level may be moving the probe with the sample topography at a frequency equal to that of the drive voltage. PFM signal obtained from a result such as this would not be due to the

electromechanical properties of the materials, but instead are the result of tip-scanning artifacts created by the topography of the sample surface. To test for, and rule out, this type of artifact, two successive PFM measurement scans are performed immediately after one another. In the first scan, the drive voltage is applied to the sample and in the second scan, the drive voltage is not applied. If there is only signal arising from the image with the drive voltage applied – seen as image contrast between the electromechanical active sample area and the non-electromechanically active substrate – then the signal is not affected by scanning artifacts. However, if there is contrast in the PFM images even when the drive voltage is not applied to the sample, the source of the signal is likely caused by scanning artifacts and not electromechanical action of the sample. The experiment must then be repeated at a different drive frequency. Therefore, when performing experiments to test for electromechanical activity of a sample, two measurement scans are required to rule out scanning artifacts. The second measurement can also be considered a control measurement to get a baseline measurement of the inherent background signal at the frequency being used and will be referred to the 'voltage-off' condition in the following sections.

In order to select the appropriate frequency to use for the PFM measurement, the frequency response of the system should be measured by performing a frequency sweep of the amplitude channel at a single point. An example of this is shown in Figure 3.6. This is a generally representative frequency response of the PFM used for these experiments when the drive voltage is applied. Again, electromechanical responses of the samples should be independent of the drive frequency which is clearly not the case in Figure 3.6. There exists a very complex frequency response from 15 kHz – 50 kHz, most-likely caused by the internal electronics of the PFM system. This frequency range should be avoided when selecting a drive frequency for quantitative PFM analysis. Instead, frequencies

where the amplitude is minimal and non-varying should be selected. The frequency range of ~ 52 kHz – 65 kHz meets this criteria in Figure 3.6, and, unless otherwise specified, all PFM measurements reported in this work will have a drive frequency of 60 kHz.

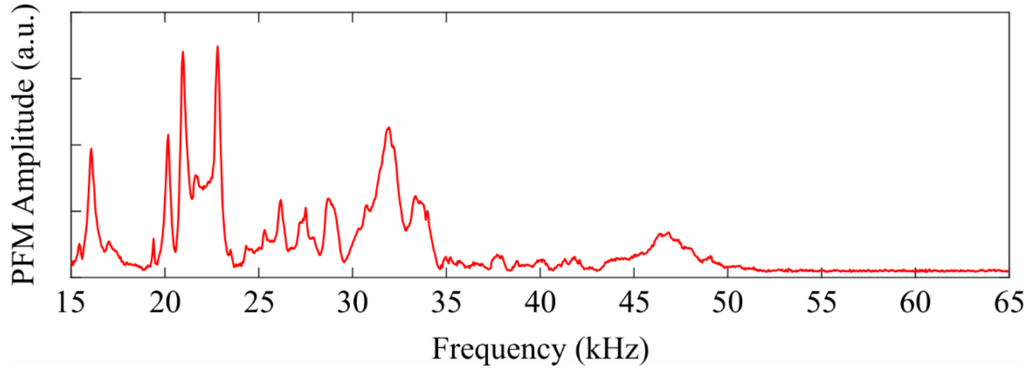

Figure 3.6 The frequency response of the PFM amplitude while sweeping the drive frequency from 15 kHz – 65 kHz. There is a very complex response below 50 kHz, so this range of drive frequencies should be avoided. Instead 60 kHz is used as the drive frequency in this work because it is in a range that is relatively frequency independent.

3.7.3. Removing the Background Signal

With a better understanding of the background signal, a process can now be developed to remove its contribution to the PFM measurement. Building on inspiration from literature[101,109], a vector background subtraction method is developed which utilizes both the amplitude and phase channels. The result of this process is to replace V_{PFM} in Equation (3.2) with a value which has the background contribution removed and only contains the signal originating from the electromechanical response of the sample.

The process begins by obtaining a PFM scan of the material of interest with V_d applied and at a frequency chosen using a frequency sweep (see section 3.7.2). The process also works best if in the PFM image, both the sample material and the conducting substrate are visible within the scan window. Measuring both the sample and the substrate within the same PFM image will give all the necessary data to perform the background subtraction

without the risk of changing parameters or wearing of the AFM tip between successive measurements. It is especially important that the tip geometry is consistent between PFM measurements since tip wear is readily observed and could change the distribution of the electric field being applied to the sample. The conductive substrate is appropriate as a measure of the inherent background signal because conductors cannot be electromechanical active, so measuring it will give an estimate of the proportion of the signal which is originating from sources other than the electromechanical coupling.

The single PFM image will give PFM amplitude and phase data for both the sample, V_{PFM}^{Sam} and θ_{PFM}^{Sam}, and the substrate, V_{PFM}^{Sub} and θ_{PFM}^{Sub}. The values are calculated by averaging over the area covered by the sample and substrate in both the PFM amplitude and phase channels. Next, a second PFM measurement is taken immediately after the first, in the same location with all the same parameters, except that the drive voltage is not applied to the sample. Importantly, the drive voltage is still fed into the lock-in amplifier as a reference signal so tip movement at that frequency can be observed without the application of the drive voltage to the sample. This is the same as the voltage-off control condition described previously. As long as there is no contrast between the sample area and the substrate area, the background subtraction process can proceed, otherwise, a different drive frequency is required. With the appropriate voltage-off condition measurement, an average of the PFM amplitude, $V_{PFM}^{V_{off}}$, and PFM phase, $\theta_{PFM}^{V_{off}}$, can be calculated by averaging over an area of the image.

Now that these six values have been obtained, two separate background subtraction methods can be performed. Since both an amplitude and a phase value are obtained for each measurement type, the PFM measurements for the sample, substrate, and voltage-off condition can all be conceptualized as vectors. This is illustrated in Figure 3.7, where the sample and substrate vectors are plotted. Now, by subtracting the substrate vector from

the sample vector, a background-subtracted vector can be created whose amplitude is given by V_{PFM}^{BS} and phase is given by θ_{PFM}^{BS}. This new vector, show in blue in Figure 3.7, represents the signal purely from the sample with the background contribution removed. V_{PFM}^{BS} can now be plugged into Equation (3.2) for V_{PFM} to calculate the effective piezoelectric coefficient of the sample d_{33}^{eff}.

The process just described compares two of the three measured vectors and can be thought of as the sample response with the removal of any background signal caused by the electric field interacting with the substrate. A separate, complementary, background-subtraction can be done by using the voltage-off condition vector as the background vector instead of the substrate vector. This version of the background-subtracted vector will have a slightly different interpretation and will represent the signal originating from the sample with any contribution from the internal electronics removed. Ideally, the two different background-subtracted vector types should be equal to each other because measuring a non-electromechanically active material should be the same as not applying a drive voltage; there should be no response. If these two background-subtracted vectors are far off from each other, this suggests that there is some contribution to the PFM signal arising from the conducive substrate. This could be from contaminations on the surface, non-perfectly conducting substrates, or stray electrostatic forces.

The background-subtraction method done here has served two purposes. The first, and more obvious, is to give a more accurate representation of the sample's electromechanical response to an applied electric field. The second, and subtler, purpose is to give a logical check that the signals being measured are originating from an electromechanical source.

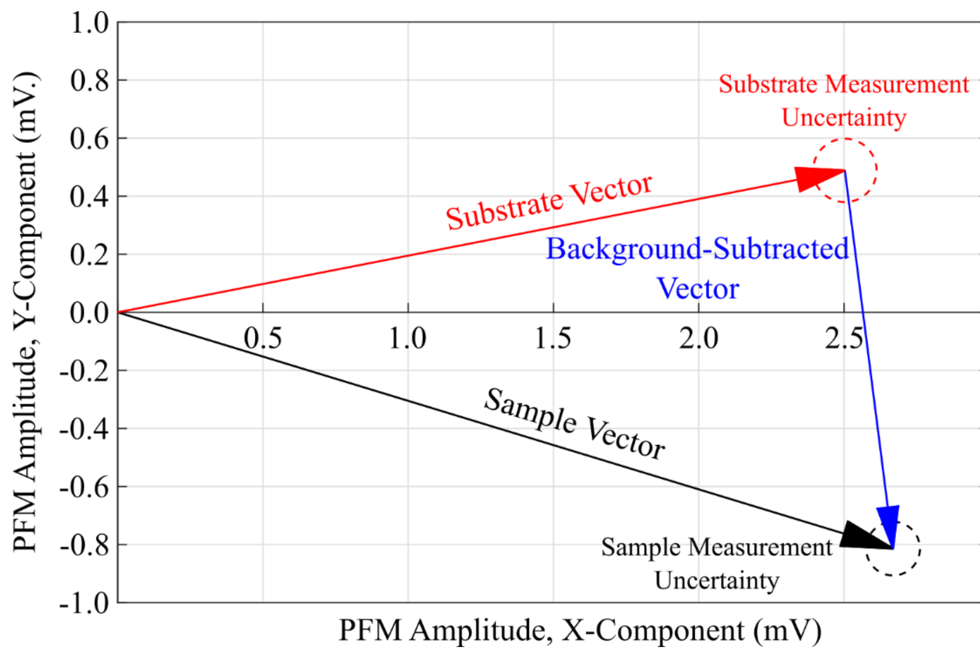

Figure 3.7 A depiction of the vector background subtraction method. First, a PFM image is obtained on a sample capturing the amplitude and phase channel on both the sample and substrate. Next, vectors are created from the amplitude and phase data and are subsequently subtracted from each other. The result, shown in blue here, is a background-subtracted vector that can be used for d_{33}^{eff} calculations. The uncertainty of each measured vector is depicted as a circle at the end of each vector, of which the vector could point to anywhere within.

3.8. Uncertainty Estimation

Any experimental measurement has an experimental uncertainty, or error, associated with it. In the current PFM measurement, an estimate of the level of uncertainty is needed to give a measure of how confidently the quantitative calculations can be claimed. The figure of merit in the PFM experiment is the effective piezoelectric constant, d_{33}^{eff}. The goal is then to determine how any uncertainties arising from every part of the experiment will affect the total uncertainty of d_{33}^{eff}.

The method used to calculate the total uncertainty in d_{33}^{eff} is to use error propagation of the measured values. The first step to accomplish this is to create an

equation which incorporates all the variables containing uncertainty. In this case, the equation for the effective piezoelectric coefficient is

$$d_{33}^{eff} = \frac{s_d}{V_d \cdot g} |V_{PFM}^{BS}|, \tag{3.9}$$

where $|V_{PFM}^{BS}|$ is the amplitude, in mV, of the background subtracted vector. This value should already be positive, but the absolute value sign is to emphasis that fact. $|V_{PFM}^{BS}|$ can then be expanded in terms of the measured values as

$$|V_{PFM}^{BS}| = \sqrt{|V_{PFM}^{Sam}|^2 + \left|V_{PFM}^{Sub}\right|^2 - 2|V_{PFM}^{Sam}|\left|V_{PFM}^{Sub}\right| \cos\left(\theta_{PFM}^{Sam}, -\theta_{PFM}^{Sub}, \right)}, \tag{3.10}$$

where $|V_{PFM}^{Sam}|$, θ_{PFM}^{Sam}, $\left|V_{PFM}^{Sub}\right|$, and θ_{PFM}^{Sub} are the amplitude and phase of the vector measured on the sample and the substrate, respectively. This specific equation is for calculating the background-subtracted amplitude using the sample and substrate vectors. A similar equation can be constructed for the case of using the sample and voltage-off condition vectors by switching out the appropriate values.

The uncertainty of $|V_{PFM}^{BS}|$ can then be obtained by using the formula

$$\sigma_V^{BS} = \sqrt{\left(\frac{\partial|V_{PFM}^{BS}|}{\partial|V_{PFM}^{Sam}|}\right)^2 (\sigma_V^{Sam})^2 + \left(\frac{\partial|V_{PFM}^{BS}|}{\partial|V_{PFM}^{Sub}|}\right)^2 \left(\sigma_V^{Sub}\right)^2 + \left(\frac{\partial|V_{PFM}^{BS}|}{\partial\theta_{PFM}^{Sam}}\right)^2 \left(\sigma_\theta^{Sam}\right)^2 + \left(\frac{\partial|V_{PFM}^{BS}|}{\partial\theta_{PFM}^{Sub}}\right)^2 \left(\sigma_\theta^{Sub}\right)^2}, \tag{3.11}$$

where σ_V^{Sam}, σ_V^{Sub}, σ_θ^{Sam}, σ_θ^{Sub}, are the uncertainties associated with the amplitude of the sample and substrate, and the uncertainties associated with the phase of the sample and substrate, respectively. The mean values for the amplitude and phase measurements are obtained by performing a Gaussian fit over the data points at the respective sample and substrate locations in the PFM image. The associated uncertainties are taken to be the 95% confidence interval of the fitted mean values. All calculations are done using custom written MATLAB code.

Next, the error must be propagated through Equation (3.9). This can be done by using the equation

$$\sigma_{d33} = d_{33}^{eff}\sqrt{\left(\frac{\sigma_{sd}}{s_d}\right)^2 + \left(\frac{\sigma_{Vd}}{V_d}\right)^2 + \left(\frac{\sigma_V^{BS}}{|V_{PFM}^{BS}|}\right)^2}, \tag{3.12}$$

where σ_{d33} σ_{sd}, and σ_{Vd}, are the uncertainties associated with d_{33}^{eff}, s_d, and V_d, respectively.

This value represents the uncertainty in the fitting of the mean value of the measurements. To incorporate any uncertainty originating from the substrate, a new value is introduced: σ_{sub}. This value is calculated using Equation (3.9), but here $|V_{PFM}^{BS}|$ is calculated using vector subtraction of the substrate and the voltage-off condition vectors. In other words, $|V_{PFM}^{Sam}|$ and θ_{PFM}^{Sam} in Equation (3.10) are replaced with $\left|V_{PFM}^{Voff}\right|$ and θ_{PFM}^{Voff}. The result can be written as

$$\sigma_{sub} = \frac{s_d}{V_d \cdot g}\sqrt{\left|V_{PFM}^{Voff}\right|^2 + \left|V_{PFM}^{Sub}\right|^2 - 2\left|V_{PFM}^{Voff}\right|\left|V_{PFM}^{Sub}\right|\cos\left(\theta_{PFM}^{Voff}, -\theta_{PFM}^{Sub},\right)}, \tag{3.13}$$

and is a quantitative representation of the contribution to measured d_{33}^{eff} from the substrate. This value should ideally be zero or very small since the conductive substrate should not have any electromechanical response and thus can also be used as a measure of error the experiment.

Finally, the total uncertainty of d_{33}^{eff} can be calculated as the sum of squares of Equation (3.12) and Equation (3.13):

$$\sigma_{tot} = \sqrt{\sigma_{d33}{}^2 + \sigma_{sub}{}^2}. \tag{3.14}$$

3.9. Maximizing PFM Contrast

The calculation of d_{33}^{eff} relies on the PFM contrast between the sample area and the substrate area in both the amplitude and phase channels. This means it is important maximize the contrast level within a measurement by increasing the sensitivity of the

experiment. This section is dedicated to some of the finer details that will allow for more robust detection of PFM signals and what is revealed from deeper analysis of the involved equations.

First, consider the effect the length of the AFM cantilever has on the sensitivity of the system. The sample deflection from the applied electric field is detected via bending of the cantilever while the tip is in contact with the sample. The bending is then detected via the reflection of a laser off the back side of the cantilever. If the angle the laser is reflected off the cantilever can be enhanced for a given vertical deflection of the sample, the system will be able to measure the deflections with a higher resolution. The length of the cantilever has this exact effect on the deflection angle of the laser. Figure 3.8 shows how a shorter cantilever bends to a larger degree for the same amount of vertical deflection. When the two cantilevers start at the same angle of incidence, an equal vertical displacement will always result in $\theta_1 > \theta_2$, which will then create a larger deflection of the laser into the position sensitive photodiode. If the cantilever length does not drastically affect other properties, shorter cantilevers are preferred for better measurements. One other parameter that can be affected by cantilever length is the cantilever spring constant, where longer cantilevers tend to have lower spring constant. If spring constants are too low, cantilever bending can be non-linear, and if spring constants are too high they may be too stiff to measure material deflection. Spring constants on the order of ~ 1 N m^{-1} tend to give good results.

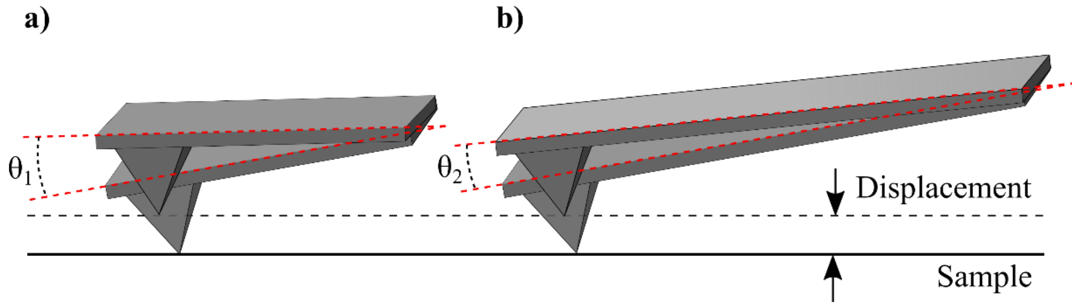

Figure 3.8 The length of the cantilever will affect the bending angle for a given vertical deflection. A shorter cantilever (a) will have a larger bending angle than a larger cantilever (b). This results in better sample displacement resolution for shorter cantilevers.

Related to the angle of laser deflection, a more thorough understanding of the deflection sensitivity, s_d, can give insights into the measurement operation. Given in the units of nm V^{-1}, it is more easily understood by describing its inverse as the voltage change measured in the position sensitive photodiode per vertical distance of deflected in the sample. In other words, it measures the amount of laser deflection per vertical sample movement. So, for better sensitivity, a larger laser deflection is desired for the same amount of vertical sample movement. This translates to a smaller value of s_d giving better sensitivity within a PFM image and is shown mathematically as

$$\leftrightarrow d_{33}^{eff} = \frac{\uparrow V_{PFM} \cdot \downarrow s_d}{\uparrow V_d \cdot GAIN}. \tag{3.15}$$

The two sides of this of Equation (3.15) must remain constant because a material's intrinsic effective piezoelectric constant does not depend on any of the RHS terms. The term in the RHS which is measured during the experiment and used for the d_{33}^{eff} calculation is the value of the amplitude channel, V_{PFM}. A larger measurable value of V_{PFM} will allow for less uncertainty and means that there is a larger amount of contrast seen between the sample and background measurements. To allow for a larger measurable value of V_{PFM} without the need for any equipment improvements or signal enhancements, simply

decreasing the value of s_d will suffice as indicated by the arrows in Equation (3.15). This can be done by maximizing the deflected angle of the laser by decreasing the cantilever length and by aligning the laser spot as close to the edge of the cantilever as possible. Also, increasing the drive voltage, V_d, will increase the measured value of V_{PFM} linearly, but should be done with caution as high voltages may damage the sample.

3.10. Conclusions and Significance

Piezoresponse force microscopy is a powerful tool for characterizing material properties and determining electromechanical behaviors. A very localized electric field is applied to a sample and the resultant material deflection is measured. It is a complex process which makes fully understanding the measurement results difficult. Internal electronics of the PFM system, varying electric field distributions, and signal contributions from unwanted sources further complicate the measurement. However, by performing the vector background subtraction, a more quantitatively accurate representation of the sample's properties is obtainable.

Before the following chapter, one point should be emphasized. Equations (3.3) to (3.6) describe the forces involved in creating a PFM image, where the major contributing forces are from the electromechanical forces in Equation (3.6). Since both the piezoelectric and flexoelectric forces arise from electric fields, which are difficult to fully determine, it is difficult in general to isolate piezoelectricity from flexoelectricity. Most measurement rely on the fact that piezoelectricity has a stronger response than flexoelectricity, which is usually an appropriate assumption. When looking at nanoscale features, this may no longer be the case because spatial gradients will be larger without creating massive strains or electric fields that would damage the material. 2D materials fit inside this category but also have interesting symmetries that allow for tricks to further isolate one effect from

another. The next chapter deals with using a PFM to measure the electromechanical response of the 2D material MoS_2 and how to properly understand the response.

Chapter 4:

Out-of-Plane Electromechanical Response of Monolayer MoS_2 [iv]

The in-plane piezoelectric response of MoS_2 has been theoretically predicted and experimentally demonstrated to exist in monolayer and few-odd layered flakes. In this chapter, the electromechanical response of monolayer MoS_2 is probed for the first time in the out-of-plane direction. The detection of such as response is an indicator that the flexoelectric effect is present and measurable in single-layered MoS_2. Using the PFM techniques developed in the previous chapter, such an out-of-plane electromechanical response is detected in MoS_2 for the first time, implicating flexoelectricity as its possible source.

[iv] Brennan, C. J.; Ghosh, R.; Koul, K.; Banerjee, S. K.; Lu, N.; Yu, E. T. Out-of-Plane Electromechanical Response of Monolayer Molybdenum Disulfide Measured by Piezoresponse Force Microscopy. Nano Lett. 2017, 17 (9), 5464–5471.
Author Contributions: C.J.B. performed the sample fabrication, AFM, PFM, Raman, photoluminescence, and data analysis. R.G. and S.B. provided CVD grown MoS_2 and assisted in the transfer process. K.K. assisted in AFM measurements. N.L. and E.T.Y. assisted in project design and supervised research. C.J.B., N.L., and E.T.Y. wrote the paper.

4.1. INTRODUCTION

The coupling of electronic and mechanical behaviors in crystalline materials has created many engineering opportunities. Strain is commonly used in electronics to alter electronic bandgaps and carrier mobilities[111], and electromechanical coupling is widely used in microelectromechanical systems (MEMS) to make sensors[25], actuators[112], and generators[113]. One of the most widely used electromechanical coupling phenomena is piezoelectricity, which links crystal polarization and mechanical strain. Piezoelectricity only exists in non-centrosymmetric crystalline materials, limiting the range of possible materials for use for such applications. As scaling trends continue to shrink the feature size of materials, a need arises for nanoscale piezoelectric materials. Two-dimensional (2D) materials are very popular candidates for nano-devices because of their exotic electronic properties[19], transparency[20,114], and mechanical robustness[63], and have recently be shown to be candidates for electromechanical nano-transducers[44,46].

In the atomically thin limit, transition metal dichalcogenides (TMDs) are intrinsically piezoelectric due to the lack of inversion symmetry in their crystal structure[16]. Piezoelectricity arises within the plane of their atoms and both direct[44,47] and converse[45,47] piezoelectric effects have been experimentally confirmed in monolayer and few layer molybdenum disulfide (MoS_2). In-plane piezoelectricity should only exist in odd-number layers of TMDs where there is no inversion symmetry present, and decrease rapidly as the number of layers increases due to cancellation of the responses from oppositely oriented layers[44]. Any strain or electric field applied perpendicular to the surface of the MoS_2 will theoretically yield zero piezoelectric response due to its crystal symmetry.

Piezoelectricity is, however, only one type of electromechanical response possible in crystal lattices. In flexoelectricity, polarization arises from strain gradients as opposed to uniform strain[10–12]. Thus, a fourth-order tensor describes flexoelectricity, while a third-

order tensor describes piezoelectricity. With an even-rank tensor, flexoelectricity is present in every crystal class. Despite this, flexoelectricity has been seldom studied because the strain gradients necessary to cause a noticeable change in polarization in macro-scale materials requires very large strains that can fracture the material. However, in nanoscale materials, even small strain can cause large gradients to form.

Investigations of flexoelectricity in 2D materials[12,38,115] have mainly focused on either carbon systems[31,49,50] or hexagonal boron nitride[52,53]. These works were performed from the modeling side, but since 2D materials are the ultimate nanoscale material and can have large strain gradients, they can offer a platform for experimental studies of flexoelectricity.

Another reason for the lack of experimental study of flexoelectricity is because piezoelectricity and flexoelectricity are difficult to isolate from each other. The proposed solution here is to utilize the symmetry of MoS_2 and other TMDs. Their crystal class, D_{3h} ($\bar{6}m2$), results in a flexoelectric tensor which has nonzero coefficients in the out-of-plane direction[116], whereas all out-of-plane piezoelectric coefficients are zero[16]. Flexoelectricity in 2D materials can therefore be studied experimentally if an out-of-plane electromechanical response in MoS_2 is measurable. There have been a few notable experimental studies investigating out-of-plane electromechanical properties of 2D materials, namely on graphene-nitride nanosheets with non-symmetric holes[55] and graphene forming bonds to the underlying SiO_2 substrate[105]. Neither study suggested an estimate for a flexoelectric coefficient. Interestingly, since 2D materials are essentially only a surface, it becomes ambiguous whether out-of-plane electromechanical effects caused by spatial gradients should be referred to as flexoelectricity or surface piezoelectricity[10,11]. Nevertheless, it is referred to as a flexoelectric response here.

In this chapter, PFM is used to probe for the existence of out-of-plane electromechanical coupling in MoS_2. If it exists, it would be a sign that the flexoelectric effect is present in 2D materials. The chapter is organized to first describe the sample fabrication process. Two samples are created here, CVD-grown MoS_2 transferred onto gold-coated silicon and CVD-grown MoS_2 transferred onto Al_2O_3 on n^{++} silicon. Next, characterization of the MoS_2 on both samples is performed with an in-depth analysis to confirm the presence of monolayer MoS_2. PFM measurements are then done to characterize the out-of-plane electromechanical response of MoS_2 followed by a detailed discussion of the origins of the detected signal and the possibilities of the measured signal being a flexoelectric effect. Finally, the possibilities of the signal originating from contamination is discussed and then the work is summarized with the practical significance of the work expressed.

4.2. EXPERIMENTAL METHODS

4.2.1. MoS_2 CVD Growth Overview

The MoS_2 used in this portion of the work has been grown via CVD using solid precursors by collaborators in Dr. Sanjay K. Banerjee's research group at the University of Texas at Austin. CVD-grown MoS_2 is desirable in this case because it yields a large amount of monolayer and few-layer MoS_2 and is more repeatable than using the exfoliation method. With a higher coverage area of monolayer MoS_2 on the sample, much less time is needed to find monolayer areas using CVD-grown MoS_2, resulting in more time dedicated to the electromechanical measurements and analysis.

The details of their growth process and material characterizations can be found in the literature[117], but the basic process flow will be discussed here. The growth substrate is a 285 nm thick SiO_2 layer on Si and the reactant materials are MoO_3 and sulfur power

placed in alumina crucibles. The standard vapor transfer growth process occurs inside a quartz tube which is elevated to 850 ˚C after the chamber is evacuated to a base pressure of 10 mTorr and returned to atmospheric pressure by flowing N_2 gas. The growth process occurs for 5 minutes at 850 ˚C, and the sample is then cooled down. The film quality can then be analyzed using Raman spectroscopy, photoluminescence, optical microscopy, and AFM for film thickness.

4.2.2. Transfer of CVD-Grown MoS_2

A good quality CVD-grown MoS_2 film is the starting point for creating the sample needed for out-of-plane electromechanical measurements using PFM. The next step involves transferring the as-grown MoS_2 onto a conductive substrate. 2D material transfer between a growth substrate or a bulk crystal to a receiving substrate is of great importance to the field of 2D material research. The film must remain intact and high quality throughout the process to prevent mechanical fracturing and degradation of electrical performance. Luckily, the requirements of this project are relaxed compared to other studies which look at in-plane electrical properties. Here, out-of-plane properties are of interests, so the size of the flake is less important and thus stresses from bending that could cause cracking are less significant to the process. Secondly, it is important to get a background PFM measurement of the conducting substrate for the background vector subtract mentioned in the previous chapter, meaning that areas of interspersed monolayer MoS_2 and exposed substrate are preferred. Figure 4.1 illustrates the transfer process.

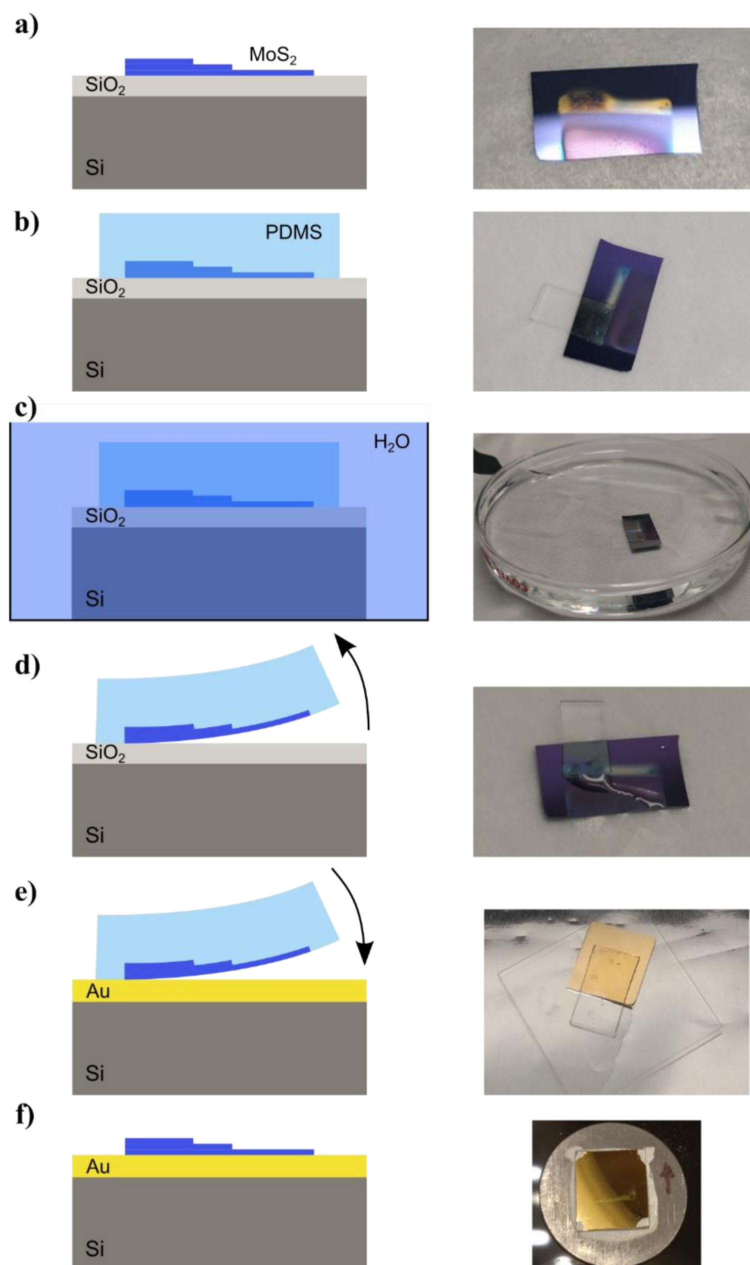

Figure 4.1 The schematic steps in the transfer process are shown with associated pictures of the sample at each step. The process is as follows: (a) MoS_2 is grown on SiO_2 via CVD; (b) a PDMS stamp is pressed on the MoS_2; (c) the sample is submerged in water; (d) the sample is removed from water, dried, and the PDMS is peeled off with some MoS_2; (e) the MoS_2 on PDMS is placed on the receiving substrate (gold shown here) and heated on a hot plate to 50 - 70 °C; (f) and finally the PDMS stamp is slowly peeled away, leaving the MoS_2 on the receiving gold substrate.

First, a small piece of 10:1 PDMS is placed directly over the MoS_2 area of interest. A small amount of pressure is used to ensure there is good contact between the PDMS and MoS_2 with no air bubbles. The entire sample, with the PDMS attached, is then submerged in DI water for roughly five minutes. The water causes the MoS_2 to separate from the SiO_2 yet remain attached to the PDMS. The difference in the hydrophobicity between MoS_2 and SiO_2 is believed to cause the separation. The sample is then removed from the DI water and excess water is removed with a rolled-up lab-wipe. After airdrying for a few minutes, the PDMS is removed from the growth substrate in a quick motion to help facilitate MoS_2 transfer. As described in section 2.2.2., PDMS is viscoelastic with fast peeling promoting MoS_2 adhesion to PDMS. The PDMS is also very soft and bendable so picking up the sample could impart stresses onto the MoS_2 flake from PDMS bending. Cracking from these stresses does not dramatically degrade the sample yield, but nevertheless, a glass backer is used to give the MoS_2/PDMS sample rigidity during its handling.

The MoS_2 is then transferred onto the receiving substrate from the PDMS stamp. Gold is primarily used in this project as the receiving substrate, but this process works with most other materials, emphasized by the fact that gold typically has poor adhesion compared to other materials. The MoS_2/PDMS/glass is placed MoS_2-side-down on the receiving substrate and placed on a hot plate set in the range 50 - 70 °C. After roughly five minutes, the PDMS/glass is slowly peeled away from the receiving substrate. The slow removal helps to separate the MoS_2 from the PDMS. A second sample, not shown in Figure 4.1, is also created by performing the sample procedure but transfer the MoS_2 onto Al_2O_3.

Interestingly, the relaxation of strain can be measured during the transfer process. During the MoS_2 growth[117], the furnace reaches temperatures of up to 850 °C. The MoS_2 growth on SiO2 occurs at this elevated temperature and is originally unstressed. As the sample cools to room temperature, differences in the thermal expansion coefficient of the

MoS_2 and SiO_2 cause the thin MoS_2 film to contract with the relatively thick SiO_2 instead of at the natural rate for MoS_2, resulting in strained MoS_2. The evolution of strain during the entire transfer process can be observed via PL measurements and Raman spectroscopy. The A-exciton peak will shift in energy with applied strain, and this shift is observable in the PL measurement[118]. Figure 4.2 shows PL measurements of the MoS_2 on the growth substrate, on the PDMS stamp, and on the final gold substrate. Figure 4.2 (g) directly compares the PL measurement of monolayer MoS_2 on all three substrates and clearly shows the peak location when on SiO_2 is shifted compared to the other substrates. The process of removing the MoS_2 from the SiO_2 growth substrate relaxes the film, which continues to be relaxed during the remainder of the transfer process.

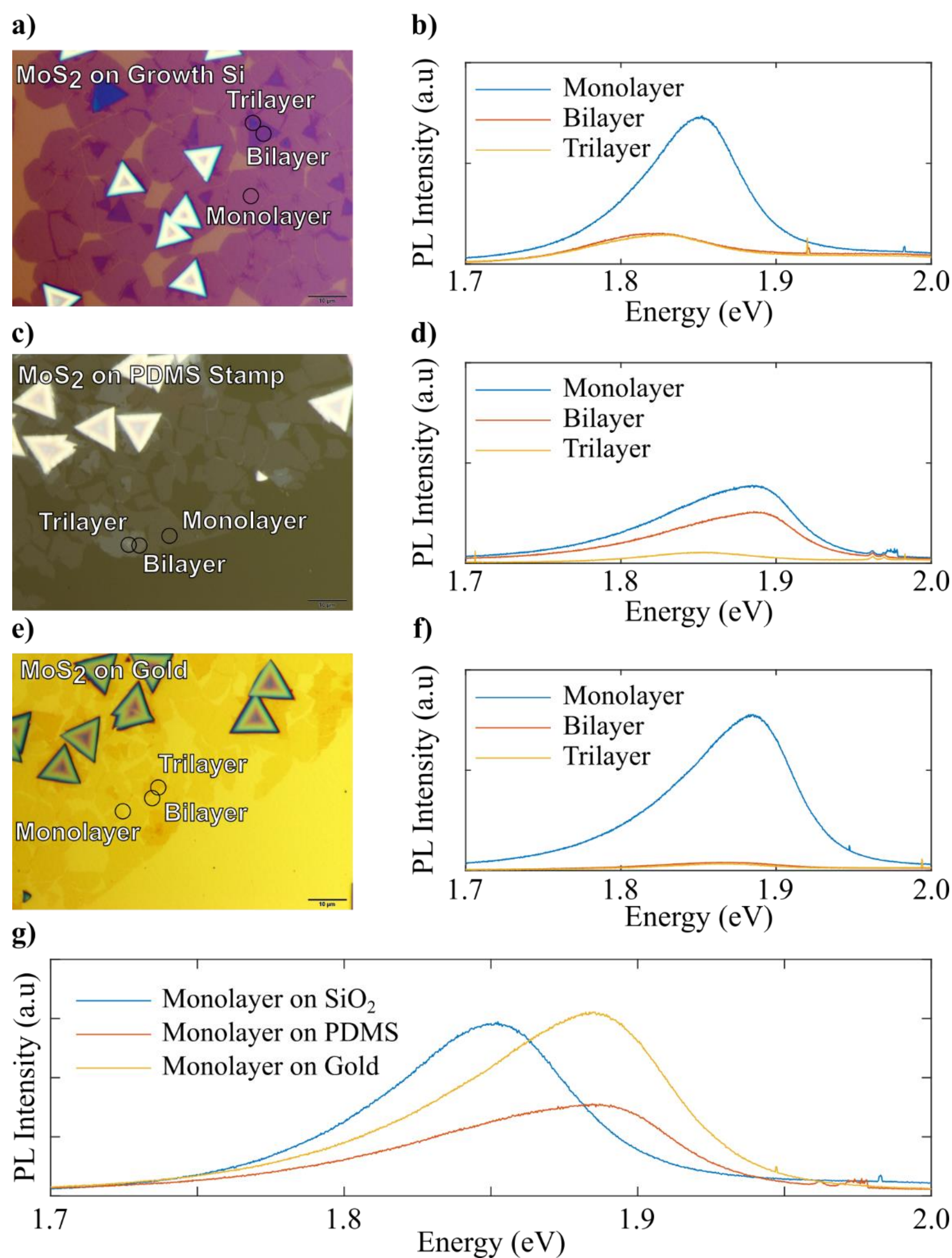

Figure 4.2 Microscope images of the MoS_2 on the growth substrate (a), PDMS stamp (c), and gold (e), with corresponding photoluminescence measurements shown to the right (b, d, f). The three monolayer PL signals on the different substrates are shown together in (g), where there is a peak shift after the MoS_2 is removed from the growth substrate.

The amount of strain experienced in the MoS_2 while on the SiO_2 should be determinable by measuring the peak shift in the PL. A straightforward relation between the shift in energy and the applied strain exits[118], but this is only strictly true when the MoS_2 is being strained on the same substrate. The PL peak location can also be affected by the specific substrate supporting the MoS_2[119]. To avoid this confounding contribution, Raman spectroscopy is used to indirectly measure the strain since this method is not affected by the substrate[120]. Figure 4.3 shows the Raman data of monolayer MoS_2 at each stage of the process, revealing a shift in the *E'* peak of ~ 1.1 cm^{-1}, corresponding to ~ 0.21 % strain. Note that the relative counts on the SiO_2 are also much higher than on the PDMS or gold as indicated by using different axes. The cause of this difference is due to different optical properties of the substrates and not strain related[119].

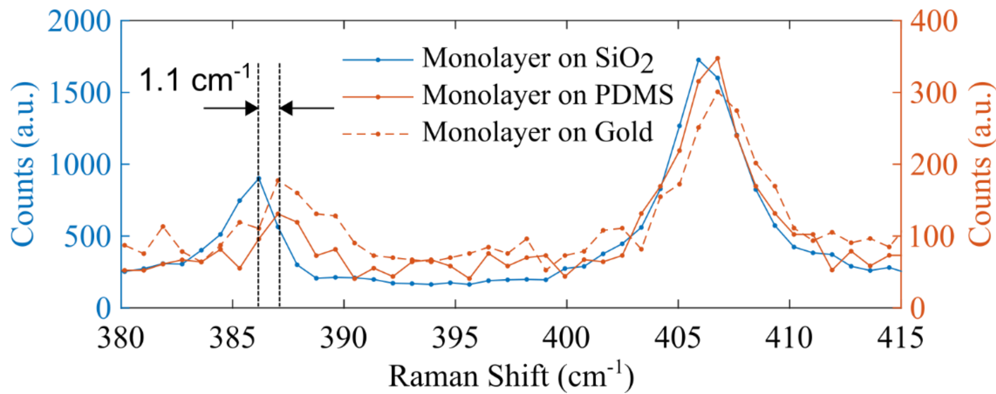

Figure 4.3 Raman spectra of monolayer MoS_2 on SiO_2, PDMS and gold substrates. The locations of these measurements are the same as in Figure 4.2. The shift in the highlighted E' peak indicates the presence of strain when the MoS_2 is on the SiO_2 substrate.

4.2.3. MoS_2 on Gold Thickness Determination

AFM step height measurements on 2D materials have been shown to be somewhat unreliable and dependent on AFM measurement conditions[62,121]. This is exacerbated if the 2D material and its substrate have different mechanical properties[90,119,122]. Additionally,

obtaining step-height measurements on substrates which have a roughness on the order of the film thickness is difficult. Slight variation between different AFM measurements of the same sample have also been seen. To overcome the shortcoming of AFM, Raman spectroscopy and PL measurements can be done to confirm the presence of monolayer MoS_2.

Figure 4.4 shows the characterization of the CVD-grown MoS_2 on the gold substrate. Monolayer MoS_2 is easily visible on the gold substrate, and with each increasing layer present the optical contrast between the MoS_2 and the gold increases. Since a large portion of the MoS_2 is monolayer, it becomes routine to determine the number of layers present with optical contrast in a microscope alone. Raman spectra data shown in Figure 4.4 (b) and PL data shown in Figure 4.4 (c) definitively confirm the presence of monolayer MoS_2. The monolayer and multilayer measurement locations are indicated by the corresponding colored circle in Figure 4.4 (a). The separation of the A_{1g} and E_{2g}^1 peaks (referred to as A_1' and E' peaks in monolayer MoS_2) is roughly 19 cm^{-1} in monolayer MoS_2 and gradually increases with increasing layer thickness. This behavior is observed in the MoS_2 on gold sample shown in Figure 4.4 (b). The PL intensity will also change with varying MoS_2 layer thickness because MoS_2 transitions from an indirect bandgap semiconductor to a direct bandgap semiconductor. The bandgap transition is visible in the PL measurement by observing significantly stronger PL intensities from monolayer MoS_2 vs. multilayer MoS_2 along with a slight shift in energy. The measurements shown in Figure 4.4 (c) exhibits these characteristic behaviors.

Furthermore, tapping-mode AFM is done to further confirm that the layer thickness of the monolayer MoS_2 is approximately equal to its theoretical value of 0.65 nm. Figure 4.4 (d) shows a tapping-mode AFM image of roughly the same area as the optical microscope image shown in Figure 4.4 (a). The white box indicates the location of the

height profile shown to the right in Figure 4.4 (e). The arrow direction indicates the direction of the height profile measurement from 0 nm to 800 nm. The width of the box is to indicate that averaging is performed across its width for a smoother height profile. The height difference between the red and blue lines in the height profile show a height of 0.68 nm, consistent with values for monolayer MoS_2. Although, AFM step height measurements are not reliable enough to be used alone to determine the number of layers for reasons mentioned previously, the AFM results provide useful corroboration of conclusions drawn from the Raman and PL spectra shown in Figure 4.4.

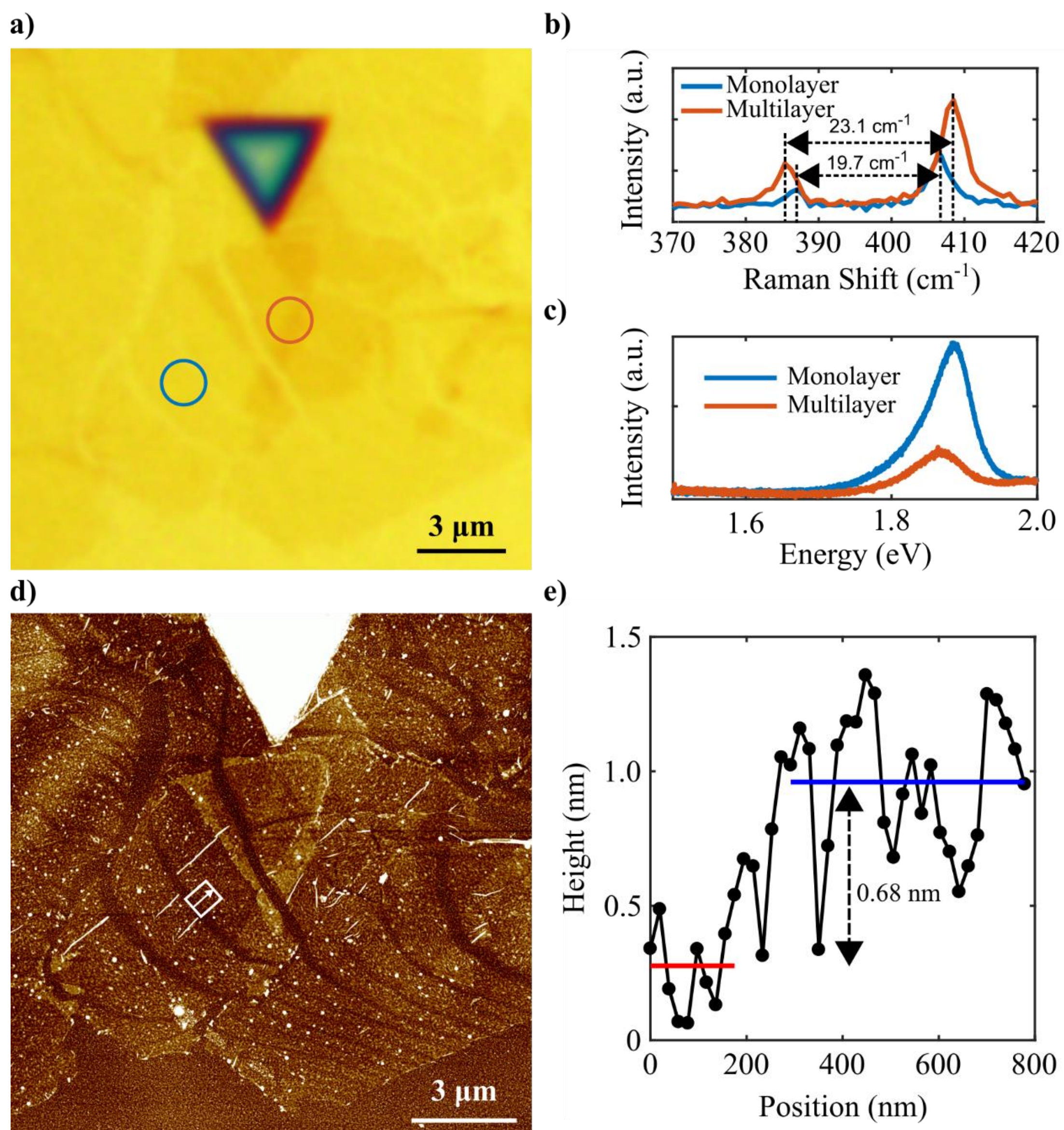

Figure 4.4 Characterization of CVD-grown MoS_2 transferred on gold. Optical microscope image in (a) shows MoS_2 is visible on gold. The colored circles represent the monolayer and multilayer measurement location for Raman (b) and PL (c). Tapping-mode AFM of roughly the same area as (a) is shown in (d). The white box indicates the location of the height profile shown in (e).

4.2.4. MoS_2 on Al_2O_3 Thickness Determination

Locating and characterizing the thickness of MoS_2 transferred onto Al_2O_3 used in this project is more difficult than characterization on gold, PDMS, or SiO_2. The Al_2O_3 film

used here is 5.3 nm thick and deposited directly on top of conductive n^{++} Si; this structure makes light absorption in the MoS_2 layer very difficult, and as a result, monolayer MoS_2 is optically transparent and does not give a detectable Raman or PL signal. This issue is one of the reasons why most 2D materials research is performed on a thicker dielectric layer. Thicker dielectric layers allow for a greater number of internal reflections of the light between the silicon and MoS_2, increasing both optical contrast and light absorption[119]. Additionally, MoS_2 placed directly on a silicon surface does not absorb enough light for a measurable Raman and PL signal due to quenching[123]. Further evidence for this explanation is provided in a recent study which shows that MoS_2 on thin Al_2O_3 is expected to have very poor optical contrast[124].

Figure 4.5 (a) exemplifies this by showing an optical image of CVD-grown MoS_2 transferred onto Al_2O_3 where only the thick triangular regions are visible. Tapping-mode AFM is needed to reveal the presence and positioning of the MoS_2 on the Al_2O_3 surface and is shown in Figure 4.5 (b). Attempts at characterization with Raman and PL are unsuccessful in the monolayer areas because not enough light is coupled into the MoS_2. The Raman results are shown in Figure 4.5 (c).

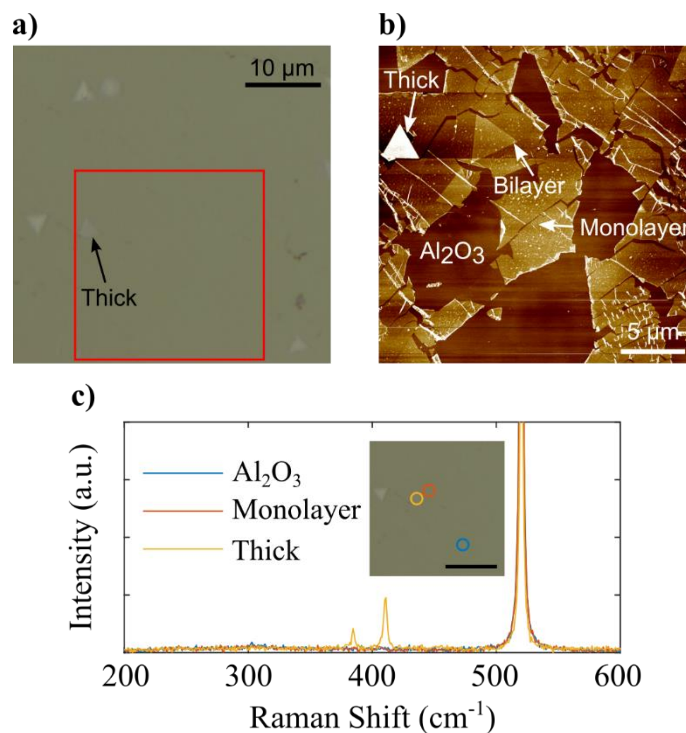

Figure 4.5 Optical microscope image of CVD-grown MoS_2 transferred onto a thin layer of Al_2O_3 on Si where the monolayer MoS_2 is not visible is shown in (a). A tapping-mode AFM image of the red boxed area is shown in (b) where the location of the MoS_2 becomes apparent. Raman spectroscopy measurements are shown in (c), where the non-optically-visible monolayer area does not give a detectable signal but the barely-visible thick MoS_2 does give a detectable signal. The areas of measurement are depicted and color-coded in the inset, where the 'thick' measurement is on the same location as labeled in (a) and (b). The inset scale bar is 10 µm and the large peak around 520 cm^{-1} is from the underlying Si substrate.

To more definitively confirm the presence of monolayer MoS_2 areas on the Al_2O_3 surface, a combination of techniques is used. First, tapping mode AFM is used to estimate the number of layers present, but as mentioned previously, this measured value may be inflated and should not be used alone. A tapping-mode AFM image of the MoS_2 on Al_2O_3 sample, taken a few months after the initial PFM measurement, is shown in Figure 4.6. The monolayer step height measured in Figure 4.6 (b) is, in fact, larger than monolayer

thickness, but this is not unexpected[62,121]. The value of the step height from monolayer to bilayer is more reliably accurate since the material is consistent over the step, and the AFM measurement here further confirms this assessment by showing the expected height of a single-layer step. This AFM measurement shows that the MoS_2 is likely monolayer, but the inflated thickness value could also be possible in bilayer or few layer MoS_2. Extra measurements are needed for further confirmation.

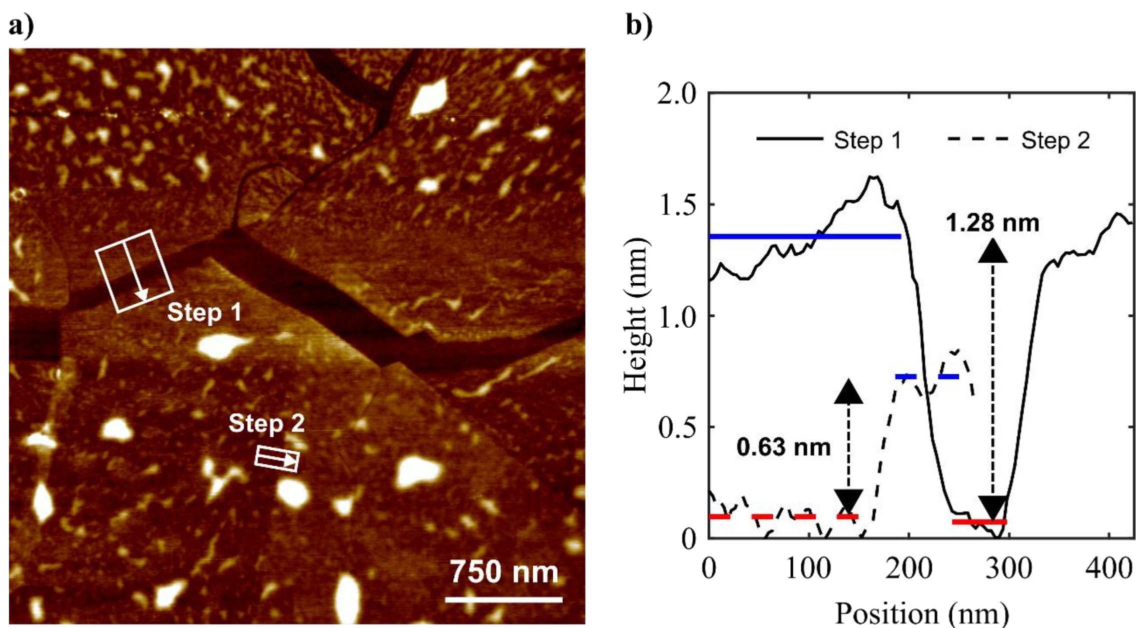

Figure 4.6 Tapping mode AFM measurement of monolayer and bilayer MoS_2 on Al_2O_3 is shown in (a). The area shown here corresponds to the area near the label of bilayer in Figure 4.5 (b). Height profiles along the white boxes are given in (b). Step 1 shows the height from monolayer to Al_2O_3 substrate to monolayer again. Step 2 shows a step from monolayer to bilayer MoS_2. The monolayer thickness is inflated when measured from the substrate.

Next, the MoS_2 remaining on the growth substrate after the transfer process is analyzed to show that monolayer MoS_2 on this substrate also gives inflated thickness values. Figure 4.7 shows CVD-grown MoS_2 on its growth substrate of SiO_2. This is the same sample which was used to create the MoS_2 on Al_2O_3 sample, which means that the

MoS_2 did not completely transfer off the growth substrate. Figure 4.7 (a) shows the tapping-mode AFM measurement of monolayer, bilayer, and multilayer MoS_2 with a corresponding optical microscope image given in Figure 4.7 (b). Figure 4.7 (c) shows height profiles along the white boxes in (a). In this case, both values are inflated, highlighting the uncertainty associated with AFM height measurement of monolayer materials. Figure 4.7 (d) shows a color-coded Raman map in the region enclosed by the white box in Figure 4.7 (b) and depicts the integrated intensity of the A_{1g} Raman peak. As expected, the total relative intensity of the Raman signal increases with increasing number of layers. Finally, Figure 4.7 (e) shows the Raman measurements for monolayer, bilayer, and 3-4 layers of MoS_2 at the locations circled in Figure 4.7 (b). As expected, monolayer MoS_2 has a peak separation of roughly 19 cm^{-1} and an increasing separation with increasing number of layers present. These data show that for the MoS_2 on the growth substrate, which is the same MoS_2 as on the Al_2O_3, most of the MoS_2 is monolayer with interspersed thicker triangular areas. This is the same general geometry as seen on the Al_2O_3 sample, giving further evidence that the areas of interest are monolayer. Additionally, no thinner areas of MoS_2 have been located on the Al_2O_3 sample.

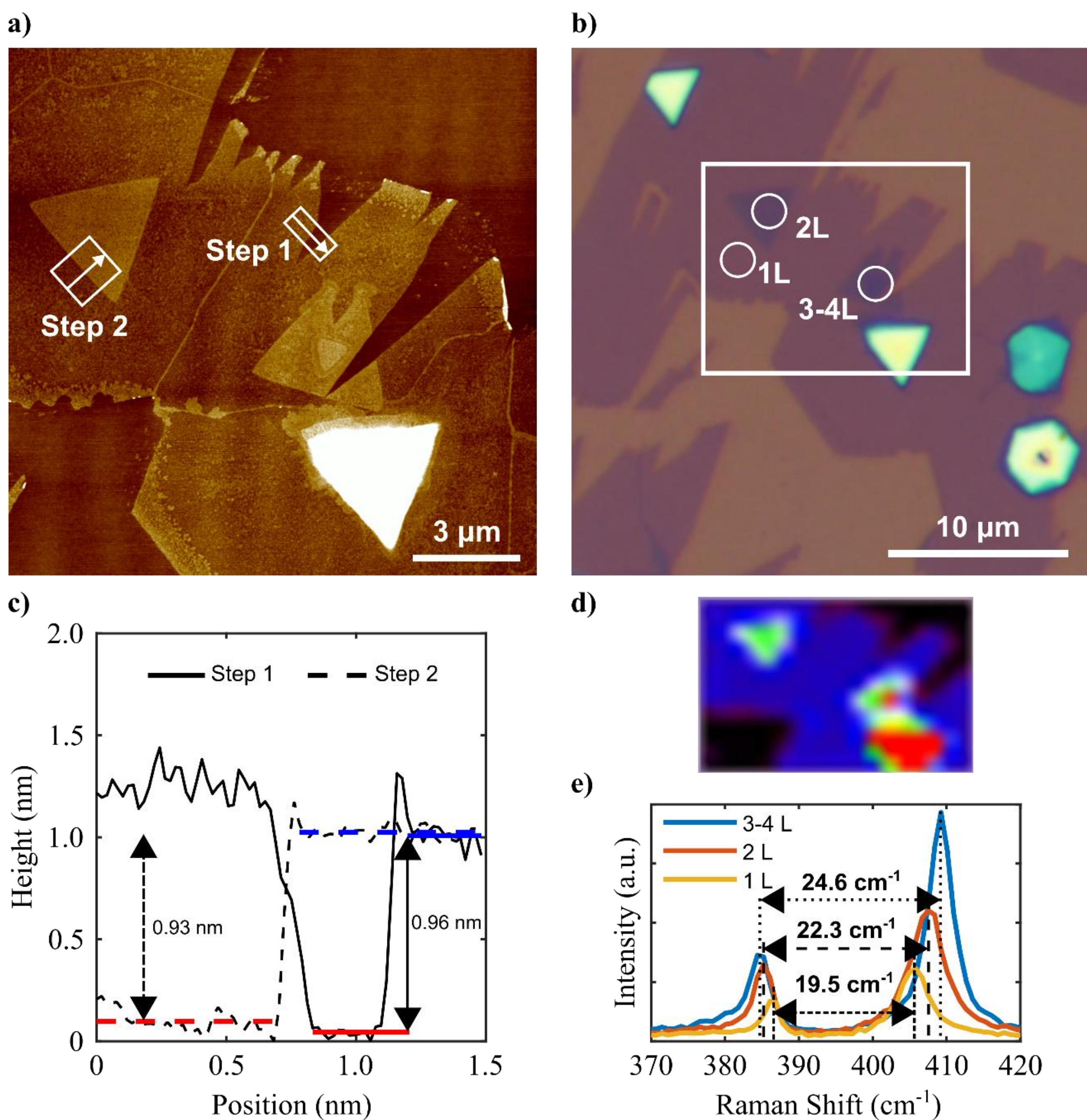

Figure 4.7 CVD-grown MoS_2 on its SiO_2 growth substrate. (a) shows a tapping-mode AFM image, where the two boxes indicate the locations of the step heights plotted in (c). An optical microscope image is shown in (b), where the white box indicates the location of the color-coded Raman map in (d). In increasing intensity, black shows no MoS_2, blue shows monolayer MoS_2, green shows bilayer, and yellow and red show multilayer MoS_2. The white circles indicated in (b) show the location of Raman spectral measurements in (e).

4.3. PFM Results

4.3.1. MoS_2 on Gold

The successfully transferred and characterized monolayer MoS_2 on gold can now be tested for the presence of out-of-plane electromechanical coupling. PFM is used to test for the electromechanical response and has been described in detail in Chapter 3. The experiment-specific details will be discussed in this section. The purpose of having MoS_2 directly on gold is to be able to concentrate the electric field within the MoS_2 between the AFM tip and gold substrate. Gold was chosen because of its stability in air and high electrical conductivity. An optical image of the MoS_2 on gold which highlights the area measured with PFM is shown in Figure 4.8 (a), and a schematic of the sample with the AFM tip and the approximate electric field is shown in Figure 4.8 (b).

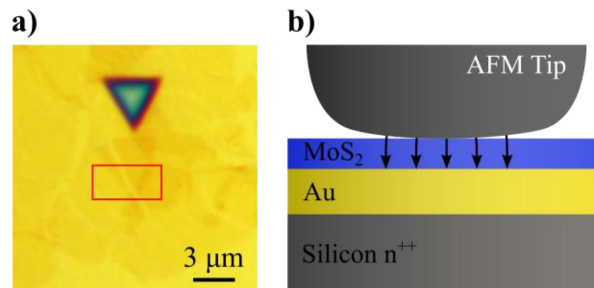

Figure 4.8 An optical image of the MoS_2 on gold is shown in (a) where the red box indicates the area imaged by PFM in Figure 4.9. A schematic of the MoS_2 on gold sample is shown in (b). The AFM is purposely drawn broad because on the scale of monolayer MoS_2 and with tip wear, the AFM tip will be broad in comparison to the MoS_2 thickness.

The PFM was performed using cobalt-chromium coated AFM probes (Bruker MESP-RC-V2), a drive voltage of 8 V and a drive frequency of 60 kHz. Immediately after the PFM image is taken with the drive voltage applied to the sample, a second PFM image is taken without the drive voltage applied to the sample. This is, as mentioned in the

previous chapter, a type of control measurement and a second measure of the inherent background signal in the system. Figure 4.9 shows the two sets of PFM images.

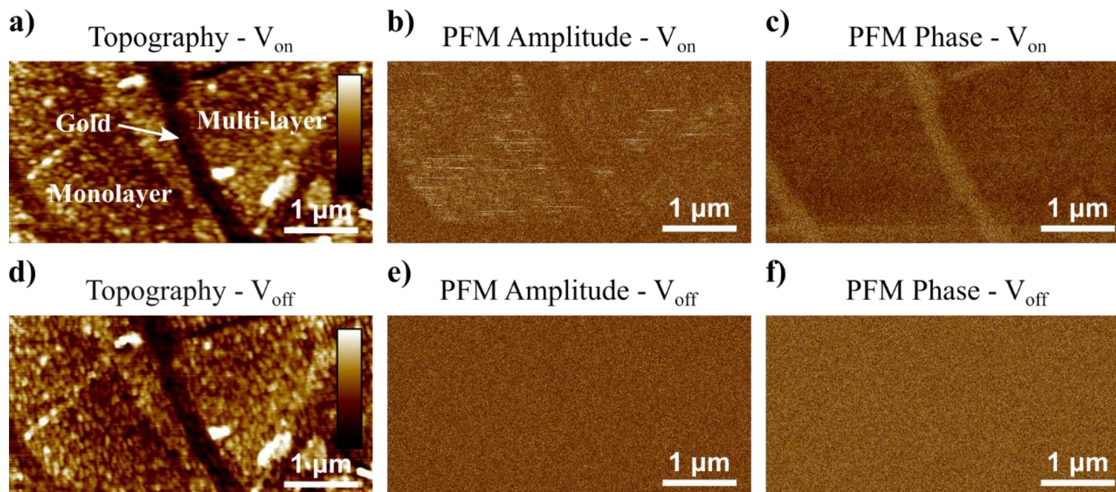

Figure 4.9 The PFM measurements of the MoS_2 on gold sample. The drive voltage is applied in (a) – (c) and the drive voltage is not applied in (d) – (f). The topography images (a) and (d) show the background gold substrate, monolayer MoS_2, and multi-layer MoS_2 regions. The applied drive voltage does not affect the topographic measurement (color bar is 0 nm to 5 nm for both). The PFM amplitude images (b) and (e) show that the MoS_2 region has contrast against the gold substrate only when the drive voltage is applied (b). The same is true for the PFM phase images (c) and (f). Both amplitude images and phase images share the same color scale.

Since PFM is a type of contact-mode AFM measurement, a simultaneous topography image in Figure 4.9 (a) is obtained with the PFM amplitude and phase channels. The topography shows the location of the monolayer, multilayer, and underlying gold substrate. Figure 4.9 (b) and (c) then show clear contrast between the locations of the MoS_2 and underlying gold substrate. This contrast indicates that there is an electromechanical response occurring in the MoS_2 region. The conducting, gold substrate should have zero electromechanical response because conductors cannot be electromechanically active, so the PFM measurement on the gold serves as an indication of the zero-level response.

Further confirmation that the MoS_2 is the cause of the PFM signal can be seen when the drive voltage is not applied to the sample in Figure 4.9 (d) to (f). Without the drive voltage applied, there cannot be any electromechanical response of the sample, so the amplitude and phase measurements in Figure 4.9 (e) and (f) should have similar values to that of the non-electromechanically active gold area in Figure 4.9 (b) and (c). This is in fact the case, supporting the claim that MoS_2 is causing the observed signal in the PFM measurement. Additionally, the disappearance of the contrast in Figure 4.9 (e) and (f) indicate that there are no scanning artifacts present.

Next, quantitative analysis is done with the PFM data to obtain an estimate of d_{33}^{eff} for MoS_2 on gold. Three vectors are created by averaging amplitude and phase data take on monolayer MoS_2 area, gold area, and data taken in the voltage-off condition. The vector background-subtraction process is then performed with the MoS_2 and gold vectors to obtain 0.93 ± 0.23 pm V^{-1} for MoS_2. Using the MoS_2 vector and the voltage-off condition vector for the background-subtraction, 1.12 ± 0.20 is obtained. These two values are, as expected, similar and within the experimental uncertainty values of each other. The values are summarized in Table 3.1.

4.3.2. MoS_2 on Al_2O_3

The MoS_2 on Al_2O_3 sample was created to complement the MoS_2 on gold sample. Since monolayer MoS_2 is so thin, there was a concern that current flow may occur and affect the PFM measurements. The Al_2O_3 in these samples is an insulator and serves as a current blocking layer. Placing the MoS_2 directly on the Al_2O_3 should limit any possible current flow and provide a complimentary electromechanical measurement of MoS_2. An added complication in this sample is that the voltage will be dropped across two different materials of different thickness and dielectric constants, reducing the electric field present

within the MoS_2. Figure 4.10 (a) shows a tapping-mode AFM image of MoS_2 on Al_2O_3 where the red box indicates the location of the PFM measurement in Figure 4.11. Figure 4.10 (b) shows a schematic of the sample, where the underlying silicon n^{++} acts as the bottom electrode and the black arrows illustrate the approximate electric field.

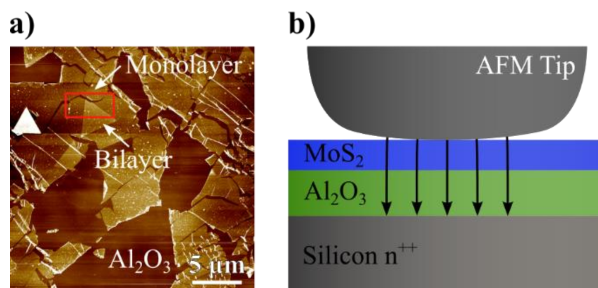

Figure 4.10 A tapping-mode AFM image of the MoS_2 on Al_2O_3 is shown in (a) where the red box indicates the area imaged by PFM in Figure 4.11. A schematic of the MoS_2 on Al_2O_3 sample is shown in (b). The MoS_2 is transferred onto Al_2O_3 to limit current flow through MoS_2 to the bottom electrode. The AFM is purposely drawn broad because on the scale of monolayer MoS_2 and with tip wear, the AFM tip will be broad in comparison to the MoS_2.

The PFM was performed under the same conditions as the MoS_2 on gold sample, so the results are directly comparable. The same AFM probe type was used as well, but a new and previously unused version is used for the measurement. This ensures that there is minimal tip wear to start each experiment, but the initial tip geometry may vary slightly from tip-to-tip. The results are shown in Figure 4.11 for both having the drive voltage applied and not applied to the sample.

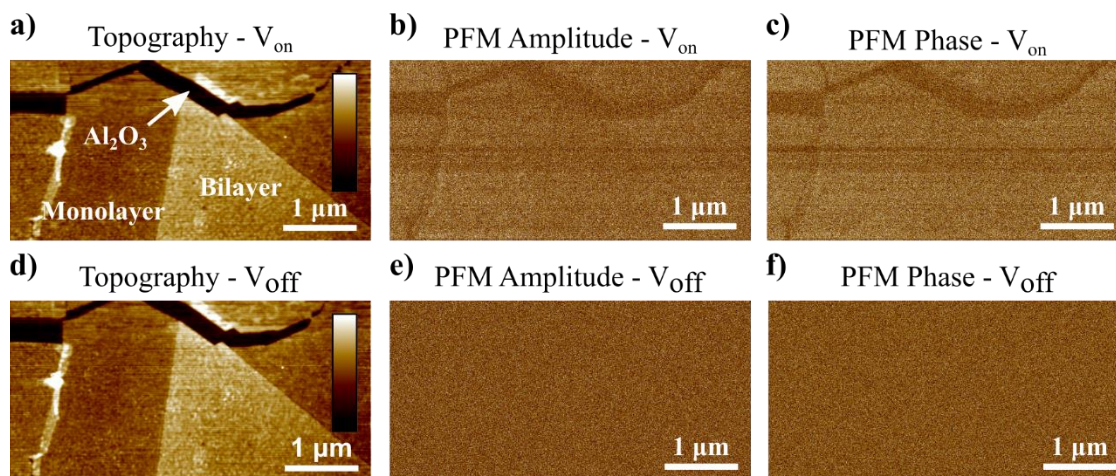

Figure 4.11 The PFM measurements of the MoS_2 on Al_2O_3 sample. The drive voltage is applied in (a) – (c) and the drive voltage is not applied in (d) – (f). The topography images (a) and (d) show the background Al_2O_3 substrate, monolayer MoS_2, and bilayer MoS_2 regions. The applied drive voltage does not affect the topographic measurement (color bar is 0 nm to 3.7 nm for both). The PFM amplitude images (b) and (e) show that the MoS_2 region has contrast against the Al_2O_3 substrate only when the drive voltage is applied (b). The same is true for the PFM phase images (c) and (f). Both amplitude images and phase images share the same color scale.

The topography channel of the PFM measurement reveals the locations of the MoS_2 monolayer, bilayer, and underlying Al_2O_3 substrate. Similar to the MoS_2 on gold sample, there is clear contrast in the PFM amplitude and phase images between the MoS_2 region and the Al_2O_3 region only when the drive voltage is applied. In the voltage-off condition, the contrast vanishes indicating that there are no scanning artifacts in the PFM measurement. The value of the PFM amplitude and phase measurements in the voltage-off condition are also very similar to the Al_2O_3 signal when the drive voltage is applied, confirming that the Al_2O_3 is not electromechanically active.

In order to perform quantitative analysis on the MoS_2 on Al_2O_3 sample, first the voltage drop within the MoS_2, V_{MoS_2}, and Al_2O_3, $V_{Al_2O_3}$, needs to be estimated. Assuming

the electric flux density through the two materials is equal and using a simple planar capacitance model for an estimation, the equation

$$\epsilon_{MoS_2} E_{MoS_2} = \epsilon_{Al_2O_3} E_{Al_2O_3}, \tag{4.1}$$

can be used. Here, ϵ_{MoS_2}, $\epsilon_{Al_2O_3}$, E_{MoS_2}, and $E_{Al_2O_3}$ are the permittivity of the MoS_2 and Al_2O_3, and the electric field within MoS_2 and Al_2O_3, respectively. The electric field in each material is then given by

$$E_i = -\frac{V_i}{t_i}, \tag{4.2}$$

where t is the thickness of the material and the subscript i is interchangeable depending on the material being considered. Combining Equations (4.1) and (4.2) gives

$$\epsilon_{MoS_2} \frac{V_{MoS_2}}{t_{MoS_2}} = \epsilon_{Al_2O_3} \frac{V_{Al_2O_3}}{t_{Al_2O_3}}. \tag{4.3}$$

Now, by using

$$V_{MoS_2} + V_{Al_2O_3} = V_d, \tag{4.4}$$

where V_d is the drive voltage amplitude, the result for an estimate of the amount of voltage dropped only within the MoS_2 is given by

$$V_{MoS_2} = V_d \frac{\epsilon_{Al_2O_3}/t_{Al_2O_3}}{\epsilon_{MoS_2}/t_{MoS_2} + \epsilon_{Al_2O_3}/t_{Al_2O_3}}. \tag{4.4}$$

Plugging in values into Equation (4.4) from the experiment ($\epsilon_{Al_2O_3}$ = 9, ϵ_{MoS_2} = 4 from reference[125], t_{MoS_2} = 0.65 nm, and $t_{Al_2O_3}$ = 5.3 nm from ellipsometry measurements), a drive voltage of V_d = 8 V results in V_{MoS_2} = 1.73 V.

The calculated value of V_{MoS_2} can now be substituted for V_d in the equations used to calculate d_{33}^{eff}. Performing the vector background subtraction with the averaged monolayer MoS_2 data and the Al_2O_3 data, d_{33}^{eff} is calculated to be 1.34 ± 0.27 pm V^{-1}. When using the voltage-off condition as the background measurement, d_{33}^{eff} is calculated

to be 1.35 ± 0.20 pm V^{-1}. These two numbers are exceptionally close to each other, indicating that that there is little, if any, contribution to the PFM measurement caused by the substrate. The values are summarized in Table 4.1.

Additionally, DC voltage sweeps are performed while measuring the PFM amplitude to check for electrostatic contributions to the PFM measurement. Figure 4.12 shows two voltage sweeps, one taken on a single spot on the MoS_2 and one taken on a single spot on the Al_2O_3. As described in the previous chapter, if electrostatic forces are playing a role in the PFM measurement, the expected relationship between the DC bias and PFM amplitude is an absolute value dependence centered at the workfunction difference between the AFM tip and the MoS_2 or Al_2O_3. Figure 4.12 shows the PFM amplitude is independent of the DC bias, allowing the influence of electrostatic force to be ruled out as a cause of the PFM signal.

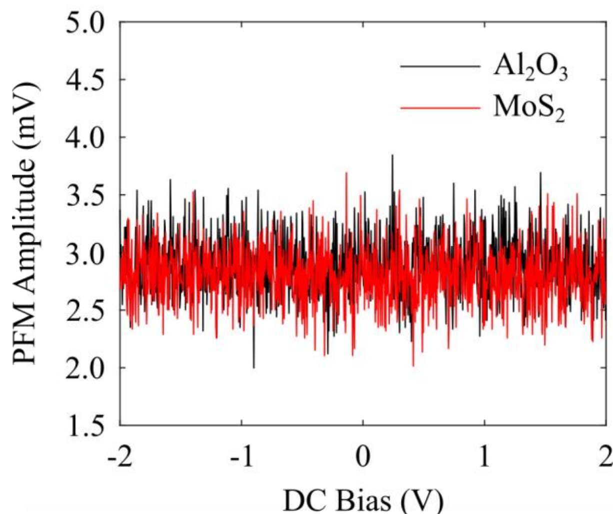

Figure 4.12 The response of the PFM amplitude with a DC Bias sweep applied in addition to the AC drive voltage. There is no dependence on DC bias seen in this measurement, meaning that there are no electrostatic force contributions present in the PFM measurement.

4.4. DISCUSSION

4.4.1. Results Summary and Comparison

The d_{33}^{eff} values calculated for MoS_2 on gold and on Al_2O_3 are summarized in Table 4.1. There are three separate columns which are used to compare the three vectors created from the PFM data. The first two columns are calculated via vector background subtraction using the MoS_2 vector with the substrate vector (gold or Al_2O_3) and the voltage-off condition vector. The last column compares the vectors created from the substrate data and the voltage-off condition. The data in this column should be small and represents the amount of signal measured during the PFM experiment which is caused by the substrate.

Sample	MoS_2 vs. Substrate (pm/V)	MoS_2 vs. V_{off} (pm/V)	Substrate vs. V_{off} (pm/V)
MoS_2 on Gold	0.93 ± 0.23	1.12 ± 0.20	0.19 ± 0.10
MoS_2 on Al_2O_3	1.34 ± 0.27	1.35 ± 0.20	0.04 ± 0.15

Table 4.1 The calculated d_{33}^{eff} values for MoS_2 on gold and on Al_2O_3. The three columns represent different comparisons between the three PFM vectors created from the data. The first subtracts the background signal measured on the substrate and the second subtracts the background signal measured on the voltage-off condition. The third compares the two background conditions

The electromechanical coupling of MoS_2 is expected to be the same regardless of the substrate. The measurements obtained in this research show that the d_{33}^{eff} values differ slightly on gold versus Al_2O_3 but are still within experimental uncertainty. Added error may also arise when estimating the electric field within the MoS_2 on Al_2O_3. A simple parallel-plate capacitor model was used to estimate the voltage drop across the MoS_2 and Al_2O_3, when in reality a more complex relationship may be needed. Additionally, if current flow is present in the gold sample, the electric field would be affected and diminished

slightly due to screening. This could be a hand-waving explanation as to why the Al_2O_3 sample has a larger response than the gold sample.

4.4.2. Flexoelectricity as the Signal Origin

Now that a quantitative description of the out-of-plane electromechanical response of MoS_2 has been detected and measured, a deep look into its origin is needed. With the background subtraction techniques and DC bias sweeps done to rule out other possible contributions to the PFM signal, the source must be coming from an electromechanical effect. The first effect to consider is piezoelectricity, which is what PFM was originally designed to measure. The piezoelectric tensor for monolayer MoS_2 can be written as[16]

$$d_{ij} = \begin{bmatrix} d_{11} & -d_{11} & 0 & 0 & 0 & 0 \\ 0 & 0 & 0 & 0 & 0 & -2d_{11} \\ 0 & 0 & 0 & 0 & 0 & 0 \end{bmatrix}, \tag{4.5}$$

where the indices correspond to those in the following definition of converse piezoelectricity:

$$\varepsilon_j = d_{ij} E_i. \tag{4.6}$$

Here, ε_j is the strain tensor employing Voigt notation and E_i is the electric field. It is important to note that the piezoelectric tensor for MoS_2 has non-zero components only within the plane of its atoms and is zero for all out-of-plane components. This indicates that there should be no piezoelectric effect out-of-plane. However, the experiments yield a non-zero value for d_{33}^{eff}, suggesting that this signal could be originating from the flexoelectric effect instead of the piezoelectric effect.

The converse flexoelectric tensor for MoS_2 is given by[116]

$$\mu_{mn}^* = \begin{bmatrix} \mu_{11}^* & 0 & 0 & 0 & \mu_{15}^* & 0 & 0 & 0 & \mu_{19}^* \\ \mu_{11}^* & 0 & 0 & 0 & \mu_{11}^* & 0 & 0 & 0 & \mu_{19}^* \\ \mu_{31}^* & 0 & 0 & 0 & \mu_{31}^* & 0 & 0 & 0 & \mu_{39}^* \\ 0 & 0 & 0 & 0 & 0 & \mu_{46}^* & 0 & \mu_{48}^* & 0 \\ 0 & 0 & \mu_{46}^* & 0 & 0 & 0 & \mu_{48}^* & 0 & 0 \\ 0 & \mu_{11}^* - \mu_{15}^* & 0 & \mu_{11}^* - \mu_{15}^* & 0 & 0 & 0 & 0 & 0 \end{bmatrix} \quad (4.7)$$

where the * indicates that the converse representation is being used and the indices are defined using the converse flexoelectric equation

$$\sigma_{ij} = \mu_{ijkl}^* \frac{\partial E_k}{\partial x_l}, \quad (4.8)$$

where σ_{ij} is the stress tensor. The four indices can be transformed to two by using Voigt notation[116] for *ij*, while *kl* follow 11 → 1, 12 → 2, 13 → 3, 21 → 4, 22 → 5, 23 → 6, 31 → 7, 32 → 8, 33 → 9 to yield μ_{mn}^*.

To a good approximation, the electric field within the MoS_2 layer can be assumed to be perpendicular to the surface of the gold and thus the plane of the MoS_2 atoms. With this assumption, the contribution of the first six columns of Equation (4.7) to the electromechanical response of MoS_2 can be neglected in this experiment. Also, the first two rows describe stresses created in-plane, which will not influence the PFM measurement. Possible contributions to an out-of-plane electromechanical response from an out-of-plane electric field then include μ_{39}^* and μ_{48}^*. The former is an out-of-plane stress caused by a vertical electric field changing through the thickness of the MoS_2. The latter is an out-of-plane shear-stress mode caused by a vertical electric field varying laterally as it spreads away from the AFM tip.

In general, a superposition of both μ_{39}^* and μ_{48}^* could contribute to a measurable d_{33}^{eff} value. Although the electromechanical response can be thought of as an effective piezoelectric response, considering the above analysis, it may be more appropriate to refer to the value in this case as an effective flexoelectric response, μ_{eff}^*.

To estimate μ_{eff}^{*} from d_{33}^{eff}, Equations (4.6) and Equation (3.2) are examined in finer detail. By doing a PFM measurement, converse piezoelectricity is used to effectively measure the strain caused by an applied electric field. Using the definition of strain,

$$\varepsilon_3 = \frac{\Delta z}{t}, \tag{4.9}$$

where Δz is the vertical deflection measured by the PFM and t is the thickness of the material being measured, Equation (4.6) can be written as

$$d_{33}^{eff} = \frac{\Delta z}{tE_3}. \tag{4.10}$$

This is similar to Equation (3.2) where Δz contains the deflection sensitivity, s_d, and the gain factor, and therefore represents the actual deflection of the sample.

Now consider the different components in Equation (4.8) which may be present in MoS_2 if the electric field is assumed to be perpendicular to the surface of the gold and MoS_2:

$$\sigma_1 = \mu_{19}^{*}\frac{\partial E_3}{\partial x_3}, \tag{4.11}$$

$$\sigma_2 = \mu_{19}^{*}\frac{\partial E_3}{\partial x_3}, \tag{4.12}$$

$$\sigma_3 = \mu_{39}^{*}\frac{\partial E_3}{\partial x_3}, \tag{4.13}$$

$$\sigma_4 = \mu_{48}^{*}\frac{\partial E_3}{\partial x_2}, \tag{4.14}$$

$$\sigma_5 = \mu_{48}^{*}\frac{\partial E_3}{\partial x_1}. \tag{4.15}$$

Of these components, σ_1 and σ_2 will create in-plane stress which may or may not create out-of-plane displacement due to Poisson-like effects. In Equation (4.14) and (4.15), the out-of-plane shear stress components σ_4 and σ_5 could create contributions to measured out-of-plane displacement. The most likely out-of-plane displacement would be due to Equation (4.13) where an out-of-plane electric field changing in the z-direction causes

stress is the z-direction. This is plausible because the gradient is taken over the very short distance of a single monolayer of MoS_2.

For simplicity, the geometry and response of the system is assumed to be approximated by Equation (4.13) and μ^*_{eff} is substituted for μ^*_{39}. Next, the dominant electric field derivative term, $\partial E_3/\partial x_3$, is approximated, at these small length scales, as $\partial E_3/\partial x_3 \approx 2V_d/t^2$. This assumption corresponds to a linear dependence of E_3 on x_3, and a quadratic dependence of the electrostatic potential on x_3, within the MoS_2 layer. The total potential drop across the MoS_2 layer is also set equal to V_d. Finally, using $\sigma = Y\varepsilon$ and Equation (4.10), Equation (4.8) can be rewritten as

$$\mu^*_{eff} = \frac{\Delta z}{V_d} \cdot Y \cdot \frac{t}{2} = d_{33}^{eff} \cdot Y \cdot \frac{t}{2}. \tag{4.16}$$

Assuming $Y = 270$ GPa and $t = 0.65$ nm for monolayer MoS_2, Equation (4.16) yields 0.08 nC m^{-1} and 0.12 nC m^{-1}, based on PFM measurements for MoS_2 on gold and Al_2O_3, respectively. This serves only as an order-of-magnitude estimate of μ^*_{eff} because of the assumptions made. These estimates are also calculated from measurements on monolayer MoS_2 and further work is needed to analyze the flexoelectric response with increasing MoS_2 thickness.

The values estimated for the effective flexoelectric constant of MoS_2 are of a reasonable magnitude. Previous studies[11] have reported that perovskite ceramics in the paraelectric phase have a μ_{eff} on the order of 1-100 μC m^{-1} while single crystal perovskites are on the order of 1 nC m^{-1}. Values of μ_{mn} obtained with different measurement techniques and those obtained via experiment versus theory can also vary by orders-of-magnitude but are slowly converging. Values of MoS_2 μ_{eff} would be expected to be less than those of perovskites since MoS_2 has a lower dielectric susceptibility, so the values estimated from the experiments are reasonable.

A further step of estimating what may be expected for the flexoelectric response of MoS_2 can be done by using an order-of-magnitude estimation method developed by Kogan[126]. This method estimates the flexocoupling coefficient with the equation

$$f \approx \frac{q}{4\pi\epsilon_0 a}, \quad (4.17)$$

where a is the lattice constant of the material. The model originates[10] from considering point charges separated with interatomic spacing of a, distorted by a strain gradient of order $1/a$. With the definition

$$\mu \equiv \chi f, \quad (4.18)$$

where χ is the dielectric susceptibility of MoS_2, an order-of-magnitude estimate of μ_{mn} can be obtained for MoS_2. Taking a = 3.2 Å, and $\chi = 3\epsilon_0$, the estimated μ_{mn} for MoS_2[29,125] is 0.12 nC/m. This is remarkably similar to the values derived from the experiments above, giving validity that the response may be from a flexoelectric effect rather than a piezoelectric effect.

4.4.3. Contamination Issues

The possibility of contamination on MoS_2 causing the measured out-of-plane electromechanical effects should not be overlooked. X-ray photoelectron spectroscopy (XPS) as performed to look for surface contaminants that could affect the PFM signal. Three separate samples were measured: 1) the MoS_2 on gold sample for which PFM images are shown in Figure (4.9), 2) gold deposited on an Si/SiO_2 substrate, and 3) gold deposited on an Si/SiO_2 substrate that was stamped with PDMS without MoS_2. Table 4.2 shows the concentration of various elements detected on the surfaces of the samples.

Element	Gold Only	PDMS-Stamped Gold	MoS_2 on Gold
Au	62.0 %	56.4 %	37.3 %
C	34.2 %	35.2 %	39.0 %
O	3.8 %	6.0 %	16.1 %
Si	0 %	2.4 %	5.6 %
Mo	0 %	0 %	0.9 %
S	0 %	0 %	1.1 %

Table 4.2 XPS measurements of the materials found on the surface of three different samples. First is pristine gold-coated silicon, second is gold-coated silicon which was stamped with PDMS, third is the sample used in the PFM measurement which is gold-coated silicon with MoS_2 transferred onto the surface with a PDMS stamp.

A notable amount of carbon is detected on all of the samples, most of which is likely from adventitious carbon which is found on all samples exposed to air. The samples which were stamped with PDMS show increased levels of oxygen and silicon compared to the non-stamped gold sample. Residue left on the sample from the stamping process, or unreacted MoO_3 from the CVD growth processes, most-likely are the culprits of the increase. Since the silicon and oxygen increase is also seen on the gold sample without the MoS_2, it is assumed that any PDMS residue is blanket-deposited wherever the PDMS contacts and does not preferably attach to the MoS_2. This means that if the PDMS residue contributes to the PFM signal, its contribution to the MoS_2 signal can be removed by doing the background subtraction process with the substrate PFM measurement. One possible complication would be if the PDMS residue interacts differently with the MoS_2 than with the gold or Al_2O_3 substrates. More work is needed to rule out any such effects.

Also noted is that the typical magnetic lens used for XPS measurements could not be used for the MoS_2/gold sample because it was mounted on a magnetic AFM disk for

better electrical contact during PFM measurements. Only the electrostatic lens was used for this sample, so the % concentration values may not be precise and represent a broader range of possible percentages.

4.5. CONCLUSIONS AND SIGNIFICANCE

This work shows that monolayer MoS_2 exhibits an out-of-plane electromechanical response with a d_{33}^{eff} of 1.03 ± 0.22 pm V^{-1} on gold and 1.35 ± 0.24 pm V^{-1} on Al_2O_3. There is strong evidence that its origin is from the flexoelectric effect rather than the piezoelectric effect, and an estimate of the effective flexoelectric coefficient μ_{eff}^{*} yields 0.10 nC m^{-1}. The presence of flexoelectricity in 2D materials has implications across many fields. In 2D material electronics, for example, roughness in the substrate surface could create local curvature and thus local polarization that could affect electronic device performance[127]. It also opens the door to making new types of nanoscale sensors, actuators, or energy harvesters which could be used in conjunction with piezoelectricity to enhance operation.

Plus, if MoS_2 exhibits flexoelectric effects, other TMD materials should also exhibit flexoelectricity. This allows for a new platform to study the flexoelectric effect which has been notoriously difficult to investigate and characterize. The next chapter will investigate the response of other TMD materials and compare the magnitude of their responses to each other. Keeping in mind how flexoelectricity may vary with certain parameters, the response from one TMD to the next could give insight into the validity of the models which describe flexoelectricity.

Chapter 5:

Comparison of Electromechanical Responses Between TMDs[v]

As described in Chapter 4, MoS_2 was found to exhibit an out-of-plane electromechanical response by using the PFM measurement techniques developed in the Chapter 3. In this chapter, the TMDs $MoSe_2$, WS_2, and WSe_2 are measured with PFM to determine if they also exhibit out-of-plane electromechanical coupling, and if so, how the magnitude of their responses compare to that of MoS_2. It was determined that all the TMDs measured are electromechanically active and three of the four TMDs approximately follow a trend predicted by a simple model for flexoelectricity.

[v] The work presented in this chapter is currently unpublished.

5.1. INTRODUCTION

The previous chapters have focused on understanding the adhesion properties that are useful for fabrication of devices, the measurement technique of PFM that is needed for the electromechanical measurements, and the implementation of PFM to measure the response of MoS_2. This chapter will bring the ideas from the previous chapters together and apply them to measure a suite of TMD materials and analyze their results.

The result that MoS_2 exhibits out-of-plane electromechanical coupling found in Chapter 4 allows for a broader study investigating if, and by what magnitude, out-of-plane electromechanical responses of other TMD materials exist and vary from one other. The comparison of the relative response of each TMD material may give insights into the origin of the signal. By comparing known and calculated parameters of TMDs[16,41,128], including lattice constants, Young's modulus, and dielectric susceptibility, trends that may be expected for a piezoelectric or flexoelectric[10,126] response can be investigated.

This chapter will first overview the fabrication processes used to create the remaining TMD samples of $MoSe_2$, WS_2, and WSe_2 on gold-coated silicon substrates. The PFM measurement results are then given with a brief description, but referring to Chapter 3 & 4 is recommended for a deeper discussion of the measurement process. An analysis of the relative magnitudes of the measured d_{33}^{eff} values between the TMDs is given along with what may be expected if flexoelectricity is present.

5.2. EXPERIMENTAL METHODS

5.2.1. $MoSe_2$ Sample Fabrication and Characterization

The $MoSe_2$ sample was created from a bulk $MoSe_2$ crystal. The fabrication process uses blue polyethylene cleanroom tape to exfoliate the bulk crystal and then is used to transfers the $MoSe_2$ onto PDMS. The $MoSe_2$ on PDMS is then placed on a gold-coated

silicon substrate and heated to 70 ˚C on a hot plate for 5 minutes. Slowly peeling the PDMS away transfers the $MoSe_2$ onto the gold. It is found that TMDs transfer more successfully onto the gold substrate using the intermediate PDMS stamp instead of going directly to the gold-coated substrate.

A representative area of one sample is shown in Figure 5.1. An optical microscope image is shown in Figure 5.1 (a), where the monolayer $MoSe_2$ region is on the order of 0.8 μm x 1.5 μm in size. Next to it in Figure 5.1 (b) is a tapping mode AFM image showing the monolayer region. The region is confirmed to be monolayer using Raman spectroscopy, shown in Figure 5.1 (c). The large peak around 245 cm^{-1}, the *A'* peak (A_{1g} in multilayer), is redshifted from the thicker areas, and more importantly, there is no peak around 350 cm^{-1}. This is the B_{2g} mode and is only present in few layer $MoSe_2$, from its absence, the area is concluded to be monolayer[129].

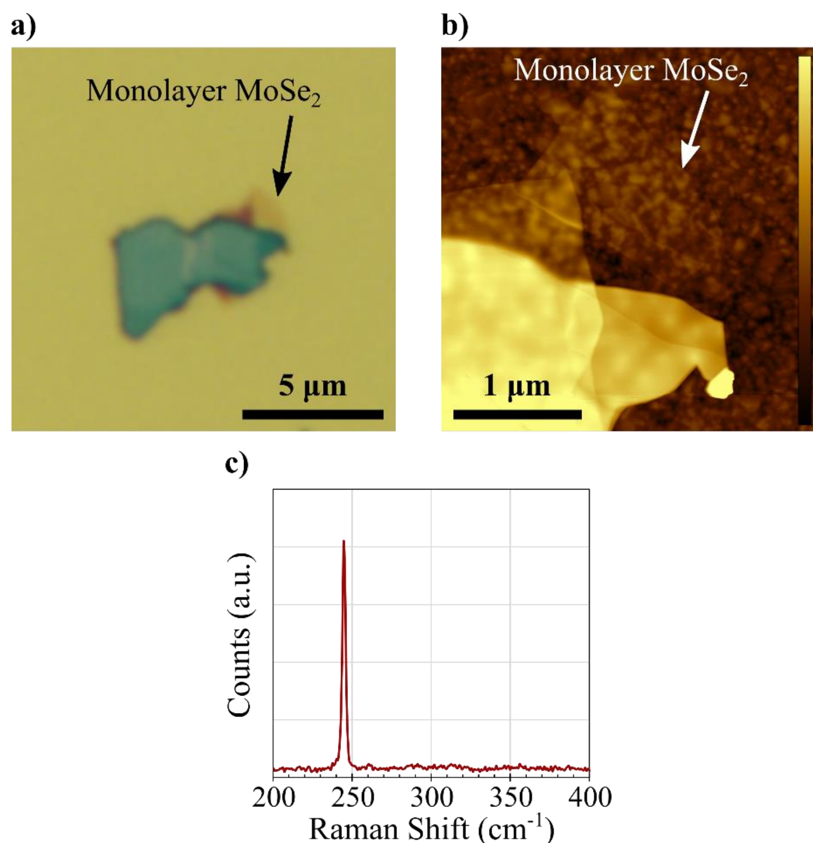

Figure 5.1 The $MoSe_2$ sample fabricated on gold is shown. An optical microscope image is shown in (a), and a tapping mode AFM image is shown in (b) where the color bar indicates heights of 0 nm to 30 nm. This tapping mode image was edited using the Gwyddion open source SPM data analysis software. The Raman spectrum of the monolayer region is shown in (c).

5.2.2. WS_2 Sample Fabrication and Characterization

The WS_2 samples were fabricated the same way as the $MoSe_2$ samples. Blue cleanroom tape was used to exfoliate a bulk WS_2 crystal first onto PDMS and is then transferred onto a gold-coated silicon substrate. The fabricated sample is shown in Figure 5.2 (a) in an optical microscope image. The black and red dots on the image indicate the location of the Raman (b) and photoluminescence (c) measurements for monolayer and multilayer, respectively. The Raman signal on monolayer is weaker in relative magnitude compared to the multilayer area[130]. The photoluminescence measurements allow for a

clearer distinction between monolayer and multilayer locations. Monolayer WS_2 is a direct bandgap semiconductor, while multilayer is an indirect semiconductor, meaning that monolayer will more strongly luminesce compared to multilayer. This is seen in the PL measurement in Figure 5.2 (c) where the displayed multilayer signal has been multiplied by a factor of two. A second peak also appears in multilayer originating from the indirect gap which is not present in monolayer, providing another distinguishing feature of monolayer WS_2[131].

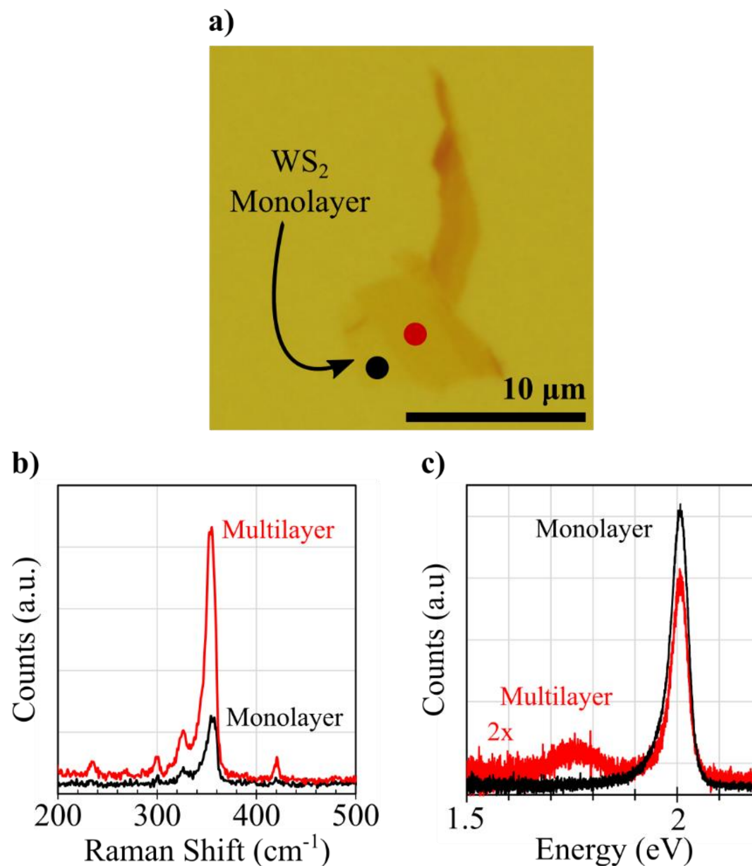

Figure 5.2 The WS_2 sample fabricated on gold. An optical microscope image is given in (a). The black and red dot indicate the location of the monolayer and multilayer measurements for the Raman (b) and photoluminescence (c) measurements.

5.2.3. WSe_2 Sample Fabrication and Characterization

Like the $MoSe_2$ and WS_2 samples, the WSe_2 sample was fabricated via exfoliation from a bulk crystal using blue cleanroom tape and a PDMS stamp. The receiving substrate is again gold-coated silicon. Figure 5.3 (a) shows an optical microscope image of the sample with the black and red dots indicating the locations of the Raman measurement for monolayer and multilayer locations, respectively. Monolayer WSe_2 has a very distinctive Raman characteristic where a peak around ~ 310 cm^{-1} vanishes in monolayer[129,130]. The origin of the peak is most-likely from an interlayer shear mode.

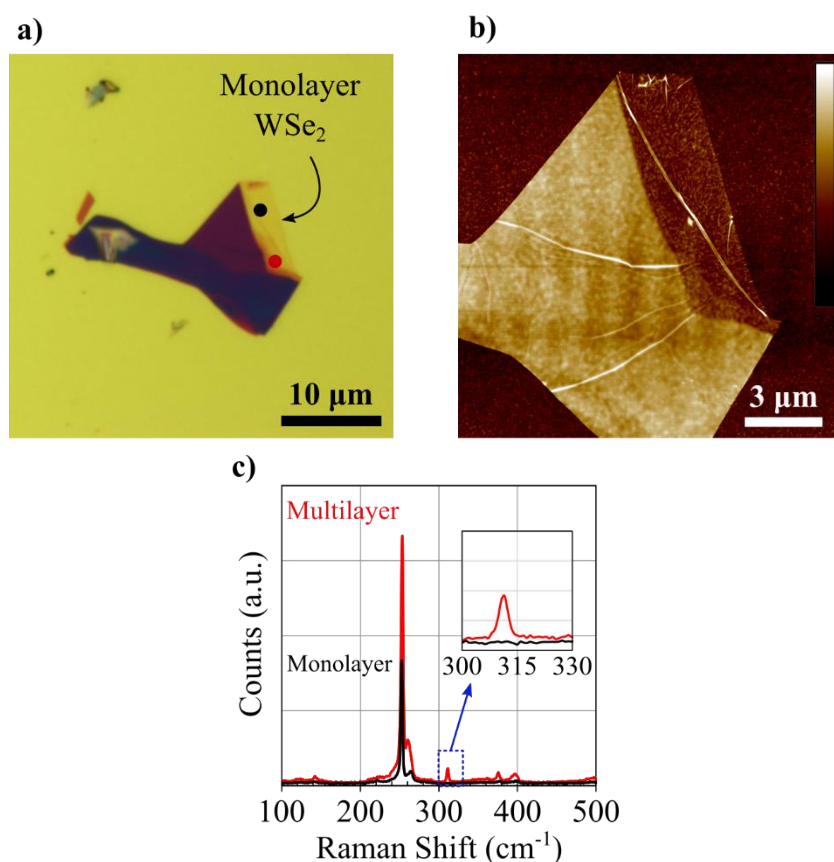

Figure 5.3 The WSe_2 sample fabricated on gold. An optical microscope image is given in (a) and a tapping mode AFM is given in (b). The color bar represents height of 0 nm to 26.6 nm. A Raman measurement is shown in (c) of the monolayer and multilayer region of the WSe_2 sample on the black and red dot in (a).

5.3. RESULTS

5.3.1. $MoSe_2$ PFM

The same $MoSe_2$ flake shown in Figure 5.1 is measured with PFM and the results are presented in Figure 5.4. The same procedure is followed as described for MoS_2 in Chapter 4. When the drive voltage is applied there is contrast arising between the $MoSe_2$ flake and the gold substrate. When a fresh AFM tip is used, the contrast is very distinct. Without applying the drive voltage, the contrast vanishes, indicating that there are no scanning artifacts. It is interesting to note that the PFM amplitude also reveals differences when a different number of layers is present. One issue which arises, is that the voltage-off condition magnitudes are not as consistent with the measurements taken on the gold substrates as MoS_2 samples. The origin of this discrepancy is not fully understood at this time, but possibly comes from sample contaminants. The measurement is considered more accurate when the background subtraction is performed using the gold substrate measurement since the values are taken from within the same PFM measurement. The background subtraction method to calculate d_{33}^{eff} of this measurement while using the gold as the background signal is 1.87 pm V^{-1}. Multiple measurements of only the monolayer region are taken on this area, the results of which are summarized in Table 5.1.

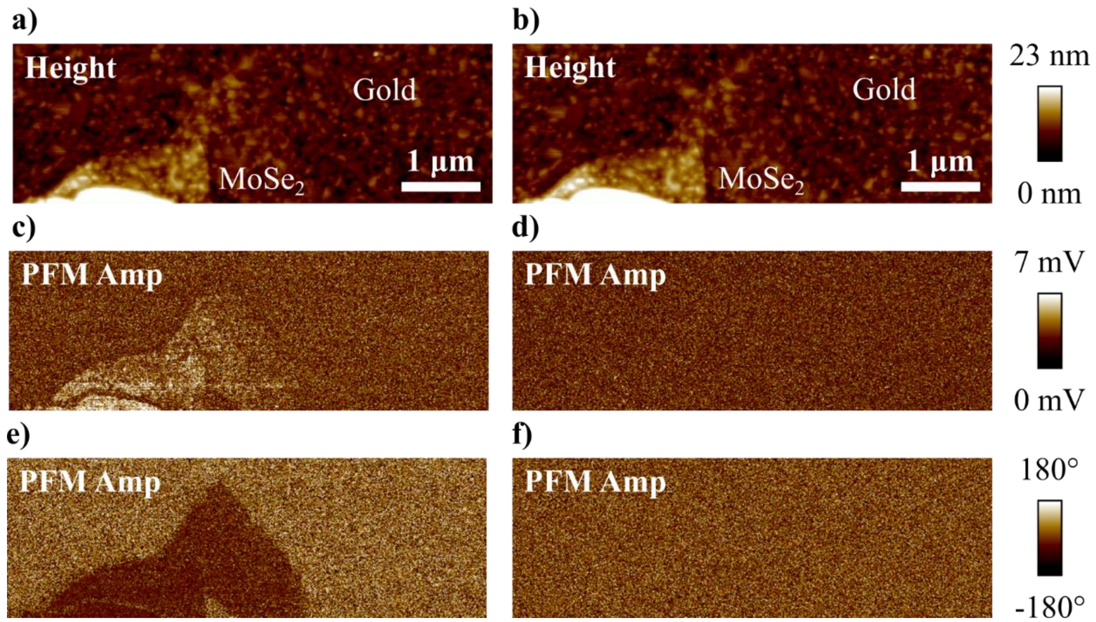

Figure 5.4 PFM images of $MoSe_2$ with the drive voltage applied (a, c, e) and not applied (b, d, f). The height image is given in (a, b), the PFM amplitude image is given in (c, d) and the PFM phase is given in (e, f). The scale bars correspond to both images to their left. The imaging conditions were: V_d = 5 V, f_d = 60 kHz, scan speed = 5 µm/sec.

5.3.2. WS_2 PFM

The PFM measurement from the same area as in Figure 5.2 are presented in Figure 5.5. The same measurement process is used as described in Chapter 4. As with the MoS_2 and $MoSe_2$, there is clear contrast between the WS_2 monolayer area and the gold substrate when the drive voltage is applied but not when the drive voltage is not applied. This indicates that there is out-of-plane electromechanical response being measured in the WSe_2 flake. The voltage-off condition is also fairly similar to the measurement of the gold substrate with the drive voltage applied. Also, there are some distinctions between monolayer and multilayer areas as can be seen with the slight color contrast on the right side of the PFM images in Figure 5.5 (c) and (e). The measured d_{33}^{eff} calculated for this PFM image by using the measurement of the gold as the background condition is 0.89 pm

V^{-1}. The results obtained from multiple measurements taken in this monolayer area are summarized in Table 5.1.

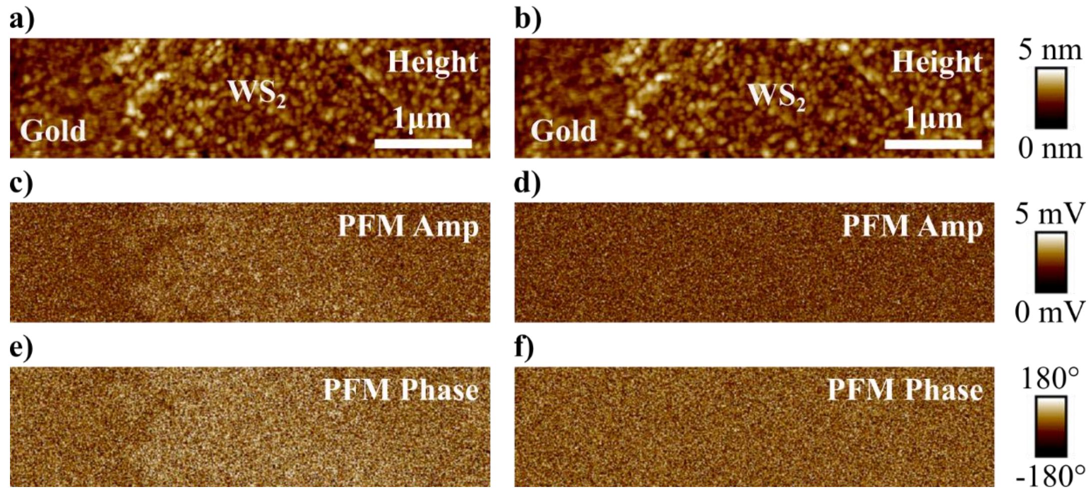

Figure 5.5 PFM images of WS_2 with the drive voltage applied (a, c, e) and not applied (b, d, f). The height image is given in (a, b), the PFM amplitude image is given in (c, d) and the PFM phase is given in (e, f). The scale bars correspond to both images to their left. The imaging conditions were: $V_d = 7$ V, $f_d = 60$ kHz, scan speed = 5 μm/sec.

5.3.3. WSe_2 PFM

PFM measurements from the same area as in Figure 5.3 are presented in Figure 5.6. The same measurement process is used as described in Chapter 4. As with the other TMDs, there is clear contrast between the WSe_2 flake and the gold substrate. This, again, indicates that there is out-of-plane electromechanical response within WSe_2. The vanishing contrast in the voltage-off condition indicates that there are no scanning artifacts. The d_{33}^{eff} calculation for this measurement using the gold as the background measurement is 0.54 pm V^{-1}.

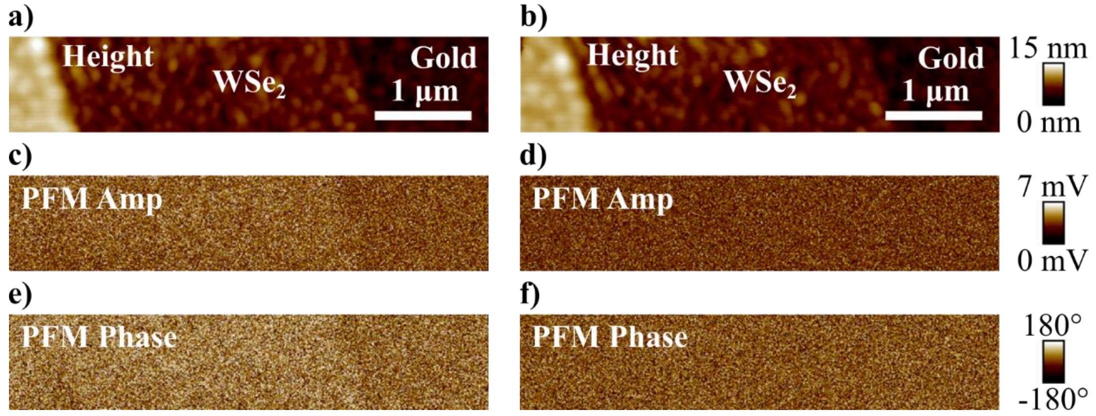

Figure 5.6 PFM images of WSe_2 with the drive voltage applied (a, c, e) and not applied (b, d, f). The height image is given in (a, b), the PFM amplitude image is given in (c, d) and the PFM phase is given in (e, f). The scale bars correspond to both images to their left. The imaging conditions were V_d = 7 V, f_d = 60 kHz, scan speed = 5 µm/sec.

5.4. Discussion

A summary of all the d_{33}^{eff} measurements across the four TMDs studied here is given in Table 5.1. The uncertainty values are the standard deviations originating from averaging over multiple measurements for a single TMD. Also given in Table 5.1 are different parameters associated with the TMDs that are considered when estimating an expected trend based on a simple model for flexoelectricity. The basic parameters included are lattice constant[16], a_0, dielectric susceptibility[132], χ, and the 2D Young's modulus calculated from DFT estimates of the elastic stiffness of the TMDs[16,128], Y_{2D}. Calculated values of the in-plane piezoelectric coefficient[16] d_{11} are also shown for a comparison. Measured values of the in-plane piezoelectric coefficient have varied slightly from this theoretical measurement[45].

TMD	a_0 [16] (Å)	χ [16]	Y_{2D} [132] (N/m)	d_{11} [16] (pm/V)	μ_{est} (nC/m)	d_{33}^{eff} (pm/V)	μ_{eff}^{*} (nC/m)
MoS_2	3.19	3.26	137.9	3.73	0.130	0.98 ± 0.11	0.067
$MoSe_2$	3.32	3.74	113.8	4.72	0.144	1.42 ± 0.36	0.081
WS_2	3.19	3.13	150.7	2.19	0.125	0.66 ± 0.18	0.050
WSe_2	3.32	3.63	123.1	2.79	0.139	0.42 ± 0.11	0.026

Table 5.1 A summary of the TMD materials investigated with PFM in this work. Also included from literature are the lattice constant[16], a_0, dielectric susceptibility[132], χ, the 2D Young's modulus[16,128], Y_{2D}, previous DFT estimates of in-plane piezoelectricity[16], d_{11}, and the estimated flexoelectric coefficient, μ_{est}. Here d_{33}^{eff} is calculated using gold measurement as the background vector. The effective flexoelectric coefficient μ_{eff}^{*} is also estimated for each TMD from the PFM measurements.

Now consider again Kogan's order-of-magnitude estimate of flexoelectricity[126],

$$\mu_{est} \approx \frac{q\chi}{4\pi\epsilon_0 a_0}. \tag{5.1}$$

This simple relation gives some insight into which parameters may be affecting the magnitude of the flexoelectric response. The parameters in Equation (5.1) that are material dependent are χ and a_0. Table 5.1 also gives the calculated μ_{est} using the values obtained from established references[16,132]. Additionally, the calculated value of μ_{eff}^{*} based on the PFM measurements is given in the table and was calculated as

$$\mu_{eff}^{*} \approx \frac{d_{33}^{eff} \cdot Y_{2D}}{2}. \tag{5.2}$$

This equation is adapted from Equation (4.16), where Y_{2D} is used in place of the Young's modulus and film thickness. The purpose of this change is because of the absence or sparsity of measured Young's modulus values for the other TMDs. Instead of using measured values, Y_{2D} is used because it is readily calculated from the elastic stiffness

coefficients of monolayer TMDs calculated from density function theory (DFT). The relation used is[128]

$$Y_{2D} = \frac{C_{11}^2 - C_{12}^2}{C_{11}}, \tag{5.3}$$

where C is the elastic stiffness of monolayer TMDs. The stiffness values used for all TMDs are all taken from the same report[16] (relaxed-ion values are used), ensuring more direct comparability when assessing the measured results of the TMDs.

Both the estimate of μ_{est} and μ_{eff}^* may not be the most accurate in an absolute sense, but when compared across the TMDs, they offer some insights. A visual comparison of the two values is given in Figure 5.7. First, it can be seen that μ_{est} correctly predicts $MoSe_2$ to have the largest measured out-of-plane electromechanical response μ_{eff}^*. It also shows a fairly accurate trend predicting the relative magnitude of the other TMDs, except for WSe_2. This discrepancy could be arising from one of two sources, either the measurement of the out-of-plane electromechanical response is being affected by an unidentified condition, or there are missing pieces to the basic model put forward to describe the flexoelectric response. In one experiment, a PFM measurement was taken of WSe_2 followed directly by a measurement of $MoSe_2$ using the same AFM tip with the same measurement conditions. The results from this experiment agree with the results shown in Table 5.1, supporting the validity of the measured results, and suggest something about WSe_2 is causing the discrepancy. Further study into the origin of the discrepancy could yield a better model of flexoelectricity.

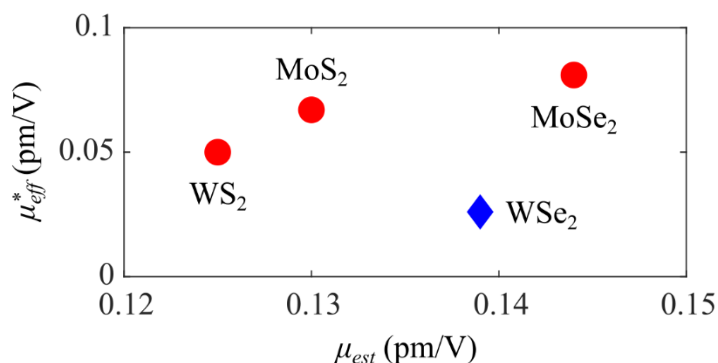

Figure 5.7 A plot comparing the estimated value of the flexoelectric coefficient, μ_{est}, using Kogan's method to the calculated value of the flexoelectric coefficient, μ^*_{eff} , from PFM measurements. WSe_2 is shown as a blue diamond to emphasis that it does not follow the trend of the other TMDs.

5.5. Conclusions and Significance

By exploring the out-of-plane electromechanical response of different TMDs, additional evidence is provided that the response being measured is a flexoelectric response. In this chapter, $MoSe_2$, WS_2, and WSe_2 were measured with PFM and compared against the previous measurements taken on MoS_2. The relative magnitudes of three out of the four TMDs measured matched the predicted trend using a simple model. These results can be used to gain further knowledge about the basic nature of electromechanical effects and specifically flexoelectricity. By developing a more detailed model that more closely follows the results obtained will give a better understanding of flexoelectricity. Alternately, it should be confirmed that the PFM results are fully accurate and are not being affected by unseen variables. There is always the possibility that the obtained results were anomalous so additional studies to further confirm the results will strengthen the physical models.

Chapter 6:

Conclusions and Outlook

The overall conclusions and significance of the research reported in this dissertation is described in this chapter. Also presented are suggestions for future research that might yield interesting results.

6.1. Summary and Conclusion of Research

In this work, progress has been made towards understanding the electromechanical response of 2D TMD materials. Previous work had revealed the nature of intrinsic piezoelectricity in certain 2D materials that arises within the plane of the crystal's atoms. The main contribution from this work is that all measured TMD materials also exhibit an out-of-plane electromechanical response which should not be allowed from piezoelectricity alone. The most-likely source of this effect is flexoelectricity. This knowledge can allow for a deeper understanding of the flexoelectric effect as well as enable new capabilities for electromechanical devices.

In Chapter two, a property relevant to 2D device fabrication and 2D device reliability is investigated. The strength of adhesion between 2D materials and soft substrates is important to understand for fabrication because 2D materials often need to be transferred from one substrate to another. An example of this is transferring CVD grown MoS_2 from a growth substrate to a receiving substrate on which a device will be created. The transfer will often be done using a soft material as a stamp, such as PDMS, which will need to adhere more strongly to the 2D material than the growth substrate, but not as strongly as the receiving substrate. By performing buckle analysis, the strength of adhesion was readily obtained to be about 18 mJ m^{-2} for MoS_2 to PDMS. The strength of adhesion is also important for 2D material devices undergoing straining from bending and stretching if used in wearable devices. A strong adhesion value is desired in these cases to prevent slippage and/or mechanical failure which could create undesired buckles or hinder the device's electrical performance.

In Chapter 3, a deeper understanding of the measurement technique PFM is developed in order to perform out-of-plane electromechanical coupling experiments on 2D materials. PFM was originally developed to characterize ferroelectric materials which

have a permanent electrical polarization. To provide more robust quantitative analysis of 2D materials via PFM, a slightly different procedure was needed to perform background-subtraction of the inherent noise within the system. By performing a PFM measurement in which both a TMD area and the underlaying gold are is exposed, a vector background subtraction can be performed by using the PFM amplitude and PFM phase channels. This procedure allows for a more accurate quantitative representation of the measured signal.

The PFM technique is then used in Chapter 4 to detect and measure the out-of-plane electromechanical coupling of MoS_2 for the first time. By observing contrast in the PFM amplitude and phase channels, a background vector subtraction can be performed to estimate the magnitude of the response. Formulating the measured signal as a traditional piezoelectric response, d_{33}^{eff}, a value of roughly 1 pm V^{-1} is obtained, which is comparable to other calculations and measurements of in-plane piezoelectricity in MoS_2[45]. However, piezoelectricity in the out-of-plane direction should not be allowed due to the symmetry of the crystal, so the source of the signal could be originating from the flexoelectric effect. With this new interpretation, the measured signal is estimated to correspond to a flexoelectric response, μ_{eff}^{*}, equal to about 0.1 nC m^{-1}. This corresponds well with the values obtained from an estimation method for the flexoelectric coefficient proposed by Kogan[126].

To further investigate the out-of-plane electromechanical response of TMDs, $MoSe_2$, WS_2, and WSe_2 are measured and analyzed in Chapter 5. It was found that all of the measured TMDs exhibit this out-of-plane electromechanical coupling behavior. Furthermore, the relative magnitudes of their responses are compared to each other and what might be expected by using Kogan's estimation method. The results show that Kogan's method correctly identifies the TMD that exhibits the strongest response, $MoSe_2$, as well as the order of the response magnitude for 3 of the 4 TMDs measured. This gives

more evidence that the measured response could be from flexoelectricity. Additionally, the unexpected result from WSe_2 could means more sophisticated models are required to describe the electromechanical response of TMDs than only using Kogan's method.

The results of this research, that TMDs exhibit an out-of-plane electromechanical response, have many applications and significance across multiple fields. First, this reveals that 2D materials offer a platform to further study the flexoelectric effect to allow for better convergence between theory and experiment. Additionally, knowing that out-of-plane polarization can occur could be used to enhance piezoelectric properties or create new types of devices for sensing, actuating, or harvesting energy. Also, within the field of flexible electronics, the knowledge that polarization can be induced from mechanical deformation is extremely important to understand so higher fidelity models can be created of how a device's electronic properties vary under all possible conditions.

The original motivation of this research was to gain understanding of flexoelectricity, to learn more about 2D materials, and the possibility of using flexoelectricity in 2D materials for energy harvesters. The research presented here touches on all three of these goals. It was learned that 2D materials exhibit the previously unknown out-of-plane electromechanical coupling, and that the source of this may be from flexoelectricity. Also, by comparing the magnitude of the out-of-plane response between the TMDs, a better understanding of the flexoelectric effect can be developed. Finally, the knowledge gained in this work could be used to design thin, flexible, energy harvesters with 2D materials for potential use in epidermal electronics.

6.2. Future work and Outlook

There is both experimental and theoretical work that can be done next. On the experimental side, more measurements could be done to further confirm that WSe_2 does in

fact not follow the trend predicted by Kogan's estimation method. There is a chance that a limited number of measurements may not have been enough to correctly characterize the material. Creating another sample and performing measurements would be useful to confirm the magnitude of the previous measurement.

A second experiment that could reveal interesting properties is performing the out-of-plane PFM measurement on a stacked heterostructure of TMDs. In this case, out-of-plane piezoelectricity would be possible because the symmetry of the system would be further broken. This means there could be an even stronger response measured using PFM. Using any two TMD materials should be able to accomplish this, but the relative stacking alignment should be taken into consideration.

The measurement results provided here can also guide theoretical studies. By creating a physical model of flexoelectricity which matches the experimentally observed results, a more accurate understanding of electromechanical coupling can be obtained.

References

1. Kim, D.-H. *et al.* Epidermal Electronics. *Science* **333,** 838–43 (2011).
2. Kim, D.-H., Ghaffari, R., Lu, N. & Rogers, J. A. Flexible and stretchable electronics for biointegrated devices. *Annu. Rev. Biomed. Eng.* **14,** 113–128 (2012).
3. Lu, N. & Kim, D.-H. Flexible and Stretchable Electronics Paving the Way for Soft Robotics. *Soft Robot.* **1,** 53–62 (2014).
4. Kim, D.-H., Lu, N., Ghaffari, R. & Rogers, J. A. Inorganic semiconductor nanomaterials for flexible and stretchable bio-integrated electronics. *NPG Asia Mater.* **4,** e15–e15 (2012).
5. Yang, S. *et al.* 'Cut-and-Paste' Manufacture of Multiparametric Epidermal Sensor Systems. *Adv. Mater.* **27,** 6423–6430 (2015).
6. Jeong, J.-W. *et al.* Materials and optimized designs for human-machine interfaces via epidermal electronics. *Adv. Mater.* **25,** 6839–46 (2013).
7. Kabiri Ameri, S. *et al.* Graphene Electronic Tattoo Sensors. *ACS Nano* **11,** 7634–7641 (2017).
8. Widlund, T., Yang, S., Hsu, Y. Y. & Lu, N. Stretchability and compliance of freestanding serpentine-shaped ribbons. *Int. J. Solids Struct.* **51,** 4026–4037 (2014).
9. Martin, R. M. Piezoelectricity. *Phys. Rev. B* **5,** 1607–1613 (1972).
10. Yudin, P. V & Tagantsev, a K. Fundamentals of flexoelectricity in solids. *Nanotechnology* **24,** 432001 (2013).
11. Zubko, P., Catalan, G. & Tagantsev, A. K. Flexoelectric Effect in Solids. *Annu. Rev. Mater. Res.* **43,** 387–421 (2013).
12. Nguyen, T. D., Mao, S., Yeh, Y.-W., Purohit, P. K. & McAlpine, M. C. Nanoscale Flexoelectricity. *Adv. Mater.* **25,** 946–974 (2013).
13. Lee, C., Wei, X., Kysar, J. W. & Hone, J. Measurement of the elastic properties and intrinsic strength of monolayer graphene. *Science* **321,** 385–8 (2008).
14. Castellanos-Gomez, A. *et al.* Elastic Properties of Freely Suspended MoS2 Nanosheets. *Adv. Mater.* **24,** 772–5 (2012).
15. Bertolazzi, S., Brivio, J. & Kis, A. Stretching and breaking of ultrathin MoS2. *ACS Nano* **5,** 9703–9 (2011).
16. Duerloo, K. A. N., Ong, M. T. & Reed, E. J. Intrinsic piezoelectricity in two-dimensional materials. *J. Phys. Chem. Lett.* **3,** 2871–2876 (2012).
17. Novoselov, K. S. *et al.* Electric field effect in atomically thin carbon films. *Science*

306, 666–9 (2004).

18. Geim, A. K., Novoselov, K. S. & Article, P. The rise of graphene. *Nat. Mater.* **6,** 183–191 (2007).
19. Radisavljevic, B., Radenovic, A., Brivio, J., Giacometti, V. & Kis, A. Single-Layer MoS2 Transistors. *Nat. Nanotechnol.* **6,** 147–50 (2011).
20. Nair, R. R. *et al.* Fine Structure Constant Defines Visual Transparency of Graphene. *Science (80-.).* **320,** 1308–1308 (2008).
21. Pospischil, A., Furchi, M. M. & Mueller, T. Solar-energy conversion and light emission in an atomic monolayer p-n diode. *Nat. Nanotechnol.* **9,** 257–61 (2014).
22. Branny, A., Kumar, S., Proux, R. & Gerardot, B. D. Deterministic strain-induced arrays of quantum emitters in a two-dimensional semiconductor. *Nat. Commun.* **8,** 15053 (2017).
23. Palacios-Berraquero, C. *et al.* Large-scale quantum-emitter arrays in atomically thin semiconductors. *Nat. Commun.* **8,** 15093 (2017).
24. Desai, S. B. *et al.* MoS2 transistors with 1-nanometer gate lengths. *Science (80-.).* **354,** 99–102 (2016).
25. Hill, E. W., Vijayaragahvan, A. & Novoselov, K. Graphene Sensors. *IEEE Sens. J.* **11,** 3161–3170 (2011).
26. Zhao, J., Zhang, G.-Y. & Shi, D.-X. Review of graphene-based strain sensors. *Chinese Phys. B* **22,** 57701 (2013).
27. Petrone, N., Hone, J., Akinwande, D., Petrone, N. & Hone, J. Two-dimensional flexible nanoelectronics. *Nat. Commun.* **5,** 1–12 (2015).
28. Cady, W. G. *Piezoelectricity*. (McGraw-Hill Book Company, Inc., 1946).
29. Ganatra, R. & Zhang, Q. Few-Layer MoS2: A Promising Layered Semiconductor. *ACS Nano* **8,** 4074–99 (2014).
30. Novoselov, K. S. Nobel Lecture: Graphene: Materials in the Flatland. *Rev. Mod. Phys.* **83,** 837–849 (2011).
31. Landis, C. M., Yakobson, B. I., Dumitrică, T., Landis, C. M. & Yakobson, B. I. Curvature-induced polarization in carbon nanoshells. *Chem. Phys. Lett.* **360,** 182–188 (2002).
32. Li, X., Wang, X., Zhang, L., Lee, S. & Dai, H. Chemically derived, ultrasmooth graphene nanoribbon semiconductors. *Science* **319,** 1229–32 (2008).
33. Chandratre, S. & Sharma, P. Coaxing graphene to be piezoelectric. *Appl. Phys. Lett.* **100,** 2014–2017 (2012).
34. Novoselov, K. Graphene: Mind the gap. *Nat. Mater.* **6,** 720–721 (2007).

35. Novoselov, K. S., Mishchenko, A., Carvalho, A. & Castro Neto, A. H. 2D materials and van der Waals heterostructures. *Science (80-.).* **353,** aac9439 (2016).

36. Manzeli, S., Ovchinnikov, D., Pasquier, D., Yazyev, O. V. & Kis, A. 2D transition metal dichalcogenides. *Nat. Rev. Mater.* **2,** 17033 (2017).

37. Bursian, E. V. & Trunov, N. N. Nonlocal piezoelectric effect. *Sov. Phys. Solid State* **16,** 760–762 (1974).

38. Ahmadpoor, F. & Sharma, P. Flexoelectricity in two-dimensional crystalline and biological membranes. *Nanoscale* **7,** 16555–16570 (2015).

39. Krichen, S. & Sharma, P. Flexoelectricity: A Perspective on an Unusual Electromechanical Coupling. *J. Appl. Mech.* **83,** 30801 (2016).

40. Ong, M. T. & Reed, E. J. Engineered Piezoelectricity in Graphene. *ACS Nano* **6,** 1387–1394 (2011).

41. Blonsky, M. N., Zhuang, H. L., Singh, A. K. & Hennig, R. G. Ab Initio Prediction of Piezoelectricity in Two-Dimensional Materials. *ACS Nano* **9,** 9885–9891 (2015).

42. Fei, R., Li, W., Li, J. & Yang, L. Giant piezoelectricity of monolayer group IV monochalcogenides: SnSe, SnS, GeSe, and GeS. *Appl. Phys. Lett.* **107,** 173104 (2015).

43. Dong, L., Lou, J. & Shenoy, V. B. Large In-Plane and Vertical Piezoelectricity in Janus Transition Metal Dichalchogenides. *ACS Nano* **11,** 8242–8248 (2017).

44. Wu, W. *et al.* Piezoelectricity of single-atomic-layer MoS2 for energy conversion and piezotronics. *Nature* **514,** 470–474 (2014).

45. Zhu, H. *et al.* Observation of piezoelectricity in free-standing monolayer MoS2. *Nat. Nanotechnol.* **10,** 151–155 (2014).

46. Qi, J. *et al.* Piezoelectric effect in chemical vapour deposition-grown atomic-monolayer triangular molybdenum disulfide piezotronics. *Nat. Commun.* **6,** 7430 (2015).

47. Kim, S. K. *et al.* Directional dependent piezoelectric effect in CVD grown monolayer MoS 2 for flexible piezoelectric nanogenerators. *Nano Energy* **22,** 483–489 (2016).

48. Lu, A.-Y. *et al.* Janus monolayers of transition metal dichalcogenides. *Nat. Nanotechnol.* **12,** 1–29 (2017).

49. Kalinin, S. V. & Meunier, V. Electronic flexoelectricity in low-dimensional systems. *Phys. Rev. B - Condens. Matter Mater. Phys.* **77,** 1–4 (2008).

50. Kvashnin, A. G., Sorokin, P. B. & Yakobson, B. I. Flexoelectricity in Carbon Nanostructures: Nanotubes, Fullerenes, and Nanocones. *J. Phys. Chem. Lett.* **6,** 2740–2744 (2015).

51. Kundalwal, S. I. I., Meguid, S. A. A. & Weng, G. J. J. Strain gradient polarization in graphene. *Carbon N. Y.* **117,** 462–472 (2017).

52. Naumov, I., Bratkovsky, A. M. & Ranjan, V. Unusual Flexoelectric Effect in Two-Dimensional Noncentrosymmetric sp2-Bonded Crystals. *Phys. Rev. Lett.* **102,** 217601 (2009).

53. Duerloo, K.-A. N. & Reed, E. J. Flexural electromechanical coupling: a nanoscale emergent property of boron nitride bilayers. *Nano Lett.* **13,** 1681–6 (2013).

54. Michel, K. H., Neek-Amal, M. & Peeters, F. M. Static flexural modes and piezoelectricity in 2D and layered crystals. *Phys. status solidi* **253,** 2311–2315 (2016).

55. Zelisko, M. *et al.* Anomalous piezoelectricity in two-dimensional graphene nitride nanosheets. *Nat. Commun.* **5,** 4284 (2014).

56. Nguyen, A. E. *et al.* Towards Ferroelectric Control of Monolayer MoS2. *Nano Lett.* **15,** 150424143559000 (2015).

57. Jin, H.-J., Yoon, W. Y. & Jo, W. Virtual Out-of-Plane Piezoelectric Response in MoS $_2$ Layers Controlled by Ferroelectric Polarization. *ACS Appl. Mater. Interfaces* **10,** 1334–1339 (2018).

58. Pittenger, B., Erina, N. & Su, C. Quantitative Mechanical Property Mapping at the Nanoscale with PeakForce QNM. *Burker Appl. Note* **128,** 1–12 (2009).

59. Rosenthal, P. a., Yu, E. T., Pierson, R. L., Zampardi, P. J. & Introduction, I. Characterization of AlGaAs/GaAs heterojunction bipolar transistor structures using cross-sectional scanning force microscopy. *J. Appl. Phys.* **87,** 1937 (2000).

60. Yaminsky, I. V & Tishin, A. M. Magnetic force microscopy. *Russ. Chem. Rev.* **68,** 165–170 (1999).

61. Morozovska, A. N., Eliseev, E. A., Balke, N. & Kalinin, S. V. Local probing of ionic diffusion by electrochemical strain microscopy: Spatial resolution and signal formation mechanisms. *J. Appl. Phys.* **108,** (2010).

62. Nemes-Incze, P., Osváth, Z., Kamarás, K. & Biró, L. P. Anomalies in thickness measurements of graphene and few layer graphite crystals by tapping mode atomic force microscopy. *Carbon N. Y.* **46,** 1435–1442 (2008).

63. Kim, K. S. K. S. K. S. *et al.* Large-scale pattern growth of graphene films for stretchable transparent electrodes. *Nature* **457,** 706–710 (2009).

64. Wang, F. *et al.* Gate-variable optical transitions in graphene. *Science* **320,** 206–209 (2008).

65. Zhang, Y., Tan, Y.-W., Stormer, H. L. & Kim, P. Experimental observation of the quantum Hall effect and Berry's phase in graphene. *Nature* **438,** 201–204 (2005).

66. Rogers, J. A., Someya, T. & Huang, Y. Materials and mechanics for stretchable

electronics. *Science* **327,** 1603–1607 (2010).

67. Suo, Z. Mechanics of stretchable electronics and soft machines. *MRS Bull.* **37,** 218–225 (2012).

68. Bae, S. *et al.* Roll-to-roll production of 30-inch graphene films for transparent electrodes. *Nat. Nanotechnol.* **5,** 574–8 (2010).

69. Suk, J. W. *et al.* Transfer of CVD-Grown Monolayer Graphene onto Arbitrary Substrates. *ACS Nano* **5,** 6916–6924 (2011).

70. Conley, H. J. *et al.* Bandgap Engineering of Strained Monolayer and Bilayer MoS2. *Nano Lett.* **13,** 3626–30 (2013).

71. Chang, H.-Y. *et al.* High-Performance, Highly Bendable MoS2 Transistors with High-K Dielectrics for Flexible Low-Power Systems. *ACS Nano* **7,** 5446–52 (2013).

72. Bunch, J. S. & Dunn, M. L. Adhesion mechanics of graphene membranes. *Solid State Commun.* **152,** 1359–1364 (2012).

73. Koenig, S. P., Boddeti, N. G., Dunn, M. L. & Bunch, J. S. Ultrastrong adhesion of graphene membranes. *Nat. Nanotechnol.* **6,** 543–6 (2011).

74. Yoon, T. *et al.* Direct measurement of adhesion energy of monolayer graphene as-grown on copper and its application to renewable transfer process. *Nano Lett.* **12,** 1448–52 (2012).

75. Cao, Z. *et al.* A blister test for interfacial adhesion of large-scale transferred graphene. *Carbon N. Y.* **69,** 390–400 (2014).

76. Scharfenberg, S. *et al.* Probing the mechanical properties of graphene using a corrugated elastic substrate. *Appl. Phys. Lett.* **98,** 91908 (2011).

77. Jiang, T., Huang, R. & Zhu, Y. Interfacial sliding and buckling of monolayer graphene on a stretchable substrate. *Adv. Funct. Mater.* **24,** 396–402 (2014).

78. Bowden, N., Brittain, S. & Evans, A. Spontaneous formation of ordered structures in thin films of metals supported on an elastomeric polymer. *Nature* **393,** 146–149 (1998).

79. Lacour, S. P., Wagner, S., Huang, Z. & Suo, Z. Stretchable gold conductors on elastomeric substrates. *Appl. Phys. Lett.* **82,** 2404–2406 (2003).

80. Khang, D.-Y., Jiang, H., Huang, Y. & Rogers, J. A. A stretchable form of single-crystal silicon for high-performance electronics on rubber substrates. *Science (80-.).* **311,** 208–212 (2006).

81. Sun, Y., Choi, W. M., Jiang, H., Huang, Y. Y. & Rogers, J. A. Controlled buckling of semiconductor nanoribbons for stretchable electronics. *Nat. Nanotechnol.* **1,** 201–207 (2006).

82. Zang, J. *et al.* Multifunctionality and control of the crumpling and unfolding of large-area graphene. *Nat. Mater.* **12,** 321–5 (2013).

83. Wang, Y. *et al.* Super-elastic graphene ripples for flexible strain sensors. *ACS Nano* **5,** 3645–50 (2011).

84. Stafford, C. M. *et al.* A buckling-based metrology for measuring the elastic moduli of polymeric thin films. *Nat. Mater.* **3,** 545–550 (2004).

85. Wilder, E. a., Guo, S., Lin-Gibson, S., Fasolka, M. J. & Stafford, C. M. Measuring the modulus of soft polymer networks via a buckling-based metrology. *Macromolecules* **39,** 4138–4143 (2006).

86. Pundt, A., Nikitin, E., Pekarski, P. & Kirchheim, R. Adhesion energy between metal films and polymers obtained by studying buckling induced by hydrogen. *Acta Mater.* **52,** 1579–1587 (2004).

87. Cordill, M. J. J., Bahr, D. F. F., Moody, N. R. R. & Gerberich, W. W. W. Adhesion measurements using telephone cord buckles. *Mater. Sci. Eng. A* **443,** 150–155 (2007).

88. Vella, D., Bico, J., Boudaoud, A., Roman, B. & Reis, P. M. The macroscopic delamination of thin films from elastic substrates. *Proc. Natl. Acad. Sci.* **106,** 10901–10906 (2009).

89. Feng, X. *et al.* Competing Fracture in Kinetically Controlled Transfer Printing. *Langmuir* **23,** 12555–60 (2007).

90. Castellanos-Gomez, A. *et al.* Local Strain Engineering in Atomically Thin MoS2. *Nano Lett.* **13,** 5361–6 (2013).

91. Choi, K. M. & Rogers, J. a. A Photocurable Poly(dimethylsiloxane) Chemistry Designed for Soft Lithographic Molding and Printing in the Nanometer Regime. *J. Am. Chem. Soc.* **125,** 4060–4061 (2003).

92. Jiang, H. *et al.* Finite deformation mechanics in buckled thin films on compliant supports. *Proc. Natl. Acad. Sci. U. S. A.* **104,** 15607–15612 (2007).

93. Mei, H., Landis, C. M. & Huang, R. Concomitant wrinkling and buckle-delamination of elastic thin films on compliant substrates. *Mech. Mater.* **43,** 627–642 (2011).

94. Lee, C. *et al.* Anomalous Lattice Vibrations of Single- and Few-Layer MoS2. *ACS Nano* **4,** 2695–700 (2010).

95. Frindt, R. F. Single Crystals of MoS2 Several Molecular Layers Thick. *J. Appl. Phys.* **37,** 1928 (1966).

96. Novoselov, K. S. *et al.* Two-dimensional atomic crystals. *Proc. Natl. Acad. Sci. U. S. A.* **102,** 10451–3 (2005).

97. Tang, D.-M. *et al.* Nanomechanical cleavage of molybdenum disulphide atomic

layers. *Nat. Commun.* **5,** 3631 (2014).

98. Splendiani, A. *et al.* Emerging photoluminescence in monolayer MoS2. *Nano Lett.* **10,** 1271–5 (2010).

99. Liu, K. *et al.* Elastic properties of chemical-vapor-deposited monolayer MoS2, WS2, and their bilayer heterostructures. *Nano Lett.* **14,** 5097–103 (2014).

100. Bevington, P. R. & Robinson, D. K. *Data Reduction and Error Analysis for the Physical Sciences*. (McGraw-Hill Book Company, Inc., 2003).

101. Soergel, E. Piezoresponse force microscopy (PFM). *J. Phys. D. Appl. Phys.* **44,** 464003 (2011).

102. Bonnell, D. a., Kalinin, S. V., Kholkin, a. L. & Gruverman, a. Piezoresponse Force Microscopy: A Window into Electromechanical Behavior at the Nanoscale. *MRS Bull.* **34,** 648–657 (2009).

103. Güthner, P. & Dransfeld, K. Local poling of ferroelectric polymers by scanning force microscopy. *Appl. Phys. Lett.* **61,** 1137–1139 (1992).

104. Vishniakou, S. *et al.* Improved Performance of Zinc Oxide Thin Film Transistor Pressure Sensors and a Demonstration of a Commercial Chip Compatibility with the New Force Sensing Technology. *Adv. Mater. Technol.* 1700279 (2018). doi:10.1002/admt.201700279

105. da Cunha Rodrigues, G. *et al.* Strong piezoelectricity in single-layer graphene deposited on SiO2 grating substrates. *Nat. Commun.* **6,** 7572 (2015).

106. Jungk, T., Hoffmann, A., Soergel, E., Hoffmann, Á. & Soergel, E. Challenges for the determination of piezoelectric constants with piezoresponse force microscopy. *Appl. Phys. Lett.* **91,** 1–4 (2007).

107. Physics, A., Jungk, T., Hoffmann, Á. & Soergel, E. Influence of the inhomogeneous field at the tip on quantitative piezoresponse force microscopy. *Appl. Phys. A* **86,** 353–355 (2007).

108. Kalinin, S. & Bonnell, D. Imaging mechanism of piezoresponse force microscopy of ferroelectric surfaces. *Phys. Rev. B* **65,** 125408 (2002).

109. Jungk, T., Hoffmann, A., Soergel, E., Hoffmann, Á. & Soergel, E. Quantitative analysis of ferroelectric domain imaging with piezoresponse force microscopy. *Appl. Phys. Lett.* **89,** 163507 (2006).

110. Jungk, T., Hoffmann, Á. & Soergel, E. Consequences of the background in piezoresponse force microscopy on the imaging of ferroelectric domain structures. *J. Microsc.* **227,** 72–78 (2007).

111. Fischetti, M. V. & Laux, S. E. Band structure, deformation potentials, and carrier mobility in strained Si, Ge, and SiGe alloys. *J. Appl. Phys.* **80,** 2234 (1996).

112. Qing-Ming Wang, Xiao-Hong Du, Baomin Xu & Cross, L. E. Electromechanical

coupling and output efficiency of piezoelectric bending actuators. *IEEE Trans. Ultrason. Ferroelectr. Freq. Control* **46,** 638–646 (1999).

113. Xu, S. *et al.* Self-powered nanowire devices. *Nat. Nanotechnol.* **5,** 366–73 (2010).

114. Lee, G.-H. *et al.* Flexible and Transparent MoS2 Field-Effect Transistors on Hexagonal Boron Nitride-Graphene Heterostructures. *ACS Nano* **7,** 7931–7936 (2013).

115. Akinwande, D. *et al.* A review on mechanics and mechanical properties of 2D materials—Graphene and beyond. *Extrem. Mech. Lett.* **13,** 42–77 (2017).

116. Shu, L., Wei, X., Pang, T., Yao, X. & Wang, C. Symmetry of flexoelectric coefficients in crystalline medium. *J. Appl. Phys.* **110,** 104106 (2011).

117. Liu, Y. *et al.* Mesoscale Imperfections in MoS2 Atomic Layers Grown by a Vapor Transport Technique. *Nano Lett.* **14,** 4682–4686 (2014).

118. He, K., Poole, C., Mak, K. F. & Shan, J. Experimental demonstration of continuous electronic structure tuning via strain in atomically thin MoS2. *Nano Lett.* **13,** 2931–6 (2013).

119. Buscema, M., Steele, G. A., van der Zant, H. S. J. & Castellanos-Gomez, A. The effect of the substrate on the Raman and photoluminescence emission of single-layer MoS2. *Nano Res.* **7,** 561–571 (2014).

120. Lloyd, D. *et al.* Band Gap Engineering with Ultralarge Biaxial Strains in Suspended Monolayer MoS2. *Nano Lett.* **16,** 5836–5841 (2016).

121. Shearer, C. J., Slattery, A. D., Stapleton, A. J., Shapter, J. G. & Gibson, C. T. Accurate thickness measurement of graphene. *Nanotechnology* **27,** 0

122. Brennan, C. J., Nguyen, J., Yu, E. T. & Lu, N. Interface Adhesion between 2D Materials and Elastomers Measured by Buckle Delaminations. *Adv. Mater. Interfaces* **2,** 1500176 (2015).

123. Man, M. K. L. *et al.* Protecting the properties of monolayer MoS2 on silicon based substrates with an atomically thin buffer. *Sci. Rep.* **6,** 20890 (2016).

124. Bhattacharjee, S. *et al.* Nitride Dielectric Environments to Suppress Surface Optical Phonon Dominated Scattering in High-Performance Multilayer MoS2 FETs. *Adv. Electron. Mater.* **3,** 1–9 (2017).

125. Santos, E. J. G. & Kaxiras, E. Electrically Driven Tuning of the Dielectric Constant in MoS2 Layers. *ACS Nano* **7,** 10741–10746 (2013).

126. SM. Kogan. Piezoelectric effect during inhomogeneous deformation and acoustic scattering of carriers in crystals. *Sov. Phys. Solid State* **5,** 2069–70 (1964).

127. Shin, B. G. *et al.* Indirect Bandgap Puddles in Monolayer MoS2 by Substrate-Induced Local Strain. *Adv. Mater.* **28,** 9378–9384 (2016).

128. Alyo, M. M., Aierken, Y., Deniz, C., Peeters, F. M. & Sevik, C. Promising Piezoelectric Performance of Single Layer Transition- Metal Dichalcogenides and Dioxides. (2015). doi:10.1021/acs.jpcc.5b06428

129. Tonndorf, P. *et al.* Photoluminescence emission and Raman response of monolayer MoS2, MoSe2, and WSe2. *Opt. Express* **21,** 4908 (2013).

130. Zhao, W. *et al.* Lattice dynamics in mono- and few-layer sheets of WS2 and WSe2. *Nanoscale* **5,** 9677 (2013).

131. Zhao, W. *et al.* Evolution of electronic structure in atomically thin sheets of ws 2 and wse2. *ACS Nano* **7,** 791–797 (2013).

132. Ramasubramaniam, A. Large excitonic effects in monolayers of molybdenum and tungsten dichalcogenides. *Phys. Rev. B* **86,** 115409 (2012).